

UC San Diego

UC San Diego Electronic Theses and Dissertations

Title

Planar micro-optic solar concentration

Permalink

<https://escholarship.org/uc/item/50g776w0>

Author

Karp, Jason Harris

Publication Date

2010

Peer reviewed|Thesis/dissertation

UNIVERSITY OF CALIFORNIA, SAN DIEGO

Planar Micro-Optic Solar Concentration

A dissertation submitted in partial satisfaction of the requirements for the degree

Doctor of Philosophy

in

Electrical Engineering (Photonics)

by

Jason Harris Karp

Committee in charge:

Professor Joseph E. Ford, Chair
Professor Prabhakar Bandaru
Professor Yeshaiah Fainman
Professor George Papen
Professor Michael Sailor

2010

Copyright

Jason Harris Karp, 2010
All rights reserved.

The dissertation of Jason Harris Karp is approved, and it
is acceptable in quality and form for publication on
microfilm and electronically:

Chair

University of California, San Diego

2010

Dedication

This dissertation is dedicated to my family.

Table of Contents

Signature Page	iii
Dedication.....	iv
Table of Contents	v
List of Figures.....	viii
List of Tables	xiii
Acknowledgements	xiv
Vita	xvii
Abstract of the Dissertation	xix
CHAPTER 1	1
Introduction	
1.1. SOLAR PHOTOVOLTAICS	1
1.2. SOLAR CELL TECHNOLOGIES	2
1.3. CONCENTRATOR PHOTOVOLTAICS.....	3
1.3.1. Concentration Ratio	4
1.3.2. Acceptance Angle	5
1.3.3. System Aperture.....	6
1.4. WAVEGUIDE CONCENTRATION	8
1.4.1. Total Internal Reflection	9
1.5. WAVEGUIDE TYPES	10
1.5.1. Tapered Guides	10
1.5.2. Planar Guides	11
1.6. PROJECT GOALS.....	12
1.7. DISSERTATION OUTLINE	14
1.8. REFERENCES.....	15
CHAPTER 2	18
Theory and Simulation of Planar Micro-Optic Solar Concentrators	
2.1. CONCEPTS.....	18

2.2. CONCENTRATION RATIO AND OPTICAL EFFICIENCY	20
2.3. COMPONENT DESIGN	22
2.3.1. Lens F-number	22
2.3.2. Waveguide Materials	24
2.3.3. Waveguide Coupling.....	25
2.3.4. 120° Coupling Prisms	26
2.3.5. Self-Alignment.....	28
2.4. ANALYTIC MODEL.....	29
2.5. CONCENTRATOR SIMULATIONS	32
2.5.1. Designs.....	32
2.5.2. Performance	33
2.5.3. Output Characteristics	35
2.5.4. Angular Acceptance	36
2.6. EQUIVALENT DESIGNS	38
2.7. SUMMARY	38
2.8. REFERENCES.....	39
 CHAPTER 3	41
Self-Aligned Fabrication and Experimental Testing of Concentrator Prototypes	
3.1. SELF-ALIGNED FABRICATION	41
3.1.1. SU-8 Photoresist Molding.....	43
3.1.2. UV Illumination	45
3.1.3. Coupler Metallization and Development	47
3.2. EXPERIMENTAL DESIGNS.....	48
3.2.1. First-Generation System	48
3.2.1.1. f/1.1 Lens Array	48
3.2.1.2. Simulation	49
3.2.2. Second-Generation Design.....	50
3.2.2.1. f/3 Lens Array	50
3.2.2.2. Simulation and Comparison	51
3.3. FIRST-GENERATION PROOF-OF-CONCEPT.....	52
3.3.1. Fabrication Results.....	52
3.3.2. Optical Efficiency	53
3.3.3. Angular Acceptance	55
3.4. SECOND-GENERATION PROTOTYPE	57
3.4.1. Fabrication Results.....	57
3.4.2. Efficiency Measurements.....	58
3.4.3. Spectral Performance	59
3.5. EXPERIMENTAL LOSSES.....	60
3.5.1. Coating Reflectivity	60
3.5.2. Edge Coupling Loss	61
3.5.3. Revised Simulations.....	62
3.6. SUMMARY	63
3.7. REFERENCES.....	64
 CHAPTER 4	66
Increased Concentration Ratios Using Orthogonal Waveguides and Secondary Optical Elements	
4.1. INTRODUCTION	66
4.2. CONCENTRATION LIMITS.....	67
4.2.1. Angular Spectrum	67

4.2.2. Micro-Optic Concentrator Output	68
4.3. ORTHOGONAL WAVEGUIDE CONCENTRATION	69
4.3.1. V-Trough Waveguide	69
4.3.2. Lens-Mirror Combination	71
4.3.3. Orthogonal Waveguides at the Concentration Limit.....	72
4.3.4. Simulation	74
4.3.5. Sidewall Reflection	76
4.3.6. f/3 System Example	77
4.4. SECONDARY OPTICAL ELEMENT.....	79
4.4.1. Design	79
4.4.2. Simulated Performance	81
4.5. HIGH-CONCENTRATION SYSTEM DESIGNS	82
4.5.1. Improved Efficiency	82
4.5.2. Spectral Separation	83
4.5.3. Combining Orthogonal and SOE Concentration.....	84
4.6. ORTHOGONAL WAVEGUIDE PROTOTYPE	86
4.6.1. Sectioned Waveguide.....	86
4.6.2. Experimental Results	87
4.7. SUMMARY	90
4.8. REFERENCES.....	91
CHAPTER 5	93
Conclusions and Future Directions	
5.1. FUTURE DIRECTION: CONFORMAL CLADDING	97
5.2. FUTURE DIRECTION: LATERAL MICRO-TRACKING	98
APPENDIX A	101
Example Zemax Nonsequential Lens Prescription	
APPENDIX B.....	109
Self-Aligned Fabrication Process	
APPENDIX C	112
Integrated Diffractive Shearing Interferometry for Adaptive Wavefront Sensing	
APPENDIX D	122
Multiband Solar Concentrator Using Transmissive Dichroic Beamsplitting	

List of Figures

Figure 1.1 Multijunction solar cell efficiency (purple) has rapidly progressed compared to other PV technologies. Current record cells exceed 41% conversion efficiency under concentrated sunlight [10]. <i>Figure courtesy of NREL</i> .	3
Figure 1.2 Sunchart for San Diego, CA [17].	6
Figure 1.3 Commercial CPV approaches using a single large aperture (a) and segmented arrays of miniaturized optics (b) [21][22].	8
Figure 1.4 Individual secondary optics require multiple PV cells (a). A slab waveguide captures sunlight from all apertures to a single cell (b). Waveguides enable highly-segmented apertures without additional components (c). Arrows indicate output apertures.	9
Figure 1.5 Lossless propagation requires an increase in modal volume (a). Light within planar waveguides may strike subsequent couplers and decouple as loss (b).	11
Figure 1.6 Continuous roll-processing concept for planar micro-optic solar concentrators.	13
Figure 2.1 Micro-optic concentrators consist of a lens array, waveguide and localized coupling regions (a). Incident sunlight focuses onto the waveguide back surface (b). Coupling regions inject light into the waveguide which exits the slab edge (c).	20
Figure 2.2 Guided light striking a downstream coupler is stripped from the waveguide.	22
Figure 2.3 Glass waveguide materials provide superior transmission through 200mm compared to polymer optics.	25
Figure 2.4 The lens focal length and acceptance angle define the coupler size (a). With 120° prisms, on-axis rays reflect at 60°. Grazing incidence at the adjacent prism (red ray) matches the angle of the opposite marginal ray (green ray) (b).	27
Figure 2.5 120° coupling prisms illuminated from external incidence angles (a). The geometry reflects a wide range of angles into guided modes (b).	28

Figure 2.6 Waveguide geometry defines the optical path length to the output.	29
Figure 2.7 Micro-optic concentrators must balance concentration ratio and optical efficiency. For f/3 lenses coupling with 120° prisms, several length and thickness combinations reach >90% optical efficiency.....	31
Figure 2.8 Optical layout of simulated air-clad and fluoropolymer-clad systems.	34
Figure 2.9 Optical efficiencies of air- and fluoropolymer-clad designs as functions of concentration ratio.	34
Figure 2.10 Spectral performance for air- and fluoropolymer-clad simulations at 300x geometric concentration. AM1.5 solar spectrum (grey line) is plotted on the right axis.	35
Figure 2.11 Propagation through the waveguide results in uniform intensity at the output.	36
Figure 2.12 Increasing the coupling area adds angular acceptance at the cost of optical efficiency (a). At 300x, the efficiency drops by 22% (b).	37
Figure 2.13 The cladding thickness or lens aperture can be altered for a given f-number and yield identical performance.	38
Figure 3.1 Self-alignment molds coupling regions within SU-8 photoresist. The lens array focal plane acts as the lithography mask during exposure.	42
Figure 3.2 50µm pitch 120° coupling prisms molded in SU-8 photoresist. Residual solvent becomes trapped beneath plastic molds (a) while PDMS molds allow the solvent to diffuse into the material for accurate replication (b).	44
Figure 3.3 Optical layout of the UV illumination source with adjustable divergence.	45
Figure 3.4 UV illumination system for self-aligned fabrication (a). Source divergence closely matched the extent of the sun (b).	46
Figure 3.5 Prior to development, SU-8 is coated with an aluminum reflector (a). Using heat and ultrasonic agitation, uncured regions are removed, leaving behind cross-linked prism regions (b).	48
Figure 3.6 Image showing the sag of the f/1.1 plano-convex lens array (a). Gaps between lens elements reduced the array fill-factor (b).	49
Figure 3.7 Second-generation plano-convex f/3 lenses (a). Reduced surface sag avoided gaps between hexagonally-packed elements (b).	50

Figure 3.8	Layouts of the optimized air-clad design and the first- and second-generation prototype designs (a). Simulated efficiencies are traced as functions of concentration ratio (b). (© 2010 IEEE).	51
Figure 3.9	Patterend couplers on the waveguide surface using self-aligned fabrication (a). Couplers were spaced in a hexagonal array defined by the lens array (b). 120° prisms molded into SU-8. Lens aberrations increased the coupler size (c,d).	53
Figure 3.10	Fabricated first-generation concentrator under test (a). When aligned, coupled light appears as a bright line emitting form the edge (b). An unsaturated false color image shows intensity uniformity (c).	54
Figure 3.11	Angular acceptance measured through lateral translation (a). When aligned to the source with $\pm 1.0^\circ$ accuracy, light efficiently couples to the output (b).	56
Figure 3.12	Outdoor demonstration using the first-generation proof-of-concept.	56
Figure 3.13	Thousands of coupling regions appear on the waveguide surface, yet occupy only a fraction of the total area (a). Molded and reflective 120° prism couplers match the hexagonal lens layout (b). Improved lens performance leads to well-defined couplers (c).	58
Figure 3.14	Second-generation concentrator under test (a). A multijunction solar cell measured output flux (b). Bright, uniform light exits the slab edge (c).	59
Figure 3.15	Measured input and output spectrums of the concentrator.	60
Figure 3.16	Aluminum reflectivity was measured by comparing refelction from a TIR (a) and coated prisms (b).	61
Figure 3.17	$f/3$ lenses could focus to 40 μm , but resulted in edge coupling losses (a). Reducing prism pitch minimizes such losses (b).	62
Figure 3.18	Prism pitches much smaller than the coupler reduce coupling losses, highlighted in red (a). Simulations were updated to include mirror reflectivity and coupling loss (b).	63
Figure 4.1	Generalized concentrator defining apertures and output angles.	67
Figure 4.2	Light exiting the waveguide is biased at $\pm 30^\circ$ (a). Output angles span a small percentage of the available angular spectrum (b).	69

Figure 4.3	The concentration ratio for rectangular waveguides is only a function of length and thickness (a). Angling the sidewalls imparts additional concentration along the waveguide width (b).	71
Figure 4.4	The lens-mirror combination proposed by Collares-Pereira et. al. The system is thermodynamically-limited when edge rays approach $\pm 90^\circ$ and define the output boundaries.	72
Figure 4.5	Geometry of the orthogonal waveguide concentrator, noting key dimensions including waveguide width, length and trough angle.	73
Figure 4.6	Lens array f-number limits maximum orthogonal concentration factor. ...	75
Figure 4.7	Systems lose efficiency beyond the maximum orthogonal concentration. All simulations included 200mm long by 1mm thick waveguides.	76
Figure 4.8	Propagating light strikes waveguide sidewalls at skew angles which undergo TIR.....	77
Figure 4.9	Orthogonal waveguide geometries increase the geometric concentration ratio without altering the optical path length or increasing propagation loss...	78
Figure 4.10	Layout of the 8x orthogonal waveguide concentrator (<i>note: system length was reduced for visualization purposes</i>) (a). Concentration along the width increases the angular spectrum in one dimension (b).....	79
Figure 4.11	The SOE was situated between two opposing waveguides and focused to a common output. A nonimaging path allowed downward rays to strike the PV cell directly.	80
Figure 4.12	The SOE designed for f/3 micro-optics with each ray path highlighted (a). The angular spectrum increased by 3.3x in one dimension (b). (© 2010 IEEE).	82
Figure 4.13	The SOE can improve efficiency by shortening the waveguide length while maintaining concentration (a). Optical efficiency improved from 81.9% to 87.5% at 300x.....	83
Figure 4.14	Spectral splitting with dichroic mirrors placed along the slab edges (a) or integrated into the SOEs (b).	84
Figure 4.15	Both orthogonal concentration and waveguide SOEs can be combined into a single system (a). The overall angular spectrum increased 26.4x compared to rectangular waveguides (b).	85

Figure 4.16	Layout of the orthogonal waveguide prototype with assembled linear prism arrays.	87
Figure 4.17	Dicing the waveguide left diffuse sidewalls. Refaceting edges with PDMS index-matched out surface irregularities to yield specular sidewalls. ..	88
Figure 4.18	Fabricated orthogonal waveguide concentrator (a). Experimental system under test (b).	89
Figure 5.1	Conformal claddings enable metallization after development while supporting TIR within planar regions.	98
Figure 5.2	Off-axis lens focus misses waveguide coupling regions (a). Micro-tracking translates the waveguide, repositioning couplers to the shifted lens focus (b).	99

List of Tables

Table 2.1 Effect of lens f-number on marginal ray angles and lens concentration factor.....23

Acknowledgements

First and foremost, I would like to thank my research advisor, Professor Joseph Ford. During my research career at UCSD, Dr. Ford provided limitless guidance, expertise, and inspiration through the many challenges of my work. In addition, many thanks go out to the members of the UCSD Photonic Systems Integration Lab, particularly Dr. Eric Tremblay and Justin Hallas for their countless ideas, discussions and contributions. I would like to acknowledge the hard work and support of the UCSD Nano3 cleanroom staff for their fabrication assistance. I also owe a great deal of thanks to the department, community of students and staff who made UCSD and the city of San Diego such an exceptional place to be.

Finally, I would like to acknowledge my closest friends and family who continue to support me. I am most grateful to Jessica Godin for her companionship and unyielding encouragement throughout. A special thank you goes to my parents Jeff and Diane and to my brother Scott who have been so loving and patient.

The text in Chapter 2 is in part a reprint of material appearing in:

- J. H. Karp, E. J. Tremblay and J. E. Ford, “Planar micro-optic solar concentrator” Opt. Express **18**, pp. 1122-1133 (2010).

The dissertation author was the primary researcher and author.

The text in Chapter 3 is in part a reprint of material appearing in:

- J. H. Karp, E. J. Tremblay and J. E. Ford, “Planar micro-optic concentration using multiple imaging lenses into a common slab waveguide,” Proc. SPIE 7407, 74070D (2009).
- J. H. Karp, E. J. Tremblay and J. E. Ford, “Planar micro-optic solar concentrator” Opt. Express **18**, pp. 1122-1133 (2010).
- J. H. Karp, E. J. Tremblay and J. E. Ford, "Micro-optic solar concentration and next-generation prototypes," 35th IEEE Photovoltaic Specialists Conference (PVSC), vol., no., pp.000493-000497, 20-25 June 2010.

The dissertation author was the primary researcher and author.

The text in Chapter 4 is in part a reprint of material appearing in:

- J. H. Karp, E. J. Tremblay and J. E. Ford, "Radial Coupling Method for Orthogonal Concentration within Planar Micro-Optic Solar Collectors," Optics for Solar Energy, OSA paper STuD2 (2010).
- J. H. Karp, E. J. Tremblay and J. E. Ford, "Micro-optic solar concentration and next-generation prototypes," 35th IEEE Photovoltaic Specialists Conference (PVSC), vol., no., pp.000493-000497, 20-25 June 2010.
- J. H. Karp, E. J. Tremblay and J. E. Ford, “Orthogonal and secondary concentration in planar micro-optic solar collectors,” Optics Express, (*in preparation*).

The dissertation author was the primary researcher and author.

Appendix C is a reprint of prior research pertaining to advancement to candidacy.

The material appears in:

- J. Karp, T. Chan, and J. Ford, “Integrated diffractive shearing interferometry for adaptive wavefront sensing,” *Appl. Opt.* 47, 6666-6674 (2008).

The dissertation author was the primary researcher and author.

Appendix D is a reprint of prior research pertaining to advancement to candidacy.

The material appears in:

- J. H. Karp and J. E. Ford, “Multiband solar concentrator using transmissive dichroic beamsplitting,” *Proc. SPIE* 7043, 70430F (2008).

The dissertation author was the primary researcher and author.

Vita

- 2004 Bachelor of Science in Electrical Engineering
University of Miami; Coral Gables, FL
- 2007 Master of Science in Electrical Engineering (Photonics)
University of California, San Diego; La Jolla, CA
- 2010 Doctor of Philosophy in Electrical Engineering (Photonics)
University of California, San Diego; La Jolla, CA

Journal Publications

J. H. Karp, E. J. Tremblay and J. E. Ford, "Orthogonal and secondary concentration in planar micro-optic solar collectors," *Optics Express (in preparation)*.

B. R. Nadler, J. H. Karp, J. M. Hallas and J. E. Ford, "Planar Micro-Optic Tracking Receiver for Free-Space Data Transmission," *Journal of Lightwave Technology (in preparation)*.

K. Baker, N. Finer, W. Rich, E. Tremblay, J. Karp, and J. Ford, "Anatomy-driven design of a prototype video laryngoscope for extremely low birth weight infants," *Journal of Biomedical Optics* 15(6) (2010).

J. H. Karp, E. J. Tremblay and J. E. Ford, "Planar micro-optic solar concentrator" *Opt. Express* 18, pp. 1122-1133 (2010).

E. J. Tremblay, R. A. Stack, R. L. Morrison, J. H. Karp and J. E. Ford, "Ultrathin four-reflection imager" *Appl. Opt.* 48, pp. 343-354 (2009).

J. Karp, T. Chan, and J. Ford, "Integrated diffractive shearing interferometry for adaptive wavefront sensing," *Appl. Opt.* 47, 6666-6674 (2008).

T. K. Chan, J. H. Karp, R. Jiang, N. Alic, S. Radic, C. F. Marki and J. E Ford, "1092 Channel 2-D demultiplexer for ultralarge data bandwidth," *JLT* Vol. 25 No. 3, 719 (2007).

Conference Proceedings

J. M. Hallas, J. H. Karp, E. J. Tremblay, and J. E. Ford, "Lateral translation micro-tracking of planar micro-optic solar concentrator," Proc. SPIE 7769, 776904 (2010).

J. H. Karp, E. J. Tremblay and J. E. Ford, "Micro-optic solar concentration and next-generation prototypes," 35th IEEE Photovoltaic Specialists Conference (PVSC), vol., no., pp.000493-000497, 20-25 June 2010.

J. H. Karp, E. J. Tremblay and J. E. Ford, "Radial Coupling Method for Orthogonal Concentration within Planar Micro-Optic Solar Collectors," Optics for Solar Energy, OSA paper STuD2 (2010).

B. R. Nadler, E. J. Tremblay, J. H. Karp and J. E. Ford, "Range Finding Using a Masked Folded Optic Imager," Frontiers in Optics (FiO), Paper FWG2, San Jose, CA, October 11-15 2009.

J. H. Karp, E. J. Tremblay and J. E. Ford, "Planar micro-optic concentration using multiple imaging lenses into a common slab waveguide," Proc. SPIE 7407, 74070D (2009).

J. H. Karp and J. E. Ford, "Multiband solar concentrator using transmissive dichroic beamsplitting," Proc. SPIE 7043, 70430F (2008).

J. H. Karp, T. K. Chan and J. E. Ford, "Fourier-Based Diffractive Shearing Interferometer for Wavefront Sensing," The 20th Annual Meeting of the IEEE Lasers and Electro-Optics Society(LEOS), vol., no., pp.165-166, 21-25 Oct. 2007.

Patent

J. E. Ford, J. H. Karp, E. J. Tremblay, and J.M. Hallas, "System and method for solar energy capture and related method of manufacturing", *filed and licensed*

ABSTRACT OF THE DISSERTATION

Planar Micro-Optic Solar Concentration

by

Jason Harris Karp

Doctor of Philosophy in Electrical Engineering (Photonics)

University of California, San Diego, 2010

Professor Joseph E. Ford, Chair

Solar radiation can be converted directly into electricity with materials exhibiting a photovoltaic response. Most photovoltaic arrays use crystalline silicon cells assembled in large modules which convert <20% of incident light into electricity. More recently, multijunction solar cells, comprised of multiple semiconducting layers, have exceeded 41% conversion. The drawback to these devices is the high cost associated with materials and fabrication, making them impractical as rigid panels. The field of concentrator photovoltaics pairs these costly devices with inexpensive collection optics which reduce the amount of active cell area. Most commercial systems rely upon simple lenses or mirrors focusing through secondary optics, yet

these approaches lead to hundreds of individual components which must be assembled, aligned and interconnected.

In this dissertation, I present an alternative concentration approach which replaces discrete optics with a segmented lens array and common slab waveguide. Sunlight collected by each small lens aperture focuses onto mirrors placed on the waveguide surface which reflect rays at angles that guide by total internal reflection. This configuration directs light from thousands of arrayed lenses into the same waveguide which connects to a single photovoltaic cell. We refer to this approach as planar micro-optic concentration because the waveguide remains uniform in cross-section and is compatible with large-scale microfabrication techniques such as roll-to-roll processing.

In the following chapters, I discuss the concept and tradeoffs associated with waveguide coupling and propagation. I present optimized systems which demonstrated >80% optical efficiency at 300x geometric concentration. In addition, I develop a self-aligned fabrication process to assemble several small-scale prototypes using commercially-available components. These systems were experimentally measured at 52.3% optical efficiency. Lastly, I show how the waveguide geometry can be exploited to increase performance and add functionality within concentrator photovoltaic systems.

Chapter 1

Introduction

1.1. Solar Photovoltaics

Semiconducting materials can exhibit a photovoltaic (PV) response which converts absorbed radiation into electric current. Solar PV applies this property to incident sunlight to generate renewable energy. As a resource, more solar energy reaches the earth in one hour than all the energy consumed by mankind in an entire year [1]. Capturing even a small fraction of the 120,000 terawatts of power has proven extremely challenging. Manufacturing and available materials as well as atmospheric conditions affect resource availability and power generation costs. Nonetheless, the capture of solar energy continues to be one of the fastest growing

industries with new materials and optical geometries playing important roles in future system designs.

1.2. Solar Cell Technologies

Solar technologies span a wide range of materials, configurations and manufacturing approaches. Most solar cells rely upon p-n junctions for their built-in electric fields to move photogenerated electrons. Over 50 years ago, Chapin, Fuller and Pearson at Bell Labs demonstrated the first doped silicon solar cell with 6% conversion efficiency and laid the groundwork for future research [2][3]. Today, champion silicon cells eclipse 25% efficiency and approach fundamental material limits of ~30% [4]. Manufactured modules typically operate at ~15% efficiency and account for more than 90% of the 17GW of worldwide PV installations [5].

A new solar cell technology layers III-V semiconductor compounds to capture the entire solar spectrum with conversion efficiencies exceeding 41% [6]. These multijunction solar cells combine as many as three different p-n junctions (GaInP/GaInAs/Ge) positioned in optical series, each responding to specific wavelength bands. Compared to other cell technologies, multijunction cell performance has demonstrated rapid and sustained efficiency improvements through material science and novel cell architectures [7][8][9].

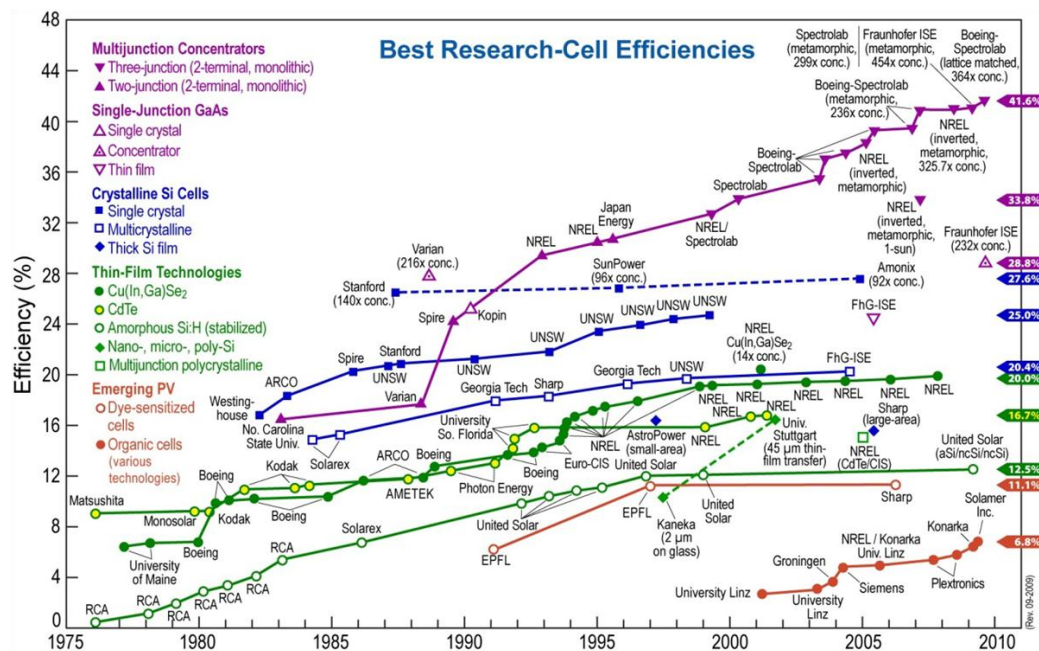


Figure 1.1 Multijunction solar cell efficiency (purple) has rapidly progressed compared to other PV technologies. Current record cells exceed 41% conversion efficiency under concentrated sunlight [10]. *Figure courtesy of NREL.*

1.3. Concentrator Photovoltaics

Multijunction solar cells were originally developed for space applications to maximize power within limited areas. Due to material and fabrication complexity, these cells can be orders of magnitude more expensive than traditional silicon cells, making arrayed modules impractical. For terrestrial applications, large-area optics can be used to collect and deposit solar energy onto small, efficient cells, thereby reducing active cell area. Concentrator photovoltaic (CPV) systems combine collection optics, solar cells and tracking systems to generate solar power. For CPV systems to be cost-effective, the complete cost of these additional components must not exceed the cost savings associated with small area PV cells.

1.3.1. Concentration Ratio

The ratio of collection aperture to cell area is defined as the geometric concentration ratio. CPV designs cover systems with relatively low concentration (<5x) to highly-focused optics reducing cell area by more than 500x. Here, we primarily focus on high-concentration optical designs which integrate with small area cells and mount onto two-axis tracking platforms.

$$C_{geo} = \frac{\text{Output Area}}{\text{Input Area}} \quad (1.1)$$

The second law of thermodynamics states that heat flows from a hot source towards a cooler body. If sunlight were focused onto an arbitrarily small receiver, the temperature at this surface could exceed that the sun itself. A number of proofs identify the concentration limit by generalizing heat flow from one body to another and equating the surface temperatures [11][12][13].

Geometrical optics describe the same conservation of flux using the ideal sine brightness equation, Eq. 1.2 [14]. L_1 and L_2 represent the radiance of the source and exit apertures, respectively, and θ_1 and θ_2 define source and output radiation cone angles. When $L_1=L_2$, the entrance and exit apertures reach the same cumulative flux and the output beam area decreases in exchange for an equal increase in angle. At the thermodynamic limit, maximum output angles (in air) reach $\pm 90^\circ$ and the concentration factor reduces to Eq. 1.3.

$$C = \frac{L_2 \sin^2 \theta_2}{L_1 \sin^2 \theta_1} \quad (1.2)$$

$$C_{limit} = \frac{1}{\sin^2 \theta_1} \quad (1.3)$$

The sun has a diameter of 13.9×10^5 km and sits 14.9×10^7 km from the earth [15]. This geometry causes the sun to appear as a disk with an angular extent of $\pm 0.26^\circ$. From Eq. 1.3, the thermodynamic limit of concentration for a point focus system is 48,562. If the concentrator instead focuses to a line, the *sine-squared* term is replaced by *sine* and the limit drops to 220.

1.3.2. Acceptance Angle

Concentration ratio and angular acceptance are related by étendue which states the entrance pupil multiplied by the solid angle of the source cannot increase within any optical system [16]. From this basic principle, solar concentrators must increase the angular spectrum at the output in order to focus onto cells smaller than the input area. CPV often incorporates mechanical tracking to maintain alignment to the sun. Concentration at the thermodynamic limit requires perfect alignment without any angular tolerance beyond the solar disk.

To understand tracking needs, we first investigated the sun's motion in terms of polar angles. Solar azimuth defined the location of the sun along the horizon and elevation angles specified the height in the sky. Suncharts plot azimuth versus elevation angles to depict both daily and seasonal variations. The sunchart in Figure

1.2 shows the yearly sun angles for San Diego, CA. At this latitude, azimuth angles sweep 240° across the horizon and elevation angles peak at 81° . Precision two-axis tracking mechanics which follow these wide ranges can be both complex and costly. Practical CPV designs extend the angular acceptance to manage fabrication imperfections, component alignment and mechanical flex from windloading. Commercial CPV systems often accept between $\pm 0.5^\circ$ and $\pm 2.0^\circ$ and lowers the concentration ratio to 250-1500x.

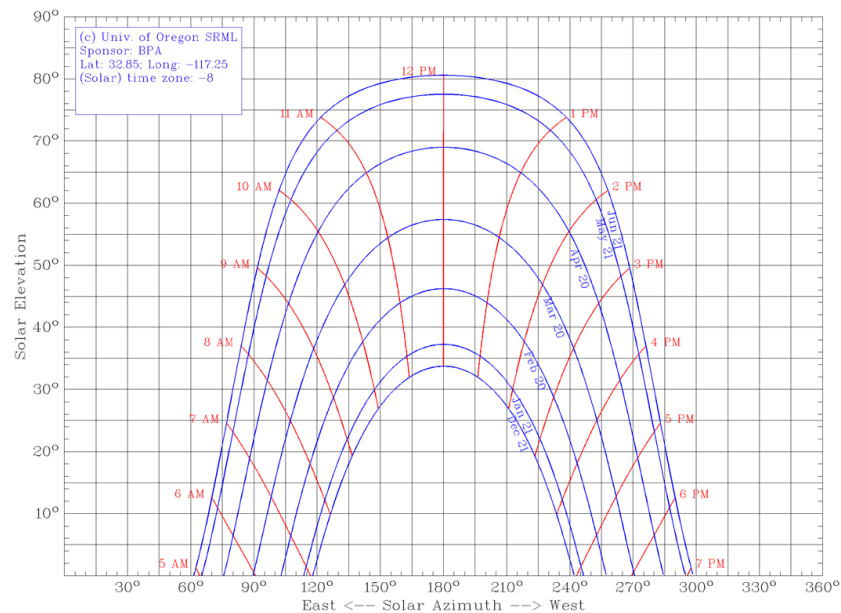


Figure 1.2 Sunchart for San Diego, CA [17].

1.3.3. System Aperture

Concentrator optics typically use primary collection apertures to capture large amounts of sunlight. Common imaging primaries such as Fresnel lenses or parabolic mirrors focus onto nonimaging secondary optics which homogenize focused intensity

prior to absorption by the PV cell. Focusing lenses and mirrors are often characterized by the ratio of their focal length f to the entrance pupil diameter D . The focal ratio, or f-number ($f/\#$), is expressed in Eq. 1.4. The f-number quantifies the light-gathering ability and the spatial resolution of the lens. Eq. 1.5 relates the Rayleigh resolution criteria using the lens f-number at a given wavelength λ [18]. High-collection optics approaching $f/1.0$ theoretically focus to very small output apertures, but geometric aberrations scale inversely with f-number and degrade resolution. Low f-number systems incorporate multiple surfaces and materials to balance aberrations which add significant complexity and cost. Incident field angles and aberrations dominate image formation with minimal influence coming from lens diffraction.

$$f/\# = \frac{f}{D} \quad (1.4)$$

$$resolution = 1.22 \cdot \lambda \cdot f/\# \quad (1.5)$$

Optics for solar energy inherently require large apertures in order to capture significant quantities of sunlight. Due to practical f-number and aberration bounds, increased lens diameter also leads to longer focal length optics. For apertures on the order of meters, the optical track occupies significant optical volume and can be extremely expensive to fabricate as indicated by astronomical telescopes. Furthermore, bulky optics complicate mounting and tracking due to their mass and windload.

An alternate design approach segments the large upward-facing primary into several smaller apertures, each focusing onto their own secondary optics and solar

cells. This transforms the optical volume into a thin system which can be manufactured in a factory instead of assembled on site from large individual components. CPV suppliers are currently manufacturing these types of systems, however, integrating hundreds of small PV cells to their respective optics leads to large-scale connectivity and alignment concerns [19][20].

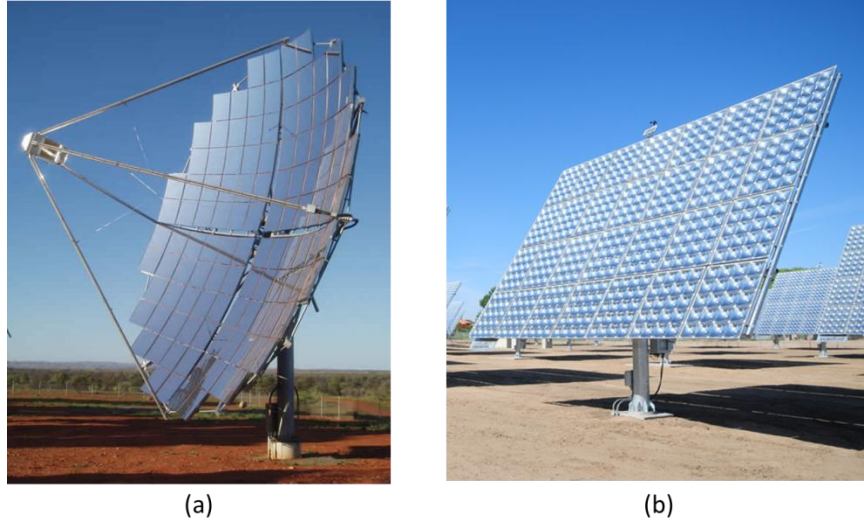


Figure 1.3 Commercial CPV approaches using a single large aperture (a) and segmented arrays of miniaturized optics (b) [21][22].

1.4. Waveguide Concentration

Instead of miniaturizing all components in segmented designs, individual secondary optics can be replaced with a common slab waveguide. Lenses focusing onto coupling regions visible from within the waveguide redirect light at angles which guide by total internal reflection (TIR). The waveguide transports sunlight collected by each divided aperture to a common output located at the slab edge(s). Segmenting the primary into thousands of millimeter-sized elements reduces the optical volume

beyond what is practically possible through pairing individual optics and cells. Long waveguides provide large collection apertures in a thin geometry which simplifies mounting and tracking. A single PV cell attaches along the waveguide edges(s) which reduces connection complexity and allows one heat sink to manage the entire thermal load.

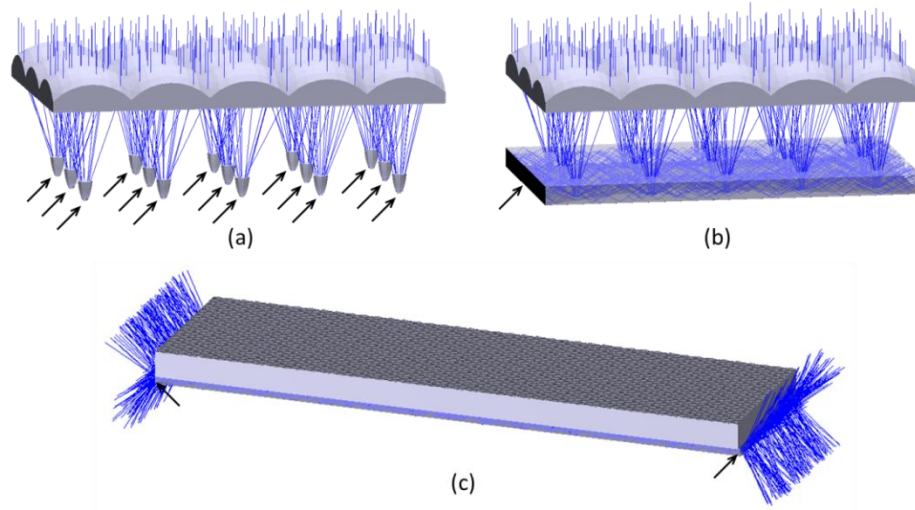


Figure 1.4 Individual secondary optics require multiple PV cells (a). A slab waveguide captures sunlight from all apertures to a single cell (b). Waveguides enable highly-segmented apertures without additional components (c). Arrows indicate output apertures.

1.4.1. Total Internal Reflection

Waveguiding relies upon TIR to confine coupled light within a dielectric medium. From Snell's Law, light traveling from a denser to less dense medium completely reflects when the refraction angle becomes parallel to the interface. This critical angle signifies the minimum angle for TIR with respect to the boundary normal. Unlike metallic mirrors, TIR is a complete reflection with no spectral or polarization-dependent losses [23]. Eq. 1.6 calculates the critical angle for $n_1 > n_2$.

$$\theta_{critical} = \sin^{-1}\left(\frac{n_2}{n_1}\right), \text{ for } (n_1 > n_2) \quad (1.6)$$

The refractive index contrast between the waveguide core and surrounding cladding dictates ray angles which guide by TIR. The acceptance angle of the waveguide can be written in terms of numerical aperture (NA) in Eq. 1.7. Waveguides for solar energy often use air or low-index polymer claddings to achieve very large index contrasts ($\Delta n=0.2$ to 0.5) which support a wide range of coupled ray angles.

$$NA = n \sin \theta = \sqrt{n_{core}^2 - n_{cladding}^2} \quad (1.7)$$

1.5. Waveguide Types

1.5.1. Tapered Guides

We can draw a parallel between waveguide concentrators and flat panel backlights which mount light sources to a waveguide edge and use surface scattering regions to emit out the planar face. These systems typically taper the waveguide thickness to gradually increase angles within the slab to promote scatter for illumination [24]. The backlight can be redesigned and reversed to act as a concentrator by using the wedge to promote TIR and propagation [25]. Variations of this tapered waveguide geometry is nearing commercialization for CPV applications [26].

Tapered guides initially appear attractive because coupling and lossless propagation only occurs with an increase in modal volume. Expanding tapers or

stepped-thickness waveguides tilt light further down the waveguide axis, reducing interaction at the surfaces. Though very efficient, tapered guides also reduce the concentration ratio by growing the output area and decreasing the angular spectrum. Fabrication of these three-dimensional structures requires complex molding using select polymer or glass materials. Altering the waveguide thickness limits the aspect ratio and the maximum length of the concentrator, leading to similar assembly and integration concerns associated with segmented apertures.

1.5.2. Planar Guides

Planar waveguides maintain uniform cross-sections and are unlimited in terms of physical length. These systems rely upon localized coupling regions to inject light into the guide. Coupling regions appear as defects on the waveguide surface which also effect propagation. Due to the parallel waveguide surfaces, guided rays can strike a downstream coupling region and decouple as loss. The number of TIR interactions associated with propagation to the output determines the likelihood of decoupling and overall optical efficiency.

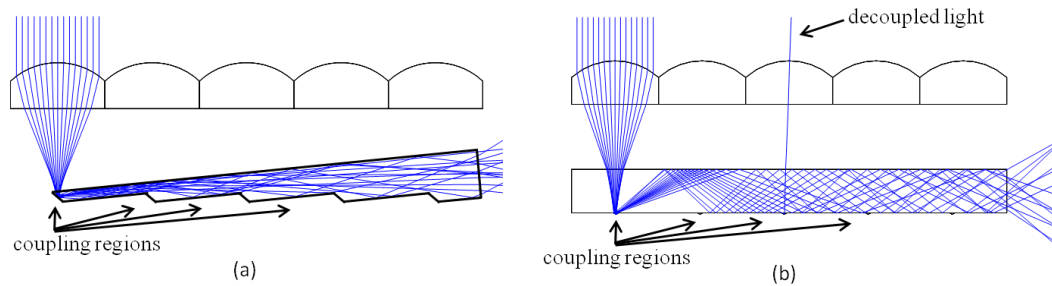


Figure 1.5 Lossless propagation requires an increase in modal volume (a). Light within planar waveguides may strike subsequent couplers and decouple as loss (b).

One approach to subsequent coupler interaction adds a bypass element to divert light around the coupling region through grazing incidence reflection [27]. Bypass elements enable a one or more coupler interactions before reflecting at angles which are no longer supported by TIR. Efficient guiding occurs over a limited length and expands the angular spectrum without adding to the concentration ratio.

Our preferred embodiment manages decoupling loss by minimizing the area occupied by coupling regions. A lens array placed above the waveguide focuses incident sunlight onto very small area coupling regions which can cover $<0.1\%$ of the waveguide surface. We refer to this geometry as planar micro-optic concentration. Shrinking coupling regions reduces the probability of downstream interaction and enables very high (but not lossless) propagation over large dimensions. Lens array f-number, coupling mechanism and waveguide geometry play important roles in defining the optical path length and resulting efficiency.

1.6. Project Goals

For CPV to significantly reduce the cost of solar energy, the cost of optics and mechanics must be as low as possible. Our primary design constraint limited systems to be compatible with a roll-process manufacturing platform, as opposed to individual molding and assembling of parts. Roll processing can perform a range of basic functions on rigid or flexible substrates such as embossing of refractive or diffractive structures, dielectric and metallic deposition and the joining of multiple processed layers [28]. Unlike any other fabrication approach, roll processing produces optics at

an unprecedented volume allowing the cost of the final product to approach that of the raw materials.

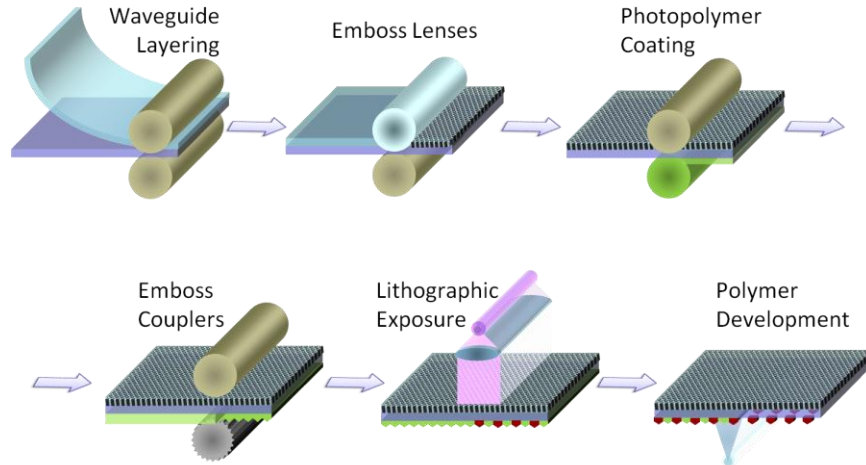


Figure 1.6 Continuous roll-processing concept for planar micro-optic solar concentrators.

Roll-processing restricts optics to planar substrates without critical component alignments. The overall project goals consisted of the design, fabrication and test of high-concentration solar collectors with large input apertures in thin form factors which were compatible with roll-processing. Within this dissertation, I present the basic layout consisting of simple singlet lenses, planar glass waveguides and localized coupling regions. Appropriate design of each element enables both high concentration and high optical. I describe two experimental prototypes fabricated using a unique, self-alignment approach based upon photolithography. The performance of each concentrator was tested and fully characterized. Planar micro-optic concentrators also support complimentary methods of increased concentration without adding propagation loss. I explore concentration along the waveguide width as well as the design of secondary optical elements. Lastly, the layered structure enables a degree to

optical tracking through simple translation. I investigate these future directions in extended angular acceptance and micro-tracking.

1.7. Dissertation Outline

This dissertation explores design tradeoffs, fabrication processes and performance limits associated with planar micro-optic solar concentration. To these ends, this dissertation is organized as follows:

- In Chapter 2, I detail the micro-optic concentrator layout and associated components. The interplay of materials, lens f-number and coupling geometry effect the overall system performance. I present an analytic model based on optical path length to define appropriate waveguide dimensions. Full Zemax ray tracing simulations highlight attainable efficiency and concentration values for selected system geometries.
- In Chapter 3, I present the design, fabrication and test of two proof-of-concept concentrators. Couplers were defined using a self-aligned fabrication process where the lens focal plane acted as a lithography mask. First- and second-generation prototypes were assembled from commercially available components and characterized in terms of optical efficiency, acceptance angle and intensity uniformity. I identify experimental loss mechanisms and propose future modifications to improve performance.

- In Chapter 4, I discuss approaches to further increase concentration while maintaining efficiency. Modifying the geometry confines coupled sunlight along the waveguide width and secondary optics join multiple systems to a common output. Concepts of étendue and angular spectrum highlight concentration limits which are used to evaluate each concentration approach. I also fabricate and test a simplified concentrator based upon these designs.
- Finally, in Chapter 5, I summarize the major contributions of this work and present future research directions.

1.8. References

- [1] O. Morton, "Solar energy: a new day dawning? Silicon Valley sunrise," *Nature* **443**, 19-22 (2006).
- [2] D. M. Chapin, C. S. Fuller, and G. L. Pearson, "A New Silicon p-n Junction Photocell for Converting Solar Radiation into Electrical Power," *Journal of Applied Physics* **25**, 676 (1954).
- [3] J. Perlin, "The Silicon Solar Cell Turns 50," National Renewable Energy Laboratory (2004).
- [4] W. Shockley and H. J. Queisser, "Detailed Balance Limit of Efficiency of p-n Junction Solar Cells," *Journal of Applied Physics* **32**, 510 (1961).
- [5] Ren21, Renewables 2009 Global Status Report.
http://www.ren21.net/Portals/97/documents/GSR/RE_GSR_2009_Update.pdf
- [6] M. A. Green, K. Emery, Y. Hishikawa, and W. Warta, "Solar cell efficiency tables (version 35)," *Progress in Photovoltaics: Research and Applications* **18**, 144-150 (2010).
- [7] S. Michael, A. Bates, and M. Green, "Silvaco ATLAS as a solar cell modeling tool," 33rd IEEE Photovoltaic Specialists Conference, 719-721 (2005).

- [8] M. McDonald, "Spectral efficiency scaling of performance ratio for multijunction cells," in *2009 34th IEEE Photovoltaic Specialists Conference (PVSC)* (IEEE, 2009), pp. 1215-1220.
- [9] D. J. Friedman, J. F. Geisz, S. R. Kurtz, and J. M. Olson, "1-eV solar cells with GaInNAs active layer, "Journal of Crystal Growth **195**, 409-415 (1998).
- [10] S. Kurtz, "Opportunities and challenges for development of a mature concentrating photovoltaic power industry," NREL Technical Report TP-520-43208, Revised November 2009.
- [11] H. Ries, "Thermodynamic limitations of the concentration of electromagnetic radiation, "Journal of the Optical Society of America **72**, 380 (1982).
- [12] A. Rabl, *Active Solar Collectors and Their Applications* (Oxford University Press, 1985).
- [13] W. T. Welford and R. Winston, *High Collection Nonimaging Optics* (Academic Press, 1989).
- [14] G. Smestad, H. Ries, R. Winston, and E. Yablonovitch, "The thermodynamic limits of light concentrators, "Solar Energy Materials **21**, 99-111 (1990).
- [15] R. Foster, M. Ghassemi, and A. Cota, *Solar Energy: Renewable Energy And The Environment* (CRC Press, 2009).
- [16] R. Winston, W. T. Welford, J. C. Miñano, and P. Benítez, *Nonimaging Optics* (Academic Press, 2005).
- [17] Sun Path Chart Program, University of Oregon Solar Radiation Monitoring Laboratory, <http://solar.dat.uoregon.edu/SunChartProgram.html>.
- [18] J. W. Goodman, *Introduction To Fourier Optics* (Roberts and Company Publishers, 2005).
- [19] D. Feuermann, J. M. Gordon, "High-concentration photovoltaic designs based on miniature parabolic dishes," Solar Energy, Vol. 70-5, 423-430 (2001).
- [20] A.W. Bett, C. Baur, F. Dimroth, G. Lange, M. Meusel, S. Riesen, G. Siefer, V. M. Andreev, V. D. Rumyantsev and N. A. Sadchikov, "FLATCONTM -Modules: Technology and Characterisation", WCPEC-3, 634-637 (2003).
- [21] Solar Systems Pty Ltd. http://www.solarsystems.com.au/the_technology.html.
- [22] SolFocus, Inc., http://www.solfocus.com/en/downloads/logos-images/onsite_low/3.jpg

- [23] C. A. Balanis, *Advanced Engineering Electromagnetics* (Wiley, 1989).
- [24] N. Gitkind, B. A. Jacobson, F. J. Scipione, R. D. Gengelbach, R. M. Emmons, and R. L. Holman, "Plastic optics in LCD backlighting," in *Design, Fabrication, And Applications Of Precision Plastic Optics*, SPIE Vol. 2600, pp. 20-26 (1995).
- [25] M. C. Chien, Y. Lung Tung, and C. H. Tien, "Ultracompact backlight-reversed concentration optics," *Applied Optics* **48**, 4142 (2009).
- [26] Morgan Solar Inc., "Light-guide Solar Panel And Method Of Fabrication Thereof," invented by J. P. Morgan, World Intellectual Property Organization, WO/2008/131561 (2008).
- [27] B. L. Unger, G. R. Schmidt, and D. T. Moore, "Dimpled Planar Lightguide Solar Concentrators," in *OSA International Optical Design Conference*, Optical Society of America, ITuE5P (2010).
- [28] M. P. Watts, "Advances in roll to roll processing of optics," *Proceedings of SPIE* **6883**, (2008).

Chapter 2

Theory and Simulation of Planar Micro-Optic Solar Concentrators

2.1. Concepts

The planar micro-optic concentrator acts as a hybrid imaging/nonimaging optical system by combining focusing lens with a multimode slab waveguide. The system consists of three main components. First, a two-dimensional lens array acts as the upward facing aperture to collect incident solar radiation. Each lens forms a demagnified image of the solar disk which subtends $\pm 0.26^\circ$. A dielectric slab waveguide, the second component, sits beneath the lens array. Localized coupling regions embedded on the backside of the waveguide comprise the last component and reorient focused light into guided modes that travel transversely via TIR. The lens

array and waveguide are separated by a low-index cladding region. A large refractive-index contrast between the core and cladding promotes more guided modes and captures steep marginal rays from the lens. The nonimaging nature of the slab allows light from each of the potentially thousands of lens elements to couple into a common optic and propagate to the output(s) at the slab edge(s). With millimeter-sized lenses, the system reduces to a thin, planar profile.

The lens array, waveguide and coupling mechanism must all be designed in concert to ensure efficient coupling and propagation. The focused cone angle and resulting coupled angles must be supported by the waveguide which itself is constrained by available material choices. In this chapter, I discuss the design and tradeoffs between concentration ratio and optical efficiency as well as develop an analytic model to accurately simulate system performance.

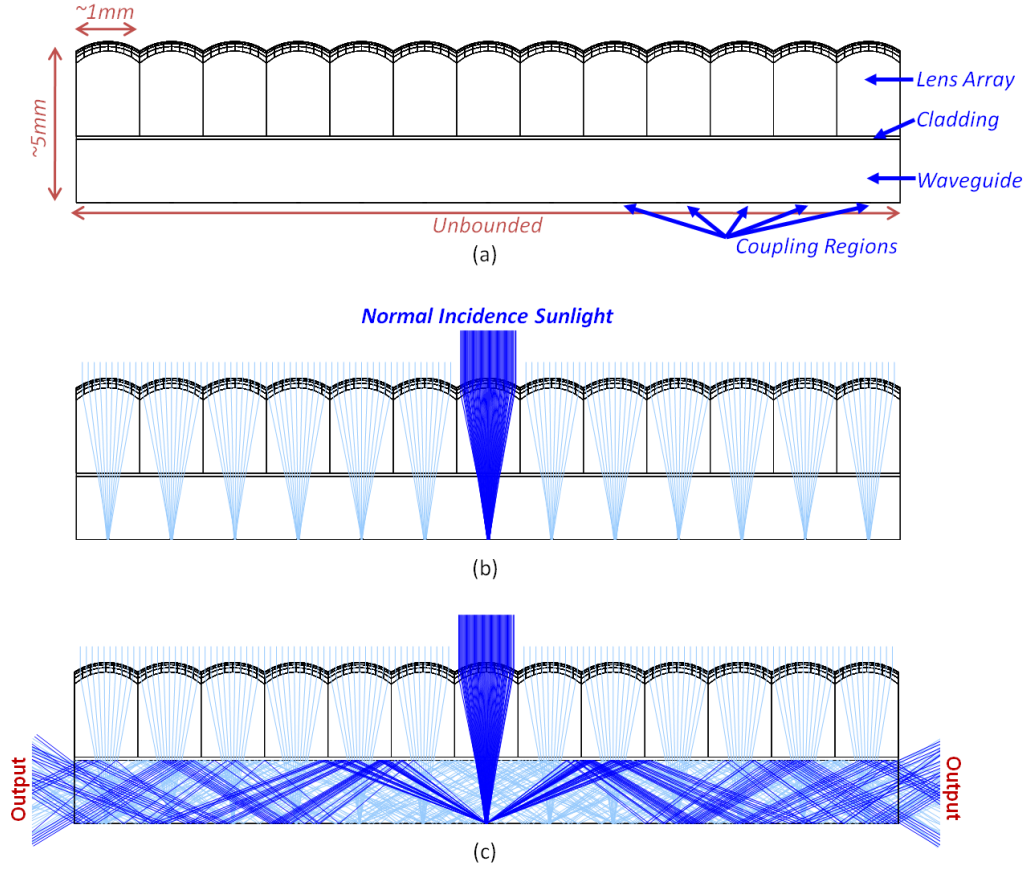


Figure 2.1 Micro-optic concentrators consist of a lens array, waveguide and localized coupling regions (a). Incident sunlight focuses onto the waveguide back surface (b). Coupling regions inject light into the waveguide which exits the slab edge (c).

2.2. Concentration Ratio and Optical Efficiency

The geometric concentration ratio of any CPV system is defined as the ratio of the input to output areas. The input aperture of the micro-optic solar collector consists of the top waveguide area defined by *length* \times *width*. Concentrated sunlight is confined within to two output apertures with areas of *width* \times *thickness*. The geometric concentration ratio is therefore the *length* divided by *two times the thickness*, Eq. 2.1. Placing a mirror over one output reflects all coupled light towards a single

edge and changes the concentration ratio to *length divided by thickness*. As currently described, the concentration ratio has no dependence on waveguide width.

In addition to geometric concentration ratio, optical efficiency η signifies the fraction of incident light reaching the output aperture. Optical efficiency principally includes Fresnel surface reflections, material absorption as well as losses associated with propagation. Eq. 2.2 denotes flux concentration as the product of the geometric concentration ratio and optical efficiency, and indicates light levels present at the output.

$$C_{geo} = \frac{\text{waveguide length}}{2 \cdot \text{waveguide thickness}} \quad (1.8)$$

$$C_{flux} = \eta \cdot C_{geo} \quad (1.9)$$

Planar waveguides maintain a uniform cross-section which allows guided light to interact with downstream coupling regions. Rays which strike subsequent prisms are stripped from the waveguide. The percentage of the waveguide surface occupied by coupling regions determines the probability of propagation loss. We can reduce the impact of this primary loss source by minimizing either the coupling area or the number of waveguide surface interactions. Though extending the waveguide length (or shrinking the thickness) increases the geometric concentration ratio without bound, absorption and propagation loss prevent the output flux from exceeding the thermodynamic limit of concentration.

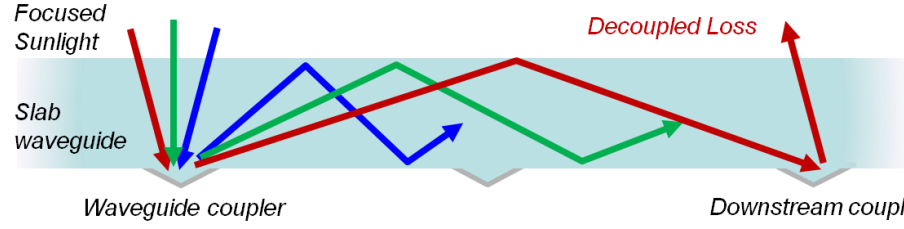


Figure 2.2 Guided light striking a downstream coupler is stripped from the waveguide.

2.3. Component Design

2.3.1. Lens F-number

The focal length and entrance pupil of each lens element affects the size and spacing of coupling regions on the waveguide. For a given acceptance half-angle θ , $2f \tan \theta$ calculates the aberration-free solar image height, where f signifies the lens focal length. By imaging the solar disk, each lens exhibits its own concentration factor expressed by Eq. 2.3, in terms of lens f-number. Inside a dielectric waveguide, C_{lens} is divided by the refractive index. The lens concentration ratio defines the maximum concentration which can occur within a micro-optic system as planar waveguides cannot alter internal ray angles. Table 2.1 shows the relationship between f-number and lens concentration ratio.

$$C_{lens} = \frac{1}{4(f/\# \cdot \tan \theta)^2} \quad (3.1)$$

Table 2.1 Effect of lens f-number on marginal ray angles and lens concentration factor.

Lens f/#	Marginal ray angle in air (°)	C_{lens}
1	28.54	12139.6
2	14.52	3034.9
3	9.78	1348.8
4	7.40	758.7
5	5.98	485.6
6	5.02	337.2
7	4.34	247.7
8	3.83	189.7
9	3.43	149.9
10	3.11	121.4

In optical systems, the marginal ray traces from the edge of the entrance aperture and defines extreme angles which must be coupled into the waveguide. Low f-numbers focus to very small image heights (in the absence of aberration), yet yield steep marginal rays which may be difficult to TIR. Marginal rays also travel along the longest optical path to the output. Steep rays undergo many TIR interactions and have an increased probability of decoupling loss. Conversely, higher f-numbers are easier to guide, yet the associated couplers occupy more surface area which negatively affects propagation efficiency. Lens arrays are typically limited to simple plano-convex profiles that characteristically experience spherical aberration and field curvature. These paraxial deviations cannot be corrected with additional optical surfaces. As we will see in the following sections, most micro-optic concentrators balance lens performance and aberration by selecting optics between $f/2$ and $f/5$.

2.3.2. Waveguide Materials

The index contrast between the waveguide and cladding must support reflected marginal ray angles. Depending on lens f-number and coupling mechanism, rays can approach the waveguide surface at $<40^\circ$ from the surface normal. With air as a cladding medium, many common glass and plastic materials provide index contrasts above 0.5 and support these marginal ray angles for TIR. However, maintaining precision air gaps can be difficult in large-area waveguide concentrators. Low-index claddings such as fluoropolymers can be designed to useful indices around 1.3, versus 1.0 for air [1]. Systems with these claddings can still achieve high contrasts by raising the core material.

Low-cost concentrator optics restricts lenses and waveguides to widely-available materials. Waveguides must also have low absorption coefficients in order to support propagation over several hundred millimeters. Common optical glasses such as BK7 ($n_d=1.516$) exhibit very low absorption coefficients ($\alpha=3\times 10^{-6}\text{cm}^{-1}$) over visible and near infrared wavelengths [2][3]. Flint glasses like F2 ($n_d=1.620$, $\alpha=1.8\times 10^{-4}\text{cm}^{-1}$) increase the index contrast, but also carry higher cost [4]. Regardless of formulation, planar slabs can be manufactured using the float glass process which yields very large, inexpensive glass sheets [5].

Polymer waveguides offer a unique low cost material choice, but cannot match the transparency of glass. Polymethylmethacrylate ($n_d=1.489$), polycarbonate ($n_d=1.586$) and cycloolefin polymers (Zeon Corp, 480R, $n_d=1.525$) characteristically

absorb at near infrared wavelengths which limit their usefulness as waveguides for solar energy [6]. Glass remains the optimum waveguide material due to its exceptional clarity and volume manufacturing approach.

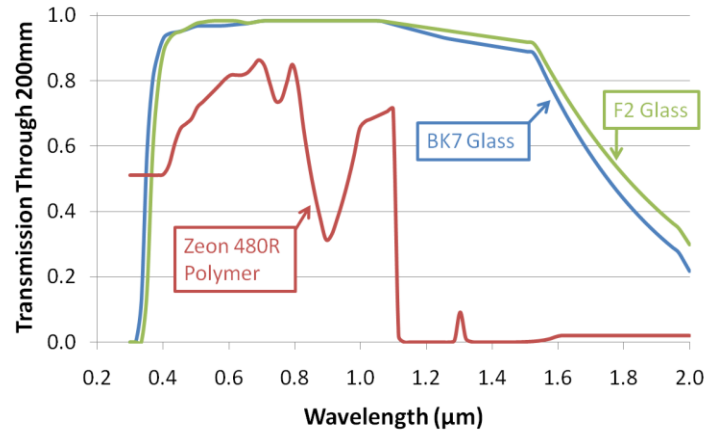


Figure 2.3 Glass waveguide materials provide superior transmission through 200mm compared to polymer optics.

2.3.3. Waveguide Coupling

All waveguide coupling schemes place localized features visible from within the slab to redirect sunlight at angles which exceed the critical angle for TIR. The simplest approach uses diffuse couplers which scatter focused sunlight into the guide. Scattering regions are commonly used in flat panel backlighting, though offer little control over the resulting ray angles [7]. Portions of the scattered light may not satisfy TIR and lead to inefficient waveguide coupling. Fluorescent dyes found in luminescent solar concentrators absorb and re-emit light into potentially guided modes [8]. Omnidirectional emission from dye molecules leads to similar coupling inefficiencies associated with diffuse scatter. Gratings and holograms have previously

demonstrated coupling with precise angular control of the diffracted light [9][10]. Diffraction also exhibits strong wavelength dependence, making it poorly suited for directional, broad spectrum sunlight.

Specular surfaces provide clearly defined reflection angles for all wavelengths. TIR-based or coated fold mirrors tilt the entire cone of focused sunlight into the waveguide. Similar surface texturing has been used in PV cell enhancement to extend photon lifetimes within active layers [11]. Marginal rays at the lens focus require the largest tilt to TIR at the core/cladding interface. Increasing the NA of the waveguide allows steeper ray angles to TIR, however, this also increases the optical path length to the exit aperture. Assuming tilted fold mirrors, the reflected angle of the steepest marginal limits the lens f-number for a given waveguide NA.

2.3.4. 120° Coupling Prisms

Large fold mirrors can be collapsed into periodic kinoforms to yield prism arrays. 45° prisms reflect light directly down the axis of the waveguide, providing the shortest optical path length. However, repeating this structure in a triangular or sawtooth manner causes reflected light to immediately strike the adjacent facet and reflect out of the waveguide as loss. To avoid neighboring shadowing effects, a 120°-apex prism array can be used to tilt the focused cone of light by 60° with respect to the top waveguide surface. The steepest marginal ray becomes biased by this reflected angle and influences lens and material selection. 60° reflection reorients normal incidence at an angle exactly parallel to the adjacent facet, thereby avoiding

shadowing effects. Shallower cone angles which happen to strike a neighboring facet reflect at grazing incidence and continue to TIR. Light can strike any portion of the periodic geometry and couple into the waveguide. Prisms can therefore be placed arbitrarily within the lens focus and couple light symmetrically towards two opposing edges.

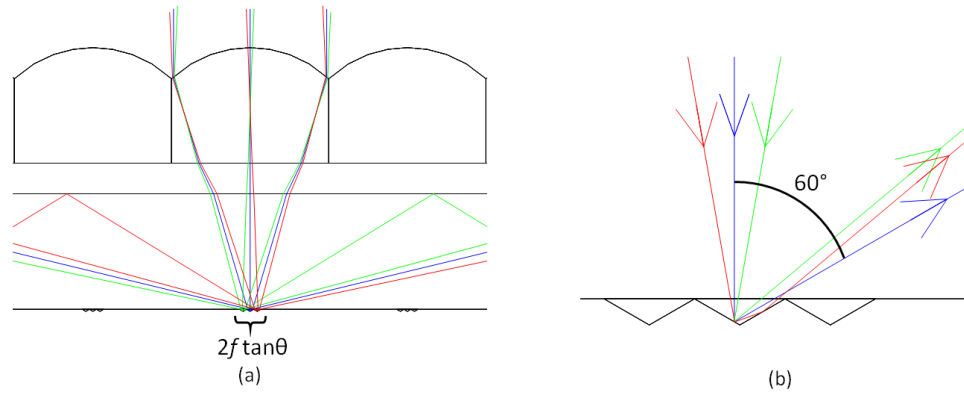


Figure 2.4 The lens focal length and acceptance angle define the coupler size (a). With 120° prisms, on-axis rays reflect at 60°. Grazing incidence at the adjacent prism (red ray) matches the angle of the opposite marginal ray (green ray) (b).

The lens f-number defines the range of focused angles incident on the coupling prisms. To ensure the 120° geometry functioned for a wide range of ray angles, we simulated coupling performance as a function of external incidence angle. Rays perpendicular to the prism direction experienced grazing reflections at shallow angles and began to break TIR at $\pm 38^\circ$. Rays approaching parallel to the prism direction reflect at skew angles and easily couple into the waveguide. These results highlight the robustness of 120° coupling prisms which can be used for a variety of f-number optics and field angles.

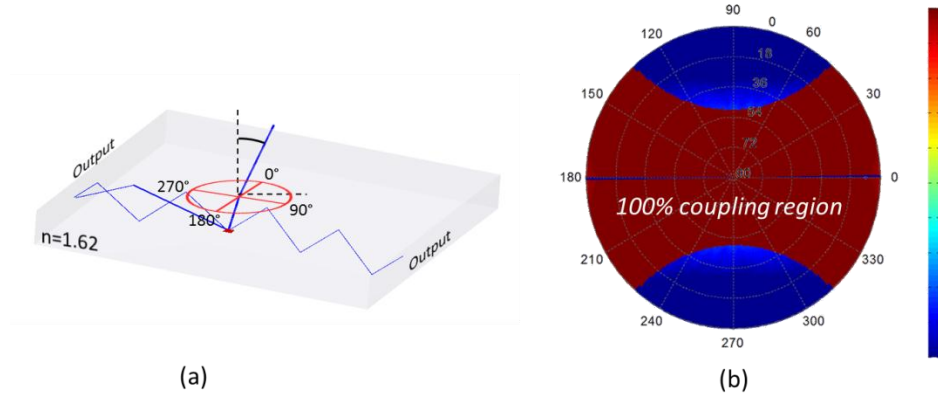


Figure 2.5 120° coupling prisms illuminated from external incidence angles (a). The geometry reflects a wide range of angles into guided modes (b).

2.3.5. Self-Alignment

For efficient coupling, the lens array must be well-aligned to the patterned waveguide. High-concentration systems utilize thousands of coupling areas aligned over hundreds of millimeters. Some example systems must be laterally aligned within $<20\mu\text{m}$ and rotationally positioned with $<0.01^\circ$ couple light efficiently. These tolerances can be prohibitively expensive when performed during assembly.

Instead of actively aligning the lens array and waveguide, a self-aligned fabrication approach can be used to properly position the components during manufacture. The approach molds the coupling prisms within a photosensitive polymer and uses a UV dosage through the lens array to induce cross-linking at the focal plane. After exposure, uncured polymer is removed while the couplers at the focus remain part of the final device. In essence, the lens array focal plane acts as a lithography mask which defines the coupling regions and ensures proper alignment between the components. Self-alignment influenced the choice of 120° coupling

prisms because they can be placed anywhere within the focal region without regard to pitch or position. Self-alignment remains compatible with roll manufacturing techniques and provides a path to large, inexpensive solar concentrators. The details of the fabrication process are described in Chapter 3 and Appendix B.

2.4. Analytic Model

We have developed an analytic model to illustrate the influence of f-number and waveguide geometry on optical efficiency. Consider a light ray which enters a waveguide of length L and thickness H , which couples at position P from the exit aperture. The ray propagates at an angle ϕ with respect to the bottom surface of the waveguide. The ray traverses a distance $2H/\tan\phi$ along the waveguide until interacting with the back surface and may undergo TIR or decouple if striking a subsequent coupler. The total number of surface interactions is inversely proportional to the waveguide thickness and is expressed as $P \tan\phi/2H$. Figure 2.6 graphically depicts the described geometry.

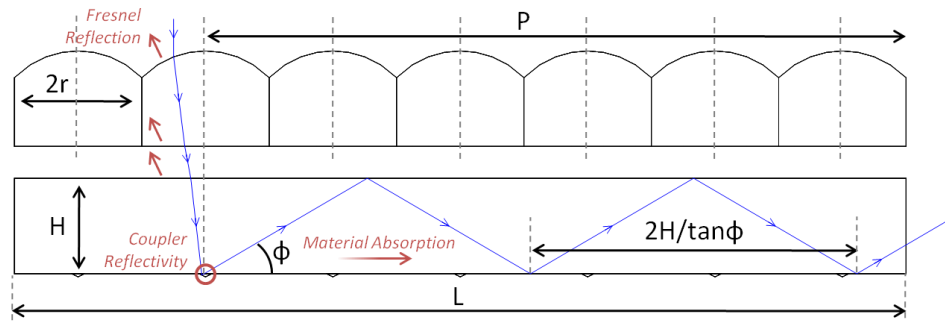


Figure 2.6 Waveguide geometry defines the optical path length to the output.

Starting with only decoupling loss, Eq. 2.4 calculates the optical efficiency at input position P , expressed as the transmission probability raised to the total number of back surface interactions for each angle ϕ . Eq. 2.5 adds Fresnel and mirror reflection losses R as well as material absorption using exponential decay of the path length multiplied by the absorption coefficient α . Eq. 2.6 computes the total optical efficiency by considering the cumulative efficiency from every lens with diameter $2r$, position P and integrated over all coupled ray angles ϕ confined within the waveguide.

$$\eta_{decouple}(P, \phi) = \left(1 - \frac{1}{C_{lens}}\right)^{\frac{P \tan \phi}{2H}} \quad (3.2)$$

$$\eta_{position}(P, \phi) = (1 - R) \cdot \eta_{decouple}(P, \phi) \cdot \exp(-\alpha P \cos \phi) \quad (3.3)$$

$$\eta_{total} = \frac{\sum_P \int_{\phi} \eta_{position}(P, \phi)}{(L - r)/2r}, \quad P = r, 3r, 5r, \dots, (L - r)/2r \quad (3.4)$$

Figure 2.7 plots the optical efficiency as functions of slab length and thickness for a 2mm diameter, f/3 lens coupled into a BK7 waveguide at $\phi = 60^\circ$. Geometries with the highest efficiency and the highest concentration ratio appear at opposite corners of the plot. Short, thick waveguides minimize the number of interactions with the back surface to avoid absorption and decoupling loss, yet provide very little concentration as a result. Conversely, very thin waveguides quickly lose efficiency as the propagation length increases. For a given concentration ratio, any combination of

length and thickness produce identical optical paths to the output and therefore yield matching optical efficiencies.

Micro-optic concentrators must accept some degree of propagation loss in order to collect light from multiple lens apertures. Without any waveguide length, the geometry regresses to a single lens focusing onto a single PV. However, focusing lenses reduce the total surface area occupied by couplers enabling light can undergo thousands of TIR reflections with a low probability of loss. A 600mm long, 1mm thick waveguide yields 300x with >90% of the light reaching the output. Despite the tradeoff between efficiency and concentration ratio, the analytic model shows micro-optic concentrators achieve promising dimensions without significant decreases in efficiency. To accurately calculate system performance, we must expand our model to include all coupled ray angles as well as geometric aberrations and material properties.

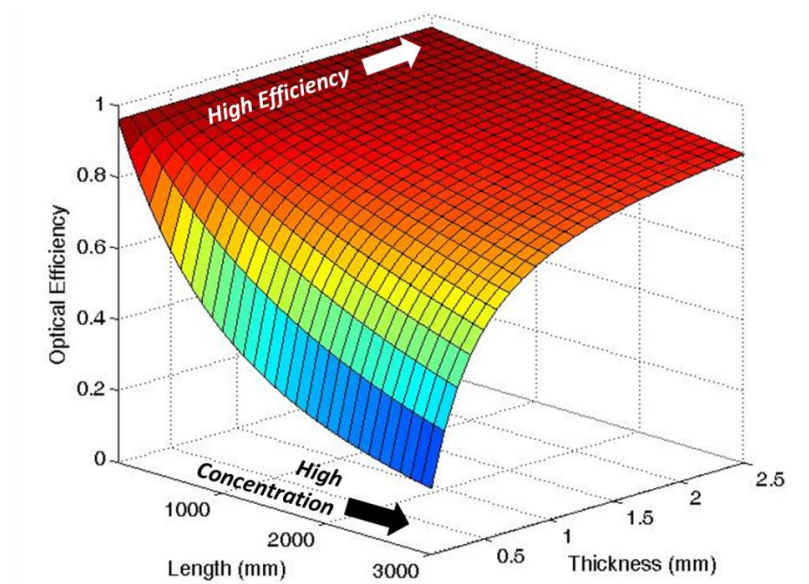


Figure 2.7 Micro-optic concentrators must balance concentration ratio and optical efficiency. For $f/3$ lenses coupling with 120° prisms, several length and thickness combinations reach >90% optical efficiency.

2.5. Concentrator Simulations

We performed Monte Carlo raytracing using Zemax EE nonsequential for two example concentrator systems. Analysis assumed plano-convex refractive lenses forming a focus on the backside of a slab waveguide patterned with 120° coupling facets. Lens aberrations, Fresnel reflections, dispersion and material absorption were included in optical efficiency calculations. Simulations incorporated AM1.5 sunlight from 0.4-1.6 μm and $\pm 0.26^\circ$ field angles.

2.5.1. Designs

The first design simulated a BK7 glass lens array and F2 glass waveguide with a 200 μm air cladding ($n_d=1.0$). All calculations used 1mm thick waveguides and varied the length in order to change the concentration ratio. Couplers used an internal silver reflector (98% reflectivity). Lenses employed a single layer MgF_2 antireflection coating on the first lens surface.

Maintaining a precision air gap between the lens array and waveguide can be difficult over large areas. Practical problems such as moisture and contaminants make air claddings even more challenging to implement. A second concentrator simulation used a low-index fluoropolymer (NuSil Technology, LS-2233, $n_d=1.33$) deposited onto waveguide surface to create a solid cladding layer. We also replaced the glass lens array with a 500 μm thick cycloolefin polymer (Zeon Corp, 480R) molded on top of a BK7 substrate to move closer to a fieldable system.

2.5.2. Performance

Glass waveguides with air claddings supported very low f-number optics which minimized requisite coupling areas. However, geometric aberrations (particularly spherical) associated with plano-convex optics cause the actual spot size to increase for lenses below $f/2.5$. The optimized air-clad system used 2.38mm diameter, $f/2.45$ lenses focusing onto $78\mu\text{m}$ coupling regions. At 73x, the system was 90% optically efficient. The efficiency dropped to 81.9% at 300x geometric concentration. Switching to a fluoropolymer cladding lowered the waveguide NA which impacted the lens f-number. Optimization returned 1.39mm diameter, $f/4.11$ lenses focusing onto $46\mu\text{m}$ coupling regions. 90% efficiency occurred at 49x geometric concentration and 78.5% at 300x.

The air-clad system performed slightly better than the fluoropolymer design because of the lower f-number. Yet both efficiency values were comparable to transmission efficiencies associated with Fresnel lenses, while at 300x, the input aperture was 600mm long and unrestricted in width [12]. Figure 2.8 and Figure 2.9 compare the optical layouts and plots efficiency as a function of concentration ratio, respectively. Note the optical efficiency drops exponentially for increased concentration, though the loss appears almost linear because couplers occupy $<0.1\%$ of the waveguide surface.

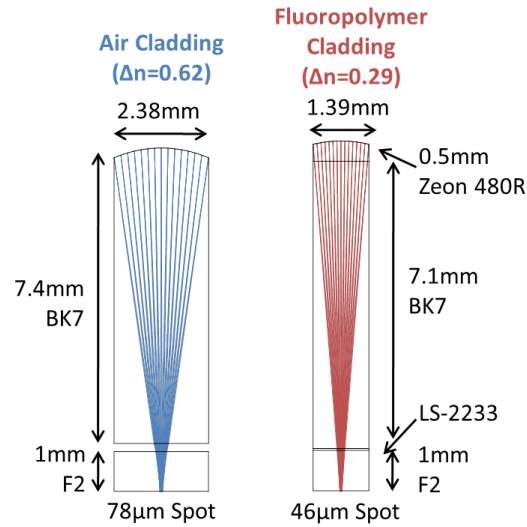


Figure 2.8 Optical layout of simulated air-clad and fluoropolymer-clad systems.

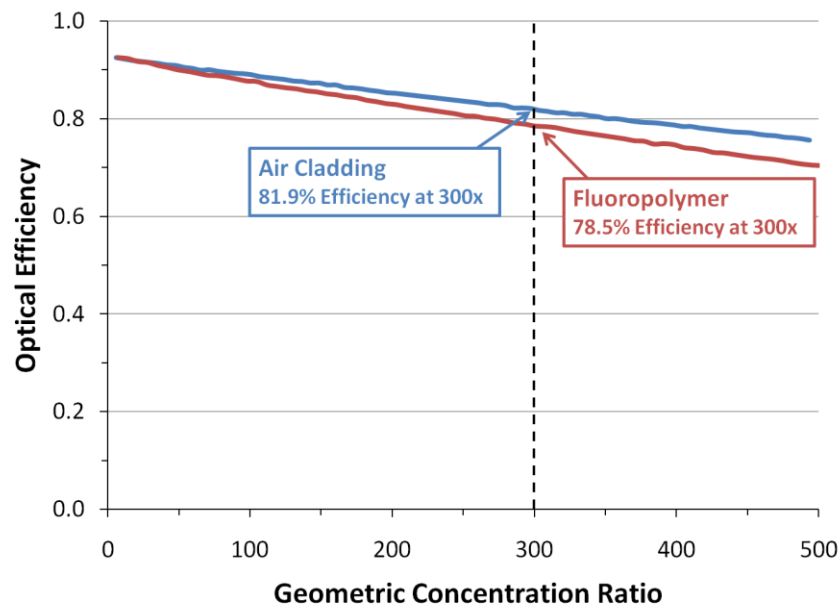


Figure 2.9 Optical efficiencies of air- and fluoropolymer-clad designs as functions of concentration ratio.

Both designs provided excellent coupling and transmission over most of the solar spectrum. Plotting efficiency as a function of wavelength showed 84.8% and 81.4% peak efficiencies for air- and fluoropolymer claddings, respectively. The glass

waveguide was largely transparent from 350nm to 1500nm. We observed higher dispersion within polymer lenses leading to some loss at shorter wavelengths. Material absorption was also evident between 1.1 μm and 1.4 μm and is common among plastic optics. Water vapor causes atmospheric absorption at these infrared wavelengths and negates much of the observed impact [13].

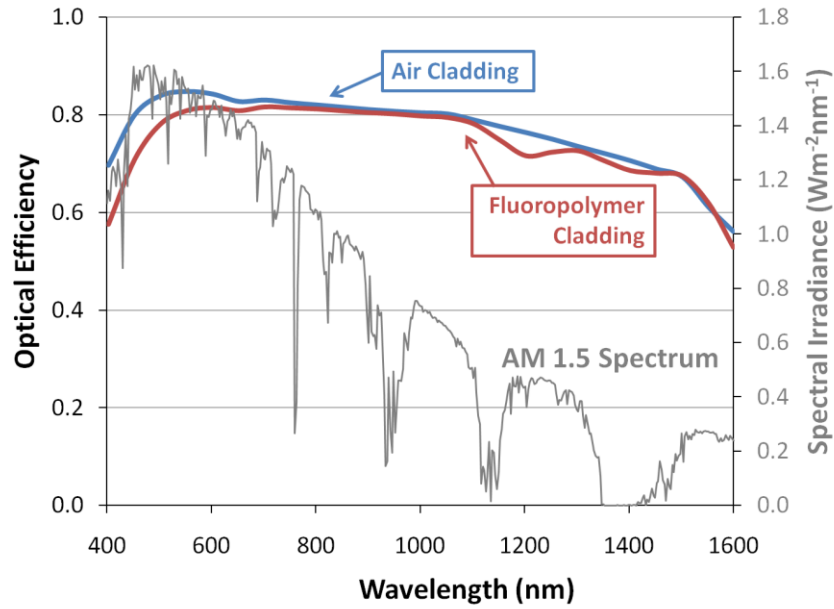


Figure 2.10 Spectral performance for air- and fluoropolymer-clad simulations at 300x geometric concentration. AM1.5 solar spectrum (grey line) is plotted on the right axis.

2.5.3. Output Characteristics

After coupling into the waveguide, light proceeds to diverge as it propagates towards the output edge. Multimode waveguides provide excellent beam homogenization when occupying a high number of supported modes [14]. Eqs. 2.7 and 2.8 estimate the number of waveguide modes, M , from the V -number and index contrast [15]. For a 1mm thick BK7 waveguide with an air cladding, the waveguide

supports over 9000 vertical modes with 500nm light and provides extremely uniform intensity at the output. Figure 2.11 shows minimal spatial intensity variation appearing at the waveguide edge.

$$M = \left(\frac{2V}{\pi} \right) + 1 \quad (3.5)$$

$$V = \frac{\pi \cdot \text{thickness}}{\lambda} \left(n_{\text{core}}^2 - n_{\text{clad}}^2 \right)^{1/2} \quad (3.6)$$

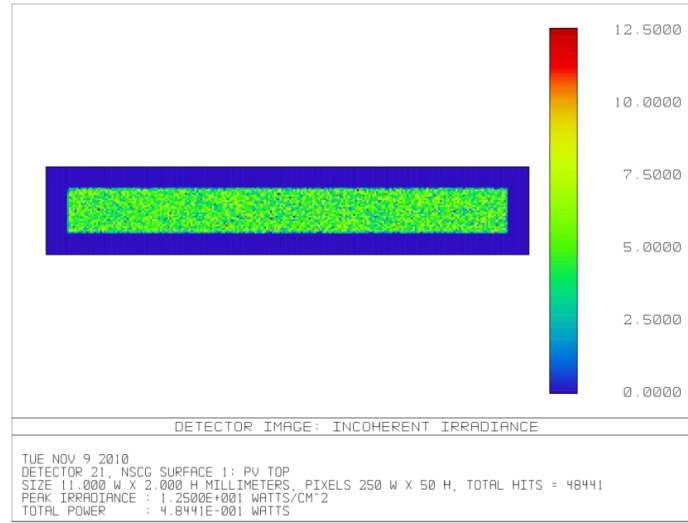


Figure 2.11 Propagation through the waveguide results in uniform intensity at the output.

2.5.4. Angular Acceptance

The angular acceptance of the concentrator depends on the coupler size compared to the demagnified image at the lens focus. When the coupling area matches the $\pm 0.26^\circ$ image height, the concentrator must be exactly normal to the sun's position. Though very efficient, this configuration is intolerant to tracking

misalignments. Oversized coupling regions extend the angular acceptance by allowing the focus to remain incident on the coupler despite alignment changes. Larger coupling regions also increase the likelihood of waveguide decoupling which adversely impacts optical efficiency. Figure 2.12 plots the optical efficiency versus geometric concentration ratio for the $f/2.45$ air-clad concentrator. $78\mu\text{m}$ coupling regions yielded $\pm 0.26^\circ$ solar acceptance while $156\mu\text{m}$ regions provided $\pm 0.63^\circ$. At 300x, the larger coupling regions cause a 22% reduction in efficiency.

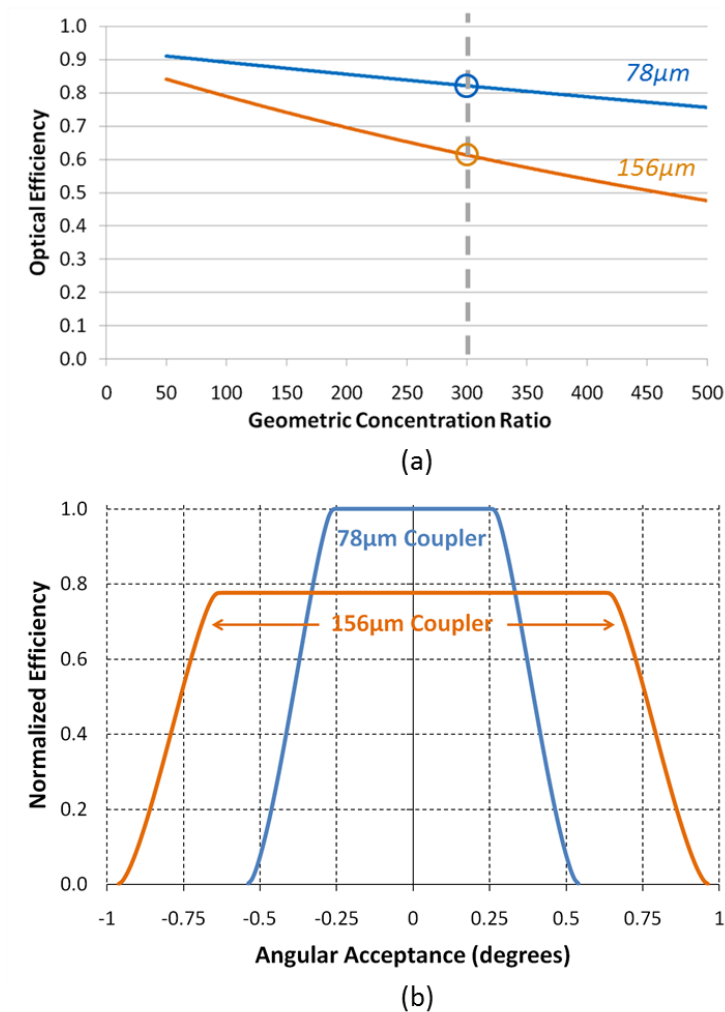


Figure 2.12 Increasing the coupling area adds angular acceptance at the cost of optical efficiency (a). At 300x, the efficiency drops by 22% (b).

2.6. Equivalent Designs

Altering the lens diameter or substrate thickness yields several equivalent systems with identical f-numbers. To reduce material quantities in air-clad designs, a portion of the lens array substrate can be replaced with a thicker air gap. Reducing the lens aperture while maintaining the same f-number shrinks the spot size, yet couplers occupy the same percentage of the total waveguide surface. As long alternate designs use the same f-numbers and waveguide thicknesses, systems yield identical path lengths to the output and therefore have the matching optical efficiencies.

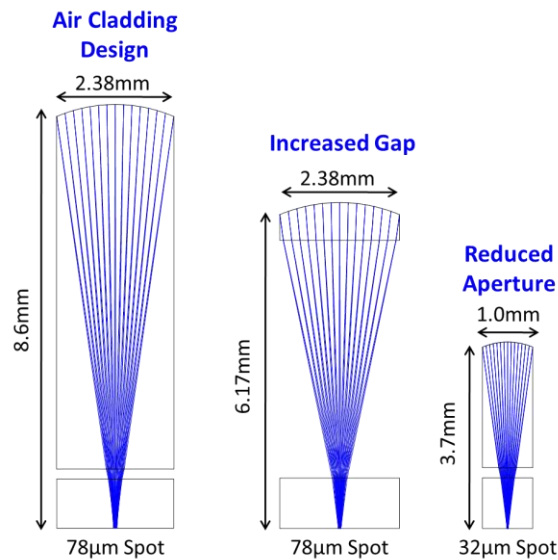


Figure 2.13 The cladding thickness or lens aperture can be altered for a given f-number and yield identical performance.

2.7. Summary

In this chapter, I introduced the concepts associated with micro-optic concentration and the relationship between lens array f-number, waveguide NA and

optical path length. 120° reflective prisms offered a unique coupler geometry which avoided shadowing effects from neighboring facets. Because the waveguide maintained a uniform cross-section, guided light could interact with subsequent prismatic regions and decouple as loss.

We developed an analytic model to understand the impact of propagation loss and determine general waveguide dimensions. From these calculations, two example designs were simulated in detail using Zemax nonsequential raytracing. Both systems approached 80% optical efficiency at 300x geometric concentration. Various waveguide geometries, coupling areas or lens parameters define an interesting new design space which can be tailored for high concentration, extended angular acceptance or aperture size.

Portions of Chapter 2 appear in J. H. Karp, E. J. Tremblay and J. E. Ford, “Planar micro-optic solar concentrator,” *Optics Express*, Vol. **18**, Issue 2, 1122-1133 (2010). The dissertation author was the primary researcher and author of this paper.

2.8. References

- [1] S. H. Cho, J. Godin, and Y. Lo, "Optofluidic Waveguides in Teflon AF-Coated PDMS Microfluidic Channels., "IEEE photonics technology letters : a publication of the IEEE Laser and Electro-optics Society **21**, 1057-1059 (2009).
- [2] Schott Inc.,
www.schott.com/advanced_optics/us/abbe_datasheets/datasheet_all_us.pdf.
- [3] A. Marcano O., C. Loper, and N. Melikechi, “High-sensitivity absorption measurement in water and glass samples using a mode-mismatched pump-probe thermal lens method,” *Appl. Phys. Lett.* **78**, 3415 (2001).

- [4] P. J. R. Laybourn, W. A. Gambling and D. T. Jones, "Measurement of attenuation in low-loss optical glass," *Optical and Quantum Electronics*, Vol. **3-3**, 137-144 (1971).
- [5] L. A. Pilkington, "Review Lecture. The Float Glass Process, "Proceedings of the Royal Society of London. Series A, Mathematical and Physical Sciences **314**, 1-25 CR - Copyright © 1969 The Royal Society.
- [6] G. Khanarian and H. Celanese, "Optical properties of cyclic olefin copolymers," *Opt. Eng.* **40**, 1024-1029 (2001).
- [7] J. G. Chang and Y. B. Fang, "Dot-pattern design of a light guide in an edge-lit backlight using a regional partition approach," *Opt. Eng.* **46**, 043002 (2007).
- [8] W. Van Sark, K. Barnham, L. Slooff, A. Chatten, A. Büchtemann, A. Meyer, S. Mc.Cormack, R. Koole, D. Farrell, R. Bose, E. Bende, A. Burgers, T. Budel, J. Quilitz, M. Kennedy, T. Meyer, S. Wadman, G. van Klink, G. van Koten, A. Meijerink, and D. Vanmaekelbergh, "Luminescent Solar Concentrators - A review of recent results," *Opt. Express* **16**, 21773-21792 (2008).
- [9] T. Tamir and S. T. Peng, "Analysis and design of grating couplers," *Appl. Phys. A.*, **14-3**, 235-254 (1977).
- [10] R. K. Kostuk and G. Rosenberg, "Analysis and design of holographic solar concentrators," *Proc. SPIE* **7043**, 70430I (2008).
- [11] P. Campbell and M. A. Green, "Light trapping properties of pyramidally textured surfaces," *J. Appl. Phys.*
- [12] A. Davis, "Raytrace assisted analytical formulation of Fresnel lens transmission efficiency," *Proc. SPIE* **7429**, 74290D (2009).
- [13] ASTM Standard G173-03e1, "Standard Tables for Reference Solar Spectral Irradiances: Direct Normal and Hemispherical on 37° Tilted Surface," *Ann. Book of ASTM Standards*, Philadelphia, PA, 2003, DOI: 10.1520/G0173-03E01, www.astm.org.
- [14] W. J. Cassarly, "Nonimaging optics: concentration and illumination," in *Handbook of Optics Vol. III*, M. Bass, J. M Enoch, E. W, Van Stryland and W. L. Wolfe (2nd ed. McGraw-Hill, 1995), Ch. 2.
- [15] S. O. Kasap, *Optoelectronics And Photonics: Principles And Practices* (Prentice Hall, 2001), p. 340.

Chapter 3

Self-Aligned Fabrication and Experimental Testing of Concentrator Prototypes

3.1. Self-Aligned Fabrication

Alignment between the lens array focus and coupling regions is critical for efficient waveguide coupling. Assembling separately fabricated components requires micron precision over large areas. Additionally, a pitch mismatch between the components causes alignment to occur only within limited regions. 120° coupling prisms enable an alternative self-alignment process which positions coupling regions during fabrication. The process begins by molding 120° prisms within a photosensitive polymer coated on the backside of the waveguide. The polymer is locally cross-linked with ultraviolet (UV) dosage through a permanently fixed lens

array. After exposure and application of a reflective coating, uncured portions of the polymer are removed while cross-linked regions remain part of the final device.

Self-alignment is extremely tolerant because the lens array focal plane is used as a lithography mask to define coupling regions. Coupler size, shape and position match exactly to the image formed by each particular lens aperture, despite lens imperfections or aberrations. This added tolerance enables concentrators to use inexpensive, embossed lens arrays instead of precision optics. In the following sections, I describe the key self-aligned processing steps, with the complete process included in Appendix B.

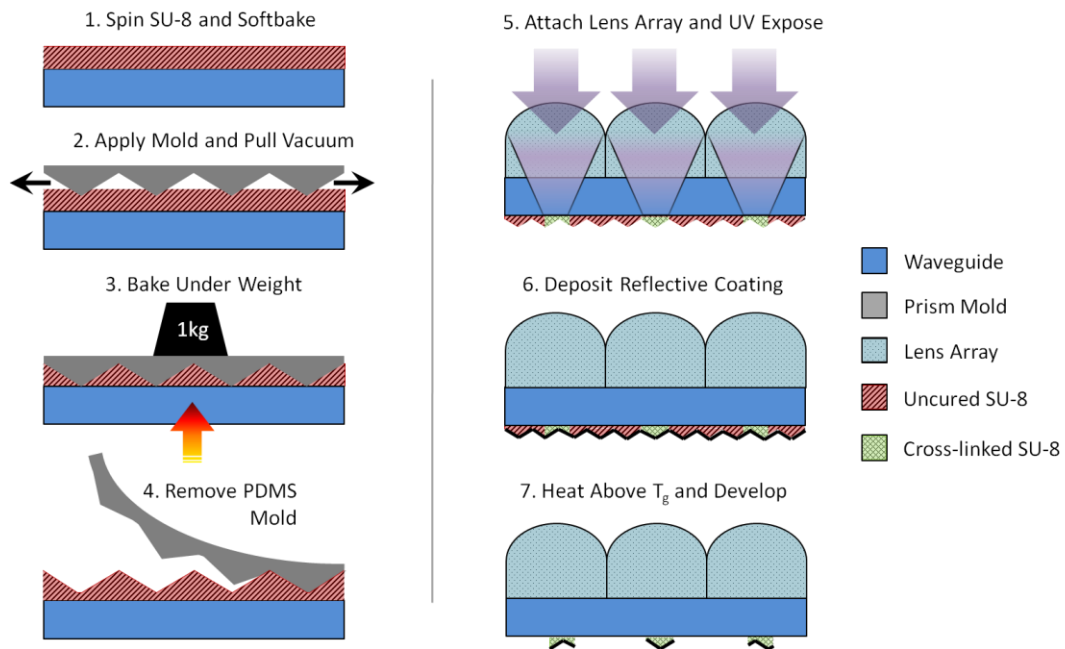


Figure 3.1 Self-alignment molds coupling regions within SU-8 photoresist. The lens array focal plane acts as the lithography mask during exposure.

3.1.1. SU-8 Photoresist Molding

Self-aligned fabrication starts by molding 120° prism couplers into SU-8 photoresist. SU-8 is a common, epoxy-based negative photoresist originally developed for microelectromechanical systems (MEMS) [1]. The resist can be spun to a wide variety of thicknesses and cross-linked with exposure to 365nm UV light [2]. Once processed, SU-8 demonstrates excellent mechanical robustness, chemical resistance and withstands temperatures above 200°C [3]. SU-8 is also highly transparent beyond 365nm and cures to a refractive index of 1.6, making it suitable as an optical coupling material [4].

SU-8 is formulated with a solvent (gamma butyrolactone) to maintain a liquid state for spin coating. After spinning onto a cleaned glass substrate, the resist was baked on a hotplate to remove the solvent, leaving behind a solid layer of a controlled thickness. Reheating the resist above the glass transition temperature (50°C) returns the film to pliable state which can be molded.

Wavefront Technology Inc. supplied 50µm pitch, 120° coupling prism material roll processed onto 200mm wide, 2m long sections of proprietary plastic film. SU-8 is not typically used as a molding polymer because trace amounts of solvent often remain within the prebaked layer. When pressed against a plastic mold, micron-sized bubbles rise to the surface and become trapped at the interface. Cannistra et. al. developed a SU-8 molding technique where a rigid master was cast into polydimethylsiloxane (PDMS) and used for molding [5]. PDMS is a widely available

silicon-based organic polymer which can be poured over three-dimensional structures such as 120° prisms and thermally cured to a flexible, reusable mold. Creating a negative imprint of the prisms in PDMS yields the identical profile because 120° prisms are symmetric. Processed PDMS remains permeable to most organic solvents, allowing gamma butyrolactone to diffuse into the mold and avoid bubble defects [6].

Once cured, the PDMS surface was silanated (United Chemical Technologies, Inc. (Tridecafluoro-1,1,2,2-Tetrahydrooctyl)-1-Trichlorosilane) to prevent bonding to the resist. The proposed molding technique placed the prepared PDMS mold over a softbaked SU-8 layer and applied pressure with a small, 1kg weight. The resist was then baked at 95°C for 45 minutes inside a low-vacuum oven which removed air trapped between the mold. Cannistra et. al. characterized the vacuum molding process and observed only minor SU-8 shrinkage ($<1\%$) and no impact on UV exposure dosage.

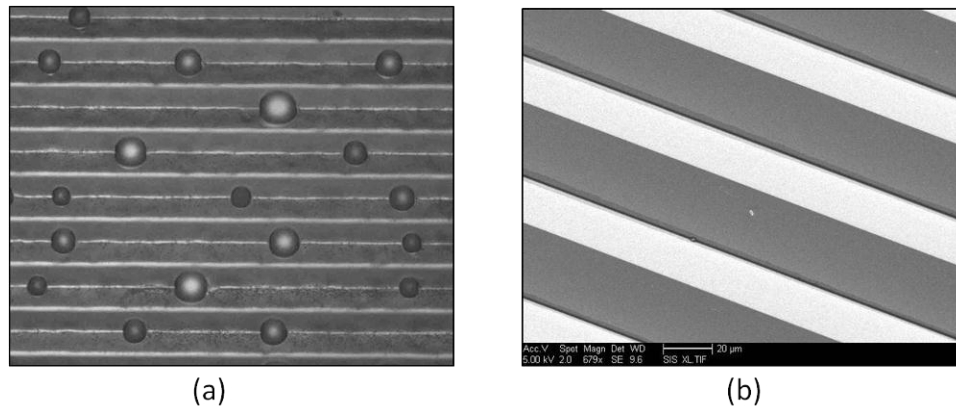


Figure 3.2 50 μm pitch 120° coupling prisms molded in SU-8 photoresist. Residual solvent becomes trapped beneath plastic molds (a) while PDMS molds allow the solvent to diffuse into the material for accurate replication (b).

3.1.2. UV Illumination

For self-alignment to correctly define coupling regions, UV illumination should mimic the angular extent of the sun. We constructed a custom UV illumination source using a mercury-arc lamp, filtered through a 4f relay system to accurately control divergence. We modified a lamp housing (Dymax 3010-EC) to gain direct access to the 100W mercury arc. An f/0.7 four-element condenser (Oriel Aspherab 66062) collected and roughly collimated the arc output. Light was reimaged with magnification using an f/2.5 plano-convex lens. We placed an adjustable iris at the image plane to control the spatial extent of the source. A 150mm diameter, f/2.4 parabolic mirror recollimated the filtered source resulting in large, uniform beam for exposure. We situated a 50/50 plate beamsplitter between the iris and collimating mirror to reflect light onto an assembly holding the lens array and waveguide. Changing the iris diameter at the mirror focus altered the degree of collimation.

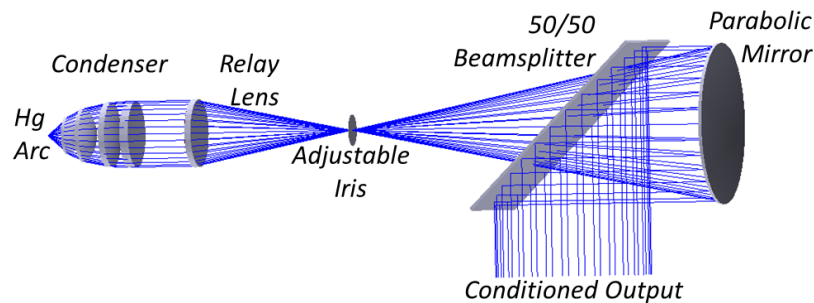


Figure 3.3 Optical layout of the UV illumination source with adjustable divergence.

We measured the source divergence using a diffraction-limited f/5 lens (Space Optics Research Labs) focused onto a scanning slit profiler (Photon Inc. XYGET

BeamScan). We initially set the divergence to $\pm 0.27^\circ$ (9.4mrad full angle). Subsequent iterations increased the divergence to create oversized coupling regions and increase angular acceptance. After conditioning, the 150mm diameter beam produced $240\mu\text{W}/\text{cm}^2$ of intensity with $\pm 12\%$ intensity variation. SU-8 required $300\text{mJ}/\text{cm}^2$ to fully cross-link, though incident UV light was focused by the lens array. Typical exposures were between 10 and 12 minutes. In addition to timed exposures, we positioned a calibrated photodetector within the unused arm of the beamsplitter to integrate exposed power.

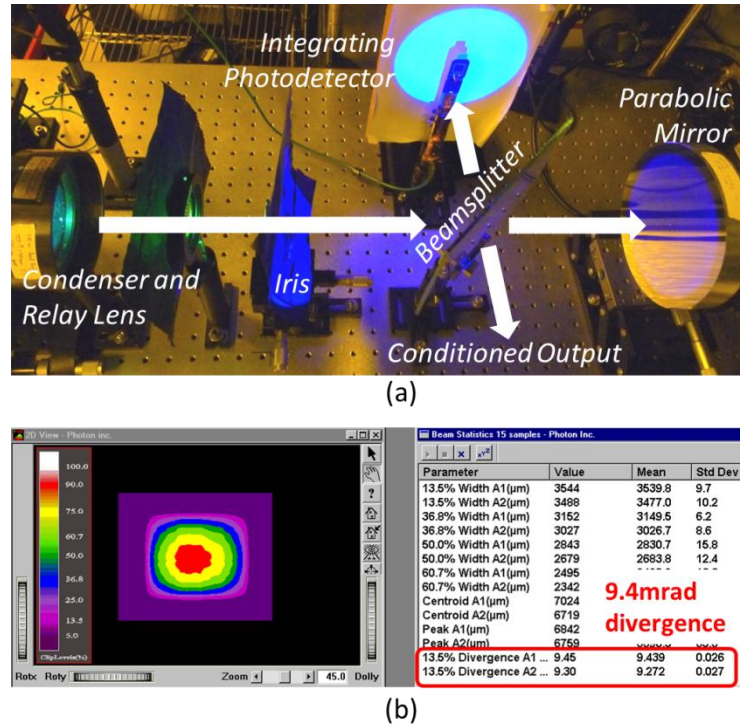


Figure 3.4 UV illumination system for self-aligned fabrication (a). Source divergence closely matched the extent of the sun (b).

3.1.3. Coupler Metallization and Development

120° prisms required a reflective coating to couple light into the waveguide. We needed to deposit a broadband reflector only on the prism facets and not planar waveguide sections to enable guided light to TIR. Prior to chemical development of SU-8, a 90nm aluminum coating was deposited over the entire layer using DC magnetron sputtering. Palik specified aluminum reflectivity at 92% and presented an inexpensive reflector for visible and infrared wavelengths [7].

The challenge was to remove uncured resist after sputter coating, while leaving cross-linked prisms as part of the final device. Standard SU-8 developer (propylene glycol monomethyl ether acetate, PGMEA) could chemically dissolve uncured regions due to the continuous aluminum coating. As a modification to the process, we heated the coated waveguide to 70°C, which exceed the glass transition temperature, to soften the underlying polymer. The resist was then developed in PGMEA in conjunction with ultrasonic agitation to pull the metallic coating away from the softened SU-8. With access to the resist, PGMEA could chemically developed uncured regions, leaving reflective cross-linked couplers attached to the waveguide surface. This process is akin to liftoff, except that later develops patterned resist prior to metallization. Proper liftoff completely strips the polymer from the surface instead of leaving select regions. Figure 3.5 shows cross-linked regions both before and after development.

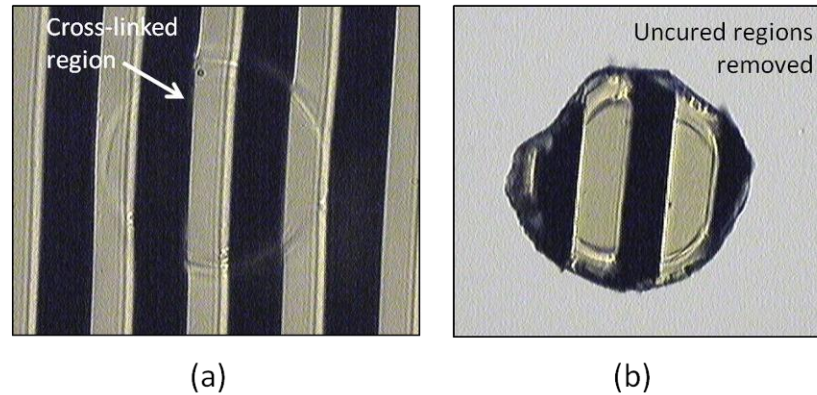


Figure 3.5 Prior to development, SU-8 is coated with an aluminum reflector (a). Using heat and ultrasonic agitation, uncured regions are removed, leaving behind cross-linked prism regions (b).

3.2. Experimental Designs

3.2.1. First-Generation System

3.2.1.1. f/1.1 Lens Array

Custom lens arrays made by diamond turning or reflow often carry high initial costs which were prohibitive in our small-scale demonstrations. Instead, experimental micro-optic concentrators were constrained to a few commercially-available lens and prism arrays. Our first experimental concentrator was based upon a 2.3mm diameter, f/1.1 plano-convex lens array (Fresnel Technologies Inc., part #300). These optics were not ideal due to lens aberrations, but were sufficient to demonstrate waveguide coupling with 120° prisms.

The low f-number produced steep marginal rays within the waveguide which required an air cladding to TIR. The extreme curvature of the lenses also led to gaps

between elements which reduced the overall fill-factor to 86.3%. Lens were embossed into a 2.23mm thick substrate of extended-range acrylic and supplied in 203mm x 254mm sheets. We used 75mm x 50mm, 1mm thick BK7 glass microscope slides as the waveguide. Wavefront Technology Inc. provided us with 50 μ m pitch 120° prisms embossed on proprietary plastic film. The assembled system yielded 37.5x geometric concentration.

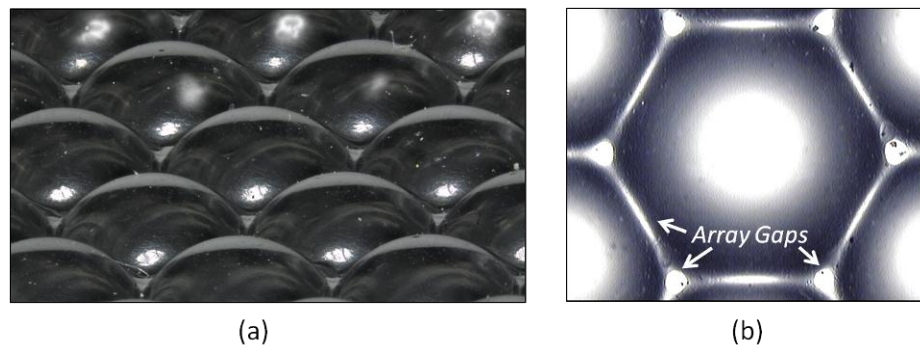


Figure 3.6 Image showing the sag of the f/1.1 plano-convex lens array (a). Gaps between lens elements reduced the array fill-factor (b).

3.2.1.2. Simulation

We simulated the performance of this experimental layout using Zemax nonsequential ray tracing. Simulations included the actual lens profile, AM1.5 illumination spectrum from 0.4-1.6 μ m, material absorption and dispersion. We assumed 92% coupler reflectivity and no antireflection coatings were applied to any optical surfaces. We adjusted the waveguide length to model optical efficiency as a function of concentration ratio.

Available $f/1.1$ lenses focused to $200\mu\text{m}$ spots on the back waveguide surface. Spherical aberration caused the coupler to occupy 1.6% of the total waveguide surface, significantly more than the 0.1% observed in optimized designs. At 37.5x, the simulated efficiency was only 44.8% with lens fill-factor and propagation losses accounting for the significant drop in expected performance.

3.2.2. Second-Generation Design

3.2.2.1. $f/3$ Lens Array

Second-generation concentrators were designed around 1.0mm pitch, $f/3$ lens arrays (Fresnel Technologies Inc., part #360). Increasing the f-number reduced aberration and surface sag, which eliminated gaps between apertures. The acrylic substrate thickness increased to 3.3mm and remained focused on the backside of identical 1mm-thick microscope slides. $60\mu\text{m}$ of air separated the lens substrate from the waveguide. Reducing the lens pitch increased the total number of coupling regions on the waveguide, though the size of each spot also decreased.

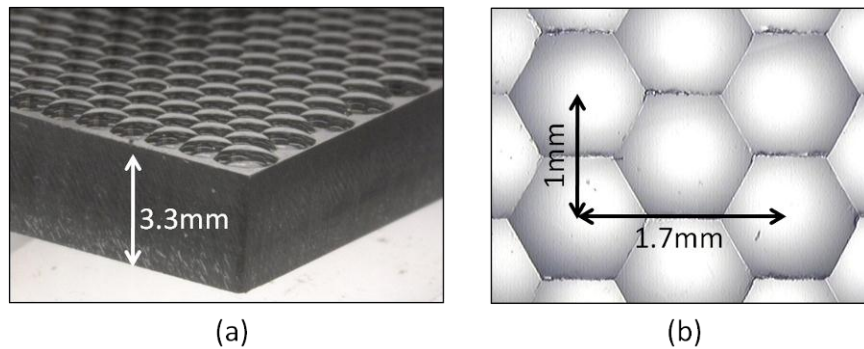


Figure 3.7 Second-generation plano-convex $f/3$ lenses (a). Reduced surface sag avoided gaps between hexagonally-packed elements (b).

3.2.2.2. Simulation and Comparison

Switching to $f/3$ lenses reduced spherical aberration, allowing these smaller optics to focus to $40\mu\text{m}$ coupling regions with $\pm 0.26^\circ$ field angles. On-axis, the lenses approach the diffraction limit, through axial color increased spot diameter at infrared wavelengths. Despite the increasing the total number of coupling regions, couplers accounted for only 0.16% of the waveguide surface, closely matching that of optimized systems. At 37.5x, the second-generation design reached 76.2% optical efficiency. The lack of antireflection coatings and reduced coating reflectivity prevented this configuration from matching the 91% simulated efficiency of the optimized air-clad system in Chapter 2.

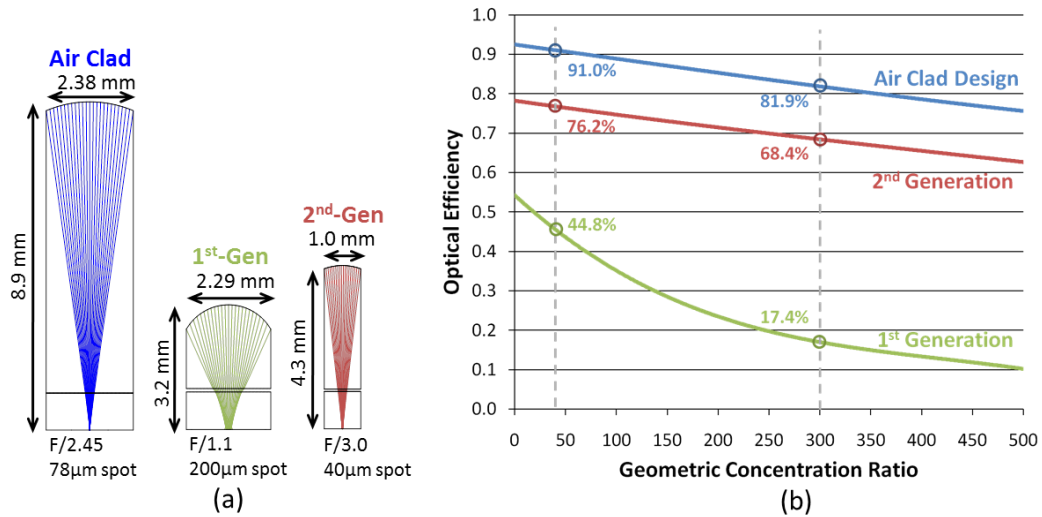


Figure 3.8 Layouts of the optimized air-clad design and the first- and second-generation prototype designs (a). Simulated efficiencies are traced as functions of concentration ratio (b). (© 2010 IEEE).

Even though $f/3$ lenses appeared to outperform $f/1.1$ optics in simulation, we pursued both optical designs. Available 120° prisms repeated a $50\mu\text{m}$ pattern.

Because couplers were fabricated on the outside of the waveguide, losses could occur near the edge of the molded coupler. Rays refracting through the coupler sidewall enter the waveguide at angles which no longer satisfy the TIR condition. Spreading light over several prism periods minimizes this coupling loss. $f/3$ lenses focused to $40\mu\text{m}$ coupling regions which encompassed less than one full prism period. $200\mu\text{m}$ coupling regions resulting from $f/1.1$ lenses included four prism periods and likely eliminate coupling edge losses. We fabricated systems using both lens arrays to determine which approach achieved best measured efficiency.

3.3. First-Generation Proof-of-Concept

3.3.1. Fabrication Results

We spun a $20\mu\text{m}$ thick layer of SU-8 photoresist onto a cleaned glass slide and embossed $50\mu\text{m}$ pitch prism facets using a PDMS mold. As expected, exposing through the $f/1.1$ lens array created $200\mu\text{m}$ diameter coupling regions on the backside of the waveguide. However, lens aberrations also produced $50\mu\text{m}$ annuluses of partially-cured photoresist around each cross-linked coupler. These uncoated regions increased the apparent size of the couplers to $300\mu\text{m}$ and impact propagation efficiency. Despite these imperfections, self-aligned fabrication consistently created accurate, reflective prisms on the waveguide surface.

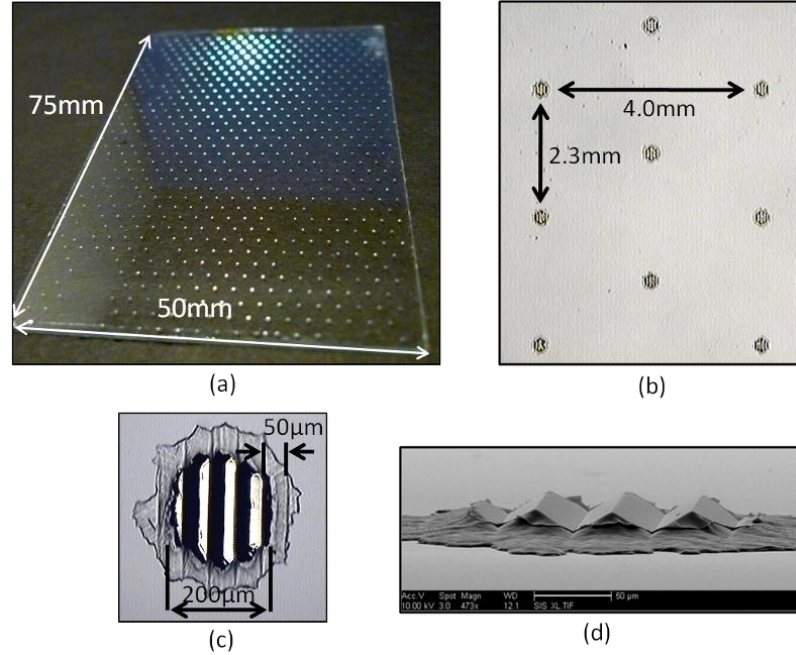


Figure 3.9 Patterened couplers on the waveguide surface using self-aligned fabrication (a). Couplers were spaced in a hexagonal array defined by the lens array (b). 120° prisms molded into SU-8. Lens aberrations increased the coupler size (c,d).

3.3.2. Optical Efficiency

After UV exposure, we separated the lens array and waveguide to simplify deposition and development processes. The two components were reassembled and mounted onto a translation stage for alignment and testing. Separation can be avoided if the lens array and waveguide remain fixed in position during fabrication and subsequent operation.

We illuminated the concentrator using a recollimated halogen lamp conditioned in a manner similar to the UV exposure system. We apertured the source to only illuminate the concentrator and accurately measure the total input power. With the lens focus aligned to the coupling prisms, we observed a bright strip of light

emitting from either edge of the waveguide. We experimentally measured 32.4% optical efficiency by index-matching a calibrated photodetector (Newport 818-ST) to the slab edge. The 10mm x 10mm photodiode underfilled the output edge and was moved to several locations to yield a more accurate result. An unsaturated image of the output reveals the mostly uniform intensity distribution, though some loss occurs towards the edges due to finite concentrator width and spatial variations of the source.

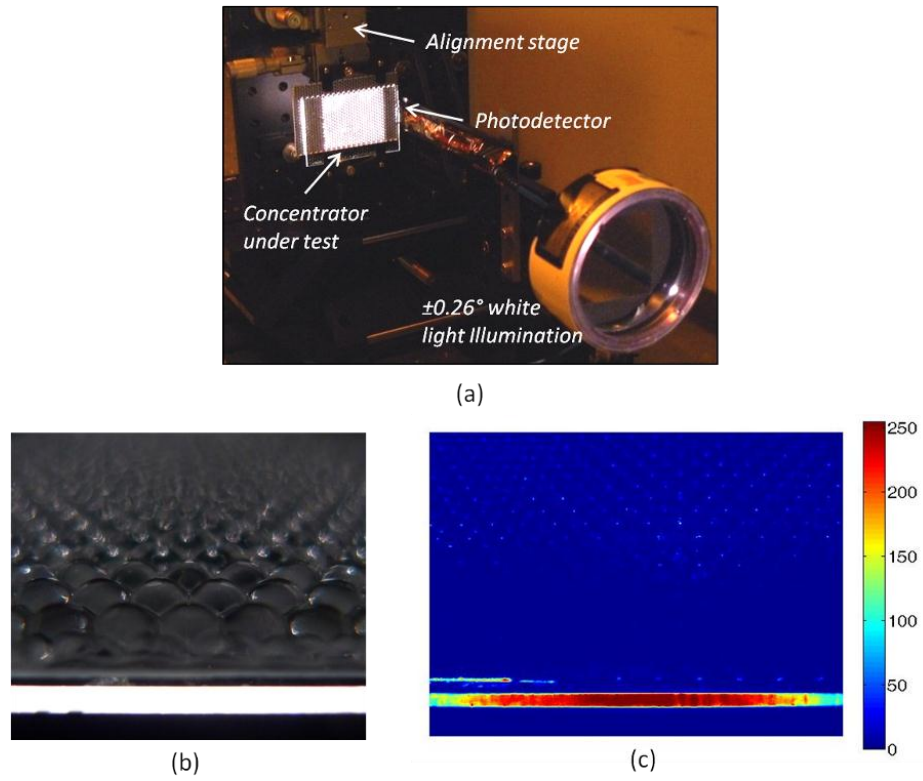


Figure 3.10 Fabricated first-generation concentrator under test (a). When aligned, coupled light appears as a bright line emitting from the edge (b). An unsaturated false color image shows intensity uniformity (c).

3.3.3. Angular Acceptance

Off-axis incidence laterally shifts the location of the lens focus. Small angles overlap portions of the focus with the coupler, capturing a fraction of the total energy. Large misalignments cause the image to completely miss associated coupling regions and pass directly through the system. The angular acceptance of the concentrator signifies the angle where 90% of the peak energy reaches the output.

To measure angular acceptance, either the concentrator or light source can be rotated to alter incidence angle. However, doing so restricts the aperture size by the cosine of the rotation angle. Instead of rotation, we measured the acceptance angle by translating the lens array with respect to the waveguide. Lateral shift can be related to angle using the lens focal length and Eq. 3.1. For the system under test, we observed $\pm 1.0^\circ$ angular acceptance with $37\mu\text{m}$ of translation. Translating by $200\mu\text{m}$ ($\pm 3.7^\circ$) caused almost no light to reach the output. We also tested the concentrator on sun to demonstrate waveguide coupling. In Figure 3.12, we can see coupled sunlight exiting the slab edge, though no data was taken under these conditions.

$$\theta = \tan^{-1} \left(\frac{\text{lateral shift}}{\text{focal length}} \right) \quad (3.1)$$

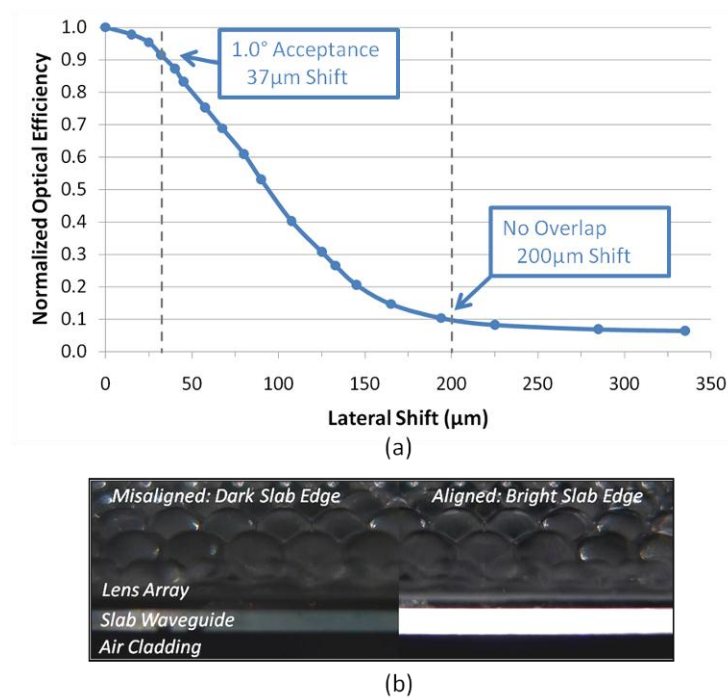


Figure 3.11 Angular acceptance measured through lateral translation (a). When aligned to the source with $\pm 1.0^\circ$ accuracy, light efficiently couples to the output (b).

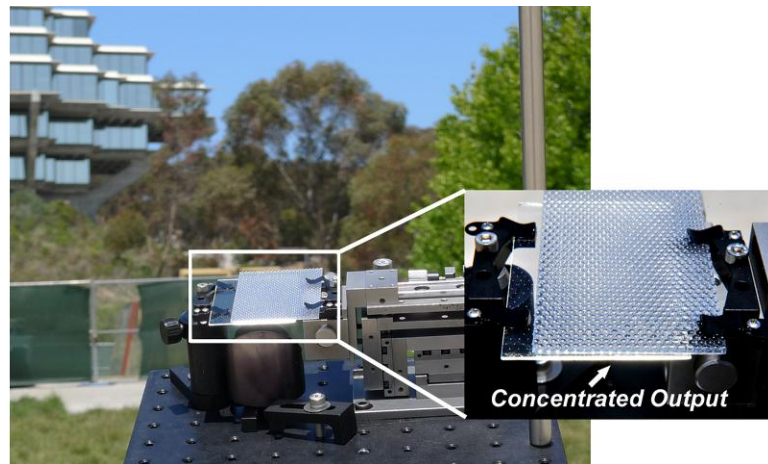


Figure 3.12 Outdoor demonstration using the first-generation proof-of-concept.

3.4. Second-Generation Prototype

3.4.1. Fabrication Results

We fabricated a second-generation experimental system using an $f/3$ lens array and the same molding and self-aligned exposure technique. Since the lens pitch shrunk to only 1mm, significantly more couplers appeared on the waveguide surface. Despite the increased density, the total covered surface area was almost ten times less than that of first-generation systems. Switching to higher f-number optics reduced spherical aberration previously seen with $f/1.1$ lenses. As a result, coupling regions are well-defined without the annulus of partially-cured resist.

As previously stated, the smallest coupling diameter contained less than one 120° prism period. We fabricated several iterations using various divergence parameters to yield coupling diameters ranging from 40-125 μm . We observed best results from systems using $\sim 80\mu\text{m}$ couplers. Oversized coupling regions were necessary to reduce edge coupling losses, though inherently effected propagation efficiency.

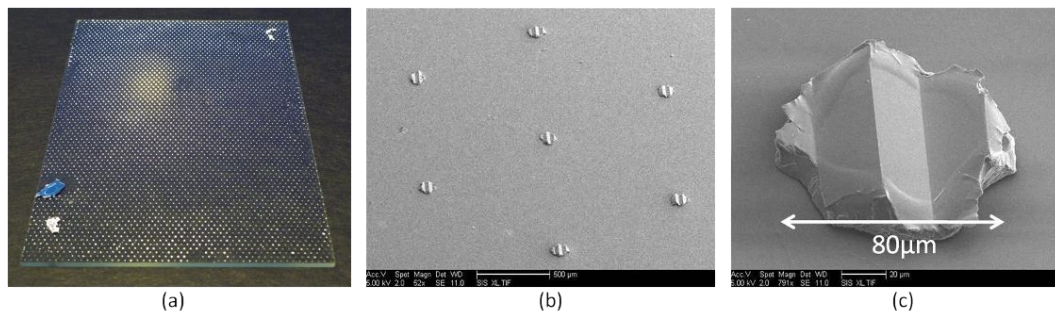


Figure 3.13 Thousands of coupling regions appear on the waveguide surface, yet occupy only a fraction of the total area (a). Molded and reflective 120° prism couplers match the hexagonal lens layout (b). Improved lens performance leads to well-defined couplers (c).

3.4.2. Efficiency Measurements

The device was tested in the laboratory using a 1000W Xe arc lamp collimated to $\pm 0.26^\circ$. This lamp was significantly brighter than the halogen source and better represented the spectrum of the sun. We again apertured the beam to illuminate only the concentrator area and measured 7.5W/m^2 of input power. We pursued two approaches to collect the 50mm x 1mm output of the waveguide. First, a 30mm x 3mm photodiode (Hamamatsu Photonics, S3588) was positioned to span exactly half of the exit aperture on one side of the waveguide. A high precision multimeter measured the photogenerated current. The diode geometry was well suited to the output dimensions and experimentally measured 52.3% optical efficiency with $\pm 0.38^\circ$ angular acceptance. A second efficiency measurement was taken using a 1cm^2 multijunction solar cell (Cyrium Technologies). The photovoltaic measured 51.26% efficiency, confirming the photodiode measurement. Spatial uniformity of the output appeared unchanged. These results show significant improvements over first-generation systems.

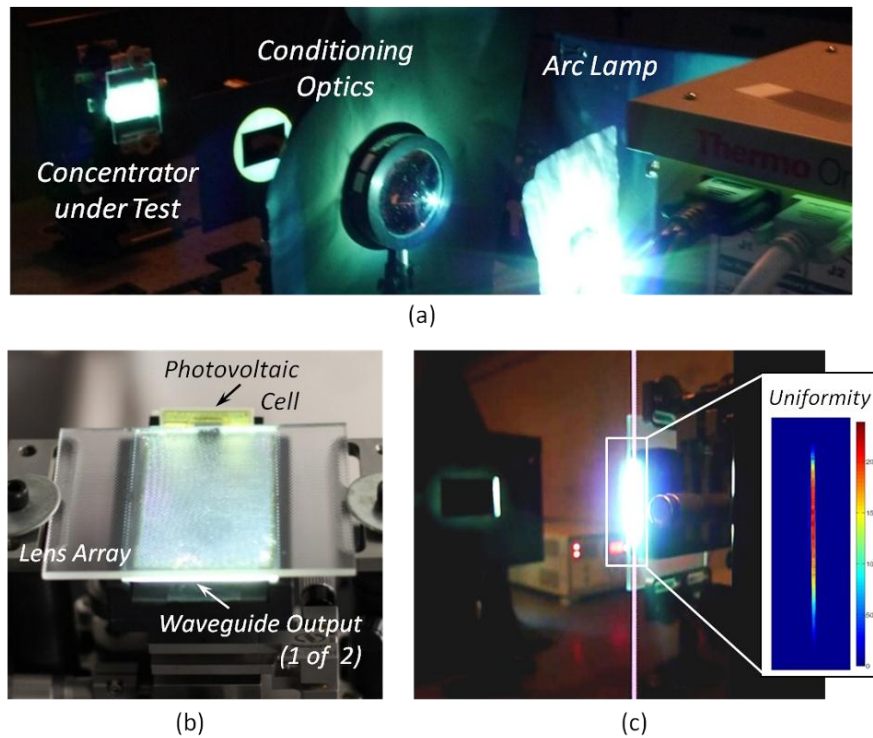


Figure 3.14 Second-generation concentrator under test (a). A multijunction solar cell measured output flux (b). Bright, uniform light exits the slab edge (c).

3.4.3. Spectral Performance

We tested the spectral transmission of the concentrator using an Ocean Optics USB2000 visible spectrometer. The grating and slit combination scanned from 343-786nm in 0.2nm increments. The measured input and output spectrums were very similar, despite an offset from different measured intensities. We did not identify any spectral selectivity or wavelength absorption within the waveguide. Figure 3.15 plots the normalized intensity as a function of wavelength, though certain spectral peaks saturated the spectrometer.

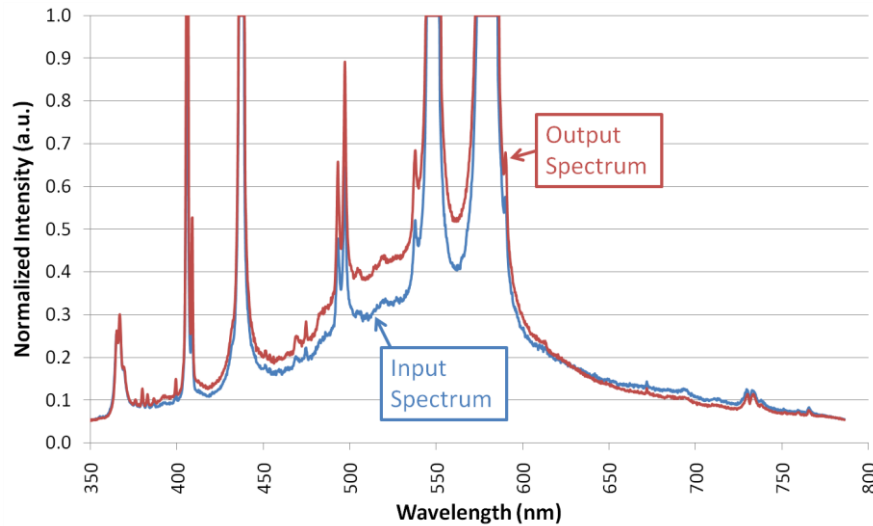


Figure 3.15 Measured input and output spectra of the concentrator.

3.5. Experimental Losses

3.5.1. Coating Reflectivity

Metallic coatings exhibit finite reflectivity as opposed to TIR reflections. To measure the actual reflectivity of the sputtered coating, we index-matched coated prisms to the hypotenuse of a right angle prism. The assembly was placed on top of a calibrated photodiode and illuminated with a HeNe laser. The measured intensity was compared to that occurring from a TIR reflection off the prism hypotenuse. Using this setup, we measured 85% coating reflectivity as opposed to 92% specified by Palik. The reflectivity difference accounted for a fixed reduction in optical efficiency at all concentrations. Suboptimal reflectivity can be improved by adjusting chamber conditions and deposition rates, but rigorous process development was beyond the

scope of this work [8]. Other broadband reflectors such as silver or dielectric mirrors can also increase reflectivity and maximize coupling efficiency.

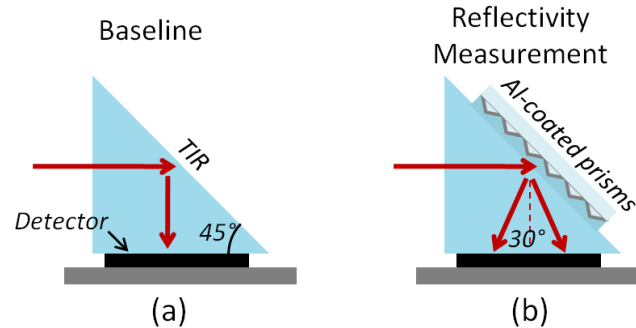


Figure 3.16 Aluminum reflectivity was measured by comparing reflection from a TIR (a) and coated prisms (b).

3.5.2. Edge Coupling Loss

Reflections near the coupler edge enable light to refract through the coupler sidewall and enter the waveguide at angles which do not TIR. This ray path exists because couplers are fabricated on the outside of the waveguide versus etched into the surface. The sidewall height projected onto the coupler area determines the edge loss percentage. Edge coupling losses become substantial when the prism pitch is comparable to the coupler diameter or the SU-8 thickness exceeds the prism height.

The $f/3$ lenses used in the second-generation prototype were capable of defining $40\mu\text{m}$ couplers, though edge coupling losses lowered measured efficiencies in these systems to below 25%. Expanding UV illumination divergence oversized coupling regions to include more than one prism period and lead to our best 52.3% measured efficiency. Due to the arc size and relay optics, the divergence could not be

further expanded without significantly increasing exposure times. Instead of increasing divergence, the correct solution reduces the prism period so sunlight strikes multiple facets. Roll-processing can easily define 120° prisms arrays with pitches below $5\mu\text{m}$, but thin SU-8 layers become more difficult to remove through ultrasonic development.

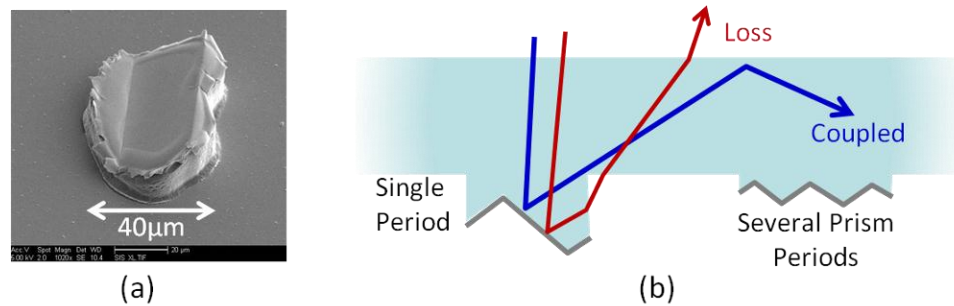


Figure 3.17 $f/3$ lenses could focus to $40\mu\text{m}$, but resulted in edge coupling losses (a). Reducing prism pitch minimizes such losses (b).

3.5.3. Revised Simulations

With a better understanding of experimental losses, we updated our initial Zemax simulations to include measured coating reflectivity and losses associated with the prism pitch. The second-generation concentrator design should be capable of 76.2% optical efficiency, yet this models a best-case scenario. Our first revision reduced mirror reflectivity to 85% and placed $50\mu\text{m}$ prisms within $80\mu\text{m}$ coupling regions. These changes significantly reduced the simulated efficiency to 62.4%. Reflectivity and coupler losses more closely modeled the system under test which was measured at 52.3%. Additional losses such as coating adhesion and TIR losses at the

waveguide sidewalls likely accounted for the remaining difference. If the prism pitch were reduced to $5\mu\text{m}$, simulations improved to 71.5%.

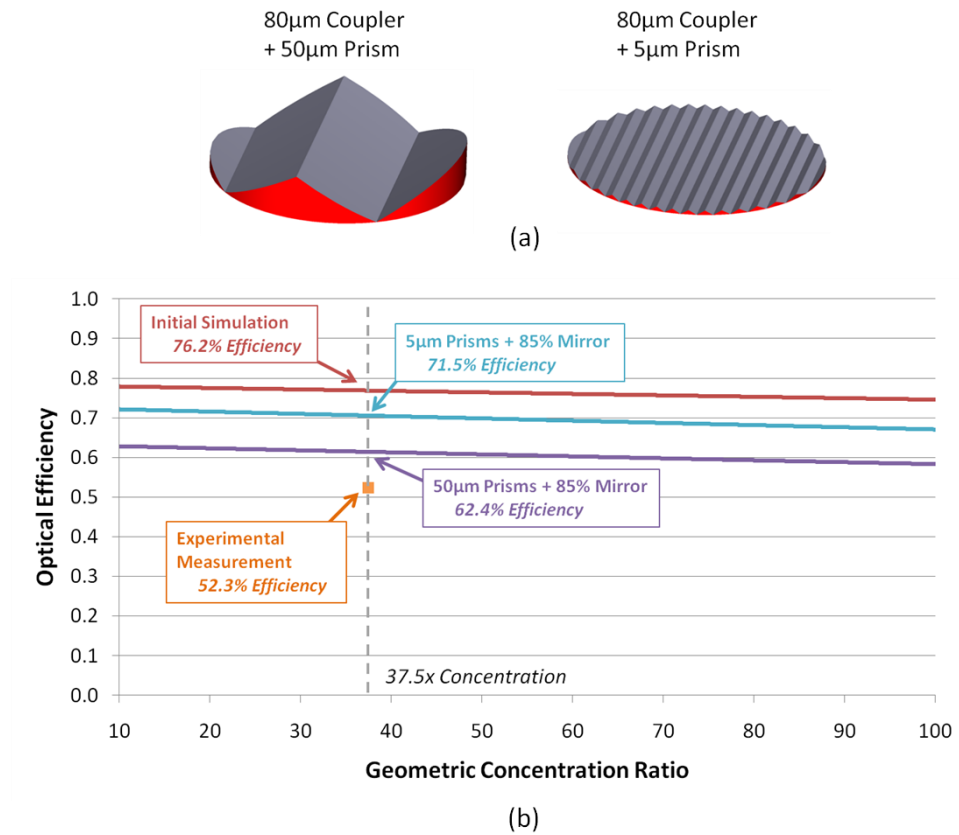


Figure 3.18 Prism pitches much smaller than the coupler reduce coupling losses, highlighted in red (a). Simulations were updated to include mirror reflectivity and coupling loss (b).

3.6. Summary

This chapter details the self-aligned fabrication process for molding, exposing, coating and developing prism couplers on the back waveguide surface. A custom UV illumination source matched the angular divergence of the sun and ensured proper sizing of coupling regions. Two experimental systems were fabricated using

commercially-available lens arrays. The first prototype suffered from lens aberrations which reduced the measured efficiency to 32.4%. A second-generation system used an improved lens array which increased the efficiency to 52.3%. We traced experimental losses to coating reflectivity and edge coupling losses. The small-scale prototypes demonstrated micro-optic concentration as well as highlighted other key design considerations for future systems.

Portions of Chapter 3 appear in 1) J. H. Karp, E. J. Tremblay and J. E. Ford, "Planar micro-optic concentration using multiple imaging lenses into a common slab waveguide," *Proc. SPIE* 7407, 74070D (2009), 2) J. H. Karp, E. J. Tremblay and J. E. Ford, "Planar micro-optic solar concentrator," *Optics Express*, Vol. **18**, Issue 2, 1122-1133 (2010) and 3) J. H. Karp, E. J. Tremblay and J. E. Ford, "Micro-optic solar concentration and next-generation prototypes," 35th IEEE Photovoltaic Specialists Conference (PVSC), vol., no., pp.000493-000497, 20-25 June 2010. The dissertation author was the primary researcher and author of these publications.

3.7. References

- [1] H. Lorenz, M. Despont, N. Fahrni, N. LaBianca, P. Renaud and P. Vettiger, "SU-8: a low-cost negative resist for MEMS," *J. Micromech. Microeng.*, Vol. **7**, 121-12 (1997).
- [2] MicroChem Corp., http://www.microchem.com/products/su_eight.htm.
- [3] H. Lorenz, M. Laudon, and P. Renaud, "Mechanical characterization of a new high-aspect-ratio near UV-photoresist," *Microelectronic Engineering* **41-42**, 371-374 (1998).

- [4] Hsieh, J., Weng, C.J., Tin, H.L., Lin, H.H. and Chou, H.Y., "Realization and characterization of SU-8 micro cylindrical lenses for in-plane micro optical systems," *Microsystem Technologies*, Vol. **11**, No. **4**, 429-437 (2005).
- [5] A. T. Cannistra and T. J. Suleski, "Characterization of hybrid molding and lithography for SU-8 micro-optical components, " *Journal of Micro/Nanolithography, MEMS and MOEMS* **9**, 013025 (2010).
- [6] T. C. Merkel, V. I. Bondar, K. Nagai, B. D. Freeman, and I. Pinnau, "Gas sorption, diffusion, and permeation in poly(dimethylsiloxane), " *Journal of Polymer Science Part B: Polymer Physics* **38**, 415-434 (2000).
- [7] E. D. Palik, *Handbook Of Optical Constants Of Solids*, Academic Press (1998).
- [8] S. Van Gils, T. Dimogerontakis, G. Buytaert, E. Stijns, H. Terryn, P. Skeldon, G. E. Thompson, and M. R. Alexander, "Optical properties of magnetron-sputtered and rolled aluminum," *Journal of Applied Physics* **98**, 083505 (2005).

Chapter 4

Increased Concentration Ratios using Orthogonal Waveguides and Secondary Optical Elements

4.1. Introduction

CPV systems often require greater than 500x solar concentration to maximize cell efficiency and reduce costly semiconductor materials [1]. In the context of micro-optic concentrators where the concentration ratio is proportional to waveguide length, very high flux levels require long propagation distances. Unfortunately, long optical paths lead to decreased optical efficiency due to subsequent interaction with downstream coupling regions. Alternatively, waveguide concentrators support complementary methods of increasing concentration beyond simple changes in optical

path length. Modifying the waveguide geometry to incorporate concentration along the slab width as well as incorporating secondary optical elements provides multiplicative concentration factors without impacting optical efficiency. Based on the concept of étendue, these methods decrease PV cell area by increasing the angular spectrum.

4.2. Concentration Limits

4.2.1. Angular Spectrum

Étendue is a fundamental property of all optical systems relating the concentration ratio to the angular field of view. Defined by Eq. 4.1, étendue states that the product of the entrance pupil diameter and source angle never increases [2]. In essence, to reduce the output aperture, the concentrator must increase the angles of rays leaving the system. We refer to the spread of ray directions as the angular spectrum.

$$a^2 \theta^2 = a'^2 \theta'^2 = \text{constant} \quad (4.1)$$

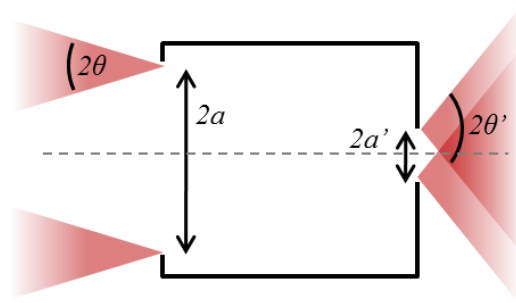


Figure 4.1 Generalized concentrator defining apertures and output angles.

In Chapter 1, I described how the second law of thermodynamics sets an upper concentration limit, occurring when the temperature at the output equals the surface temperature of the source. Rabl proved the concentration limit for point-focus concentrators, Eq. 4.2, where θ_{in} represents the source half angle and rays exiting the output span the entire $\pm 90^\circ$ angular spectrum [3]. Several optical geometries such as compound parabolic concentrators and nonimaging reflectors approach this limit, however, practical concerns such as track length, complex fabrication and thermal management hinder real-world applications [4][5].

$$C_{limit} = \frac{1}{\sin^2 \theta_{in}} \quad (4.2)$$

4.2.2. Micro-Optic Concentrator Output

The micro-optic solar concentrator relies upon a lens array coupling light into a planar waveguide. As configured, the lens array is the only element acting on incident solar angles and therefore accounts for all available concentration. Planar waveguides are inexpensive and can cover large areas, but are fundamentally unable to increase concentration due to their uniform cross-section. Though extending the waveguide length increases the geometric concentration ratio without bound, guiding losses prevent the output flux from exceeding the concentration observed between the lens aperture and focused spot.

120° prisms reflect converging light by 60°, after which rays begin to diverge as they propagate within the slab. Depending upon an odd or even number of total

reflections, light exiting the waveguide emits at $\pm 30^\circ$ with respect to the edge normal. Within each biased angle, we observe the angular extent imparted by the lens array f-number. Figure 4.2 traces the ray paths at the output and displays the angular spectrum on a polar plot for $f/3$ lenses exiting a BK7 glass waveguide. Exiting ray angles occupy only small percentage of the total angular spectrum. If the concentrator were thermodynamically limited, ray angles would completely fill the polar plot. From a fundamental perspective, we are able to confine coupled light to smaller output area.

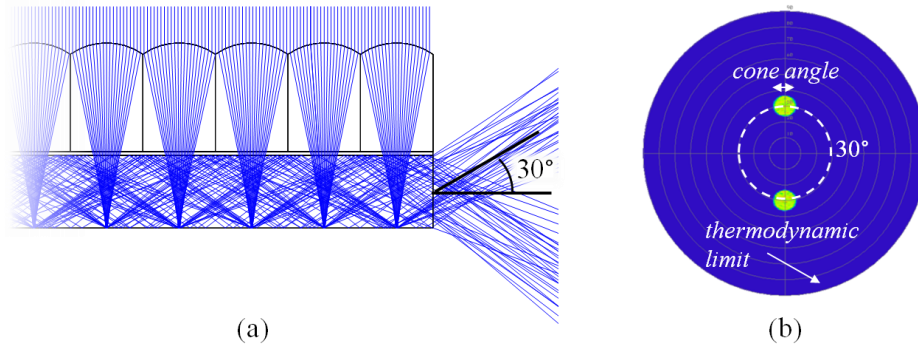


Figure 4.2 Light exiting the waveguide is biased at $\pm 30^\circ$ (a). Output angles span a small percentage of the available angular spectrum (b).

4.3. Orthogonal Waveguide Concentration

4.3.1. V-Trough Waveguide

For rectangular micro-optic collectors, the geometric concentration ratio is only of function of waveguide length and thickness. Altering the angle of slab sidewalls with respect to the waveguide axis restricts the output aperture in both width and thickness. The modified geometry allows the waveguide to act as a light cone, also known as a v-trough, to impart a degree of additional concentration along the slab

width. Light cones are one of the simplest nonimaging concentrators, but tend to turn back incident rays after multiple reflections [6]. Eq. 4.3 expresses the ratio of input to output apertures for orthogonal waveguide concentration, where l and h describe the slab length and thickness and w_1 and w_2 represent the wide and narrow widths of the waveguide, respectively.

$$C_{geo} = \frac{l \cdot (w_1 + w_2) / 2}{w_2 \cdot h} \quad (4.3)$$

In addition to the v-trough waveguide, coupling prisms can be oriented to preferentially reflect incident sunlight towards the output aperture. Rotating the coupling direction as a function of position causes the geometry to appear as a lens focusing to a common point. Rays coupled near the extreme edges experience the most tilt with respect to the waveguide axis. The slab aspect ratio and trough angle are free parameters which can be adjusted so on-axis marginal rays propagate parallel to the sidewalls. A mirror placed along the wider edge redirects light initially coupled away from the output back towards the narrow edge. Oriented couplers minimize the likelihood of ray rejection within the v-trough.

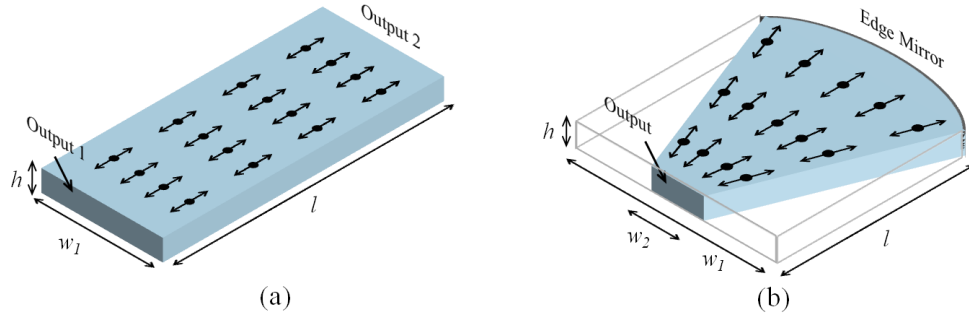


Figure 4.3 The concentration ratio for rectangular waveguides is only a function of length and thickness (a). Angling the sidewalls imparts additional concentration along the waveguide width (b).

4.3.2. Lens-Mirror Combination

We can draw a parallel between micro-optic concentration with oriented couplers and a simple lens focusing into a v-trough. Collares-Pereira et. al. previously analyzed this lens-mirror combination to demonstrate how the trough angle and lens focal length can be chosen to approach the thermodynamic limit [7]. The authors developed their geometry using the well-known edge-ray principle proposed by Welford and Winston [8]. Rays entering at the extreme edge of the aperture at the maximum acceptance angle are defined as edge-rays, and set the boundaries of the output. The edge-ray principle ensures any lesser ray position or angle also falls within these boundaries. An optical system is considered thermodynamically-limited when the edge-rays meet the extremes of the output and completely fill the angular spectrum.

For the lens-mirror combination, the lens focused into a v-trough whose trough angle sat parallel to the on-axis marginal ray. The lens f-number and v-trough aspect

ratio was chosen to intercept the edge ray at the boundary of the output and reflect at 90° . All other ray paths fall within this output area and experience at most one sidewall reflection. This geometry meets the criteria of the concentration limit by emitting over the entire angular spectrum, in one dimension.

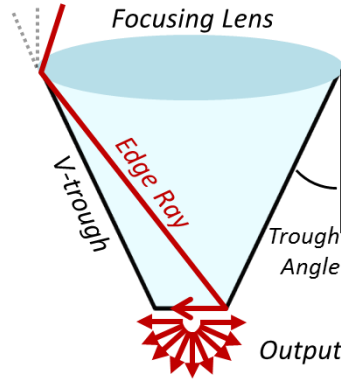


Figure 4.4 The lens-mirror combination proposed by Collares-Pereira et. al. The system is thermodynamically-limited when edge rays approach $\pm 90^\circ$ and define the output boundaries.

4.3.3. Orthogonal Waveguides at the Concentration Limit

The solar acceptance θ and the lens array f-number specify the required v-trough acceptance angle α , as noted in Eq. 4.4. Because the cone of light refracts into the waveguide, the v-trough acceptance angle decreases by a factor of n , the waveguide index. Collares-Pereira et. al. solved for the v-trough aspect ratio and trough angle which enabled the edge-ray to undergo a single reflection at the extreme of the output aperture. At the concentration limit C , the waveguide aspect ratio f/wl , length l , and trough angle ψ can be solved for using Eqs. 4.5, 4.6 and 4.7. These same equations can be applied to orthogonal waveguide designs.

The micro-optic concentrator must also incorporate a back reflector to capture light propagating away from the output. If the reflector is parabolic with focal length f , rays strike at near normal incidence and retroreflect back towards the output. This mirror provides the same angular distribution for the reflected path, making the v-trough geometry suitable for symmetric coupling.

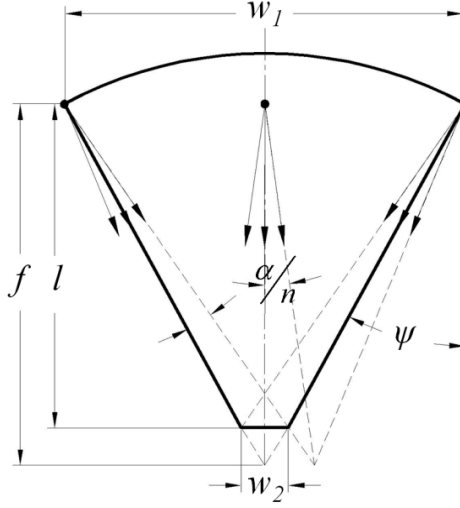


Figure 4.5 Geometry of the orthogonal waveguide concentrator, noting key dimensions including waveguide width, length and trough angle.

$$\tan \alpha = \frac{1}{2 \cdot F / \#} + \tan \theta \quad (4.4)$$

$$\frac{f}{w_1} = \frac{C+1}{2C^2} (3C^2 - 2C - 1)^{1/2} \quad \text{where} \quad C = \frac{w_1}{w_2} = \frac{1}{\sin(\alpha/n)} \quad (4.5)$$

$$\tan \psi = \frac{w_1}{2 \cdot f} \quad (4.6)$$

$$l = f \left(1 - \frac{1}{C} \right) \quad (4.7)$$

4.3.4. Simulation

We evaluated the orthogonal waveguide geometry at various lens array f-numbers collecting $\pm 0.26^\circ$ solar field angles. Figure 4.6 plots the maximum orthogonal concentration factor for aberration-free optics ranging from f/1 to f/10. The percentage of the waveguide surface occupied by couplers is also plotted on the same graph. Well-corrected f/1 lenses and couplers occupy less than 0.1% of the total waveguide surface, yet the associated 18.3° cone angle only supports 3x orthogonal concentration. With f/10 lenses, the orthogonal concentration factor approaches 30x, however, couplers occupy more of the waveguide surface area contribute to propagation loss. A certain degree of waveguide propagation is necessary as the slab length defines part of the collection area. Orthogonal concentration provides a multiplicative concentration factor and can be used as a free parameter to design systems with long waveguides or low f-number lenses.

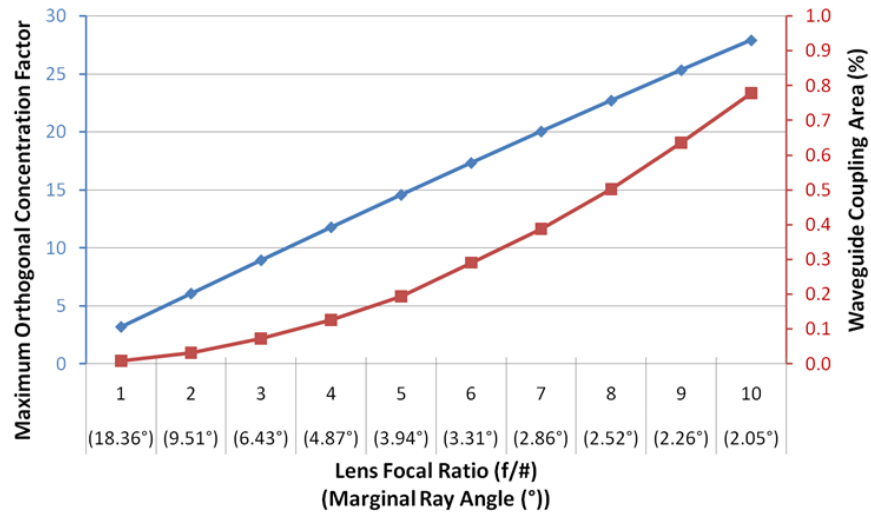


Figure 4.6 Lens array f-number limits maximum orthogonal concentration factor.

We modeled the performance of orthogonal waveguide concentration using Zemax non-sequential ray tracing. Simulations were based upon a 200mm long, 1mm thick BK7 glass slabs. Couplers and the edge mirrors were assumed to be 95% reflective. The lens array included a single layer MgF2 antireflection coating while the waveguide sidewalls remained uncoated. Figure 4.7 plots optical efficiency versus orthogonal concentration factor for several different lens array f-numbers. After passing the orthogonal concentration limit, extreme rays undergo multiple TIR reflections and begin to leak from the waveguide. For low-f-number lenses, this loss occurs rather quickly whereas the efficiency decrease is more gradual at higher f-numbers. However, high f-number designs began at lower initial efficiencies due to increased propagation loss within the 200mm long waveguide.

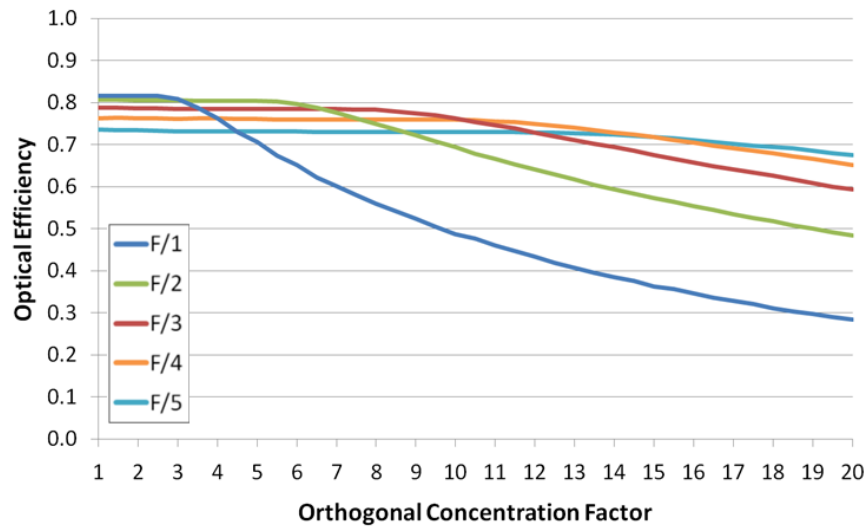


Figure 4.7 Systems lose efficiency beyond the maximum orthogonal concentration. All simulations included 200mm long by 1mm thick waveguides.

4.3.5. Sidewall Reflection

The original lens-mirror design relied upon reflective sidewalls to confine light along the width. In the revised micro-optic concentrator geometry, a glass waveguide supports TIR at these interfaces. From an overhead perspective, this claim seems inaccurate as marginal rays approach the sidewalls at angles much steeper than the critical angle between glass and air. However, light propagating within the waveguide actually strikes the sidewalls at skew angles due to coupling with 120° prisms. For common BK7 glass ($n_d=1.516$), the compound ray angle exceeds the critical angle and therefore reflects at the interface without additional coatings.

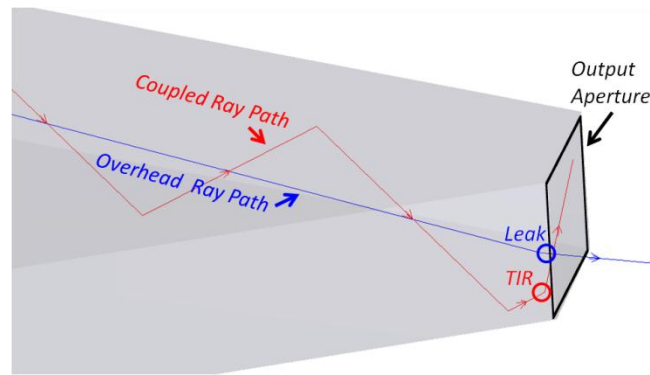


Figure 4.8 Propagating light strikes waveguide sidewalls at skew angles which undergo TIR.

4.3.6. f/3 System Example

To quantify the performance improvement, we compared orthogonal concentration to a rectangular layout using f/3 lenses. The lenses created $\pm 6.42^\circ$ field angles within the BK7 waveguide, setting an upper orthogonal concentration limit of 8.94x. Collares-Pereira et al. noted off-axis aberrations caused edge-rays to deviate from their ideal path and turn back after sidewall reflection instead of graze the output at $\pm 90^\circ$. The usable concentration factor for this design dropped to 8x in order to capture all coupled rays.

Figure 4.9 compares the optical efficiencies of orthogonal and rectangular waveguides as functions of geometric concentration ratios. Simulations began with 200mm long, 1mm thick waveguides. In the orthogonal case, we increased the concentration ratio by reducing the output width. The rectangular setup was extended in length to achieve higher concentration ratios. From Eqs. 4.5 and 4.7, the wide and narrow widths of the concentrator were calculated to be 245.7mm and 30.7mm respectively, yielding a 900x geometric concentration ratio. Orthogonal concentration

maintained 85% optical efficiency up to 900x, at which point light began to leak through the sidewalls, decreasing the optical efficiency. By contrast, the rectangular system used an 1800mm long waveguide to reach 900x. The optical efficiency dropped to 64.2% due to increased optical path and propagation loss.

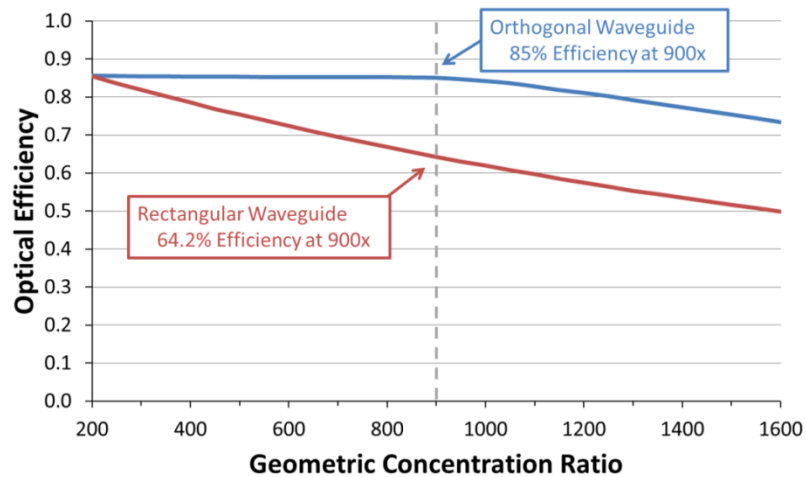


Figure 4.9 Orthogonal waveguide geometries increase the geometric concentration ratio without altering the optical path length or increasing propagation loss.

Orienting the waveguide coupling direction increases the angular spectrum of the propagating rays along the slab width. Figure 4.10 shows the final system geometry, including the parabolic edge reflector, represented as a Fresnel mirror. The polar plot shows the spread in angular spectrum which matches the increase in concentration ratio. Orthogonal concentration had no visible impact on the output uniformity and provided a useful means to increase concentration without altering the optical path length.

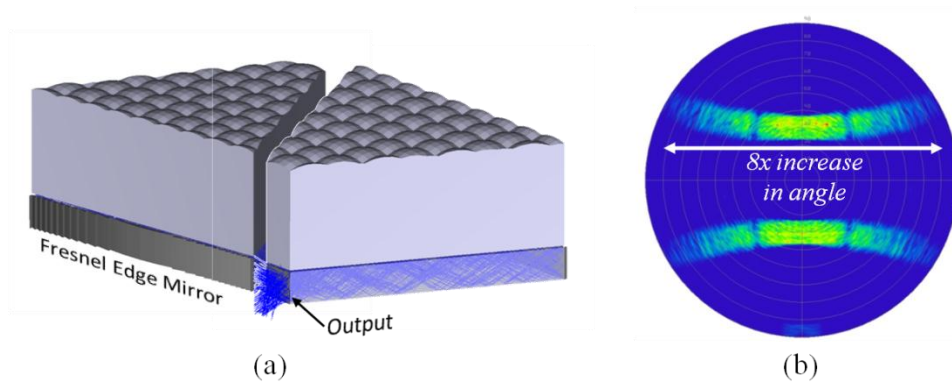


Figure 4.10 Layout of the 8x orthogonal waveguide concentrator (*note: system length was reduced for visualization purposes*) (a). Concentration along the width increases the angular spectrum in one dimension (b).

4.4. Secondary Optical Element

4.4.1. Design

CPV systems often incorporate secondary optical elements (SOEs) such as kaleidoscopes or compound parabolic concentrators which capture converging sunlight prior to reaching the PV cell [9]. These nonimaging optics homogenize the output intensity as well as provide additional concentration. Using étendue and the edge-ray principle, we designed a unique SOE which mates to the waveguide output and further increases the concentration ratio.

The proposed optic was situated between two opposing waveguides and directed counter-propagating light to a common output. Light approaching the slab edge experienced either an odd or even number of TIR reflections, producing two distinct ray bundles, biased at $\pm 30^\circ$ with respect to the waveguide axis. The SOE in Figure 4.11 used planar bottom surfaces to reflect downward rays, depicted in green,

back upwards and parallel to upward-emitting rays. Rays traced in blue travelled at $+30^\circ$ and missed the bottom surface. Both ray paths were incident on a parabolic mirror and focused onto a PV cell situated beneath the SOE. The mirror axis was centered atop the opposing waveguide and tilted by 30° to minimize focal length. The symmetric SOE used a second reflector to collect light emerging from the other waveguide and focused to the same output.

A second nonimaging optical path existed for light undergoing an odd number of TIR reflections. Downward propagating light was able to strike the PV cell directly, without reflecting off the planar SOE surface or parabolic mirror. This ray path is analogous to light traveling down the center of a kaleidoscope, avoiding interaction with the sidewalls.

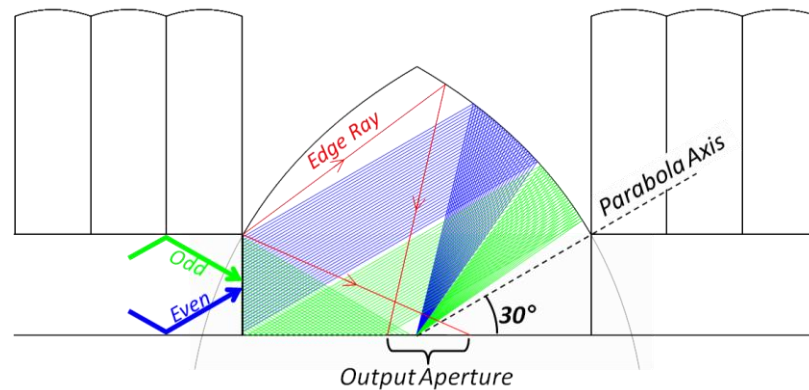


Figure 4.11 The SOE was situated between two opposing waveguides and focused to a common output. A nonimaging path allowed downward rays to strike the PV cell directly.

Edge rays, highlighted in red, identify the most extreme upward and downward light paths and mark the boundaries of the output. The f-number of the lens array

defined the marginal ray angles and limited the amount of secondary concentration. Diverging rays appeared as field angles at the parabolic mirror and focused to off-axis locations within the edge-ray boundaries. The SOE can be considered a variation of the compound parabolic concentrator, however, opposing entrance apertures prohibited light from exiting at $\pm 90^\circ$.

4.4.2. Simulated Performance

Again using Zemax nonsequential ray tracing, we simulated a SOE collecting light from micro-optic concentrators with $f/3$ lens arrays. First, we added aspheric surface coefficients to the parabolic reflector as a way to balance off-axis mirror aberrations. After optimization, the SOE focused to an output aperture 3.3x smaller than the combined waveguide edges. >99% of rays reached the output. The optical efficiency of the SOE depends on coating reflectivity, with metallic reflectors being >90% and dielectric stacks approaching 99% reflectivity. In terms of angular spectrum, exiting rays spanned $\pm 12^\circ$ to $\pm 65^\circ$ while maintaining excellent intensity uniformity. In this example, SOE concentration was limited by marginal ray angles associated with $f/3$ lenses. Higher f-numbers yield similar optics but enable increased levels of concentration.

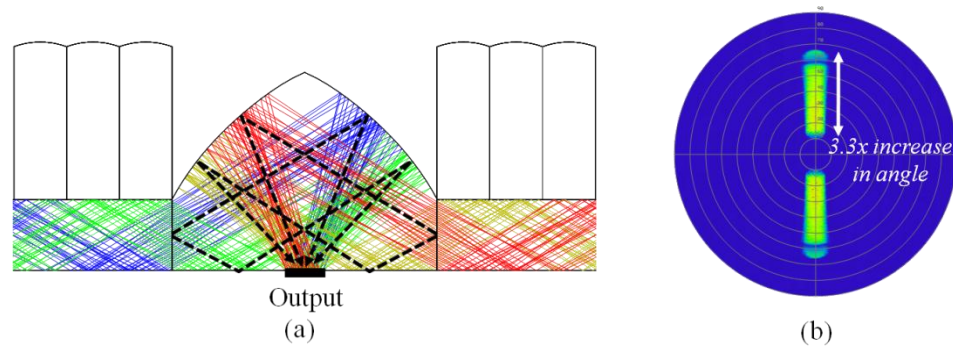


Figure 4.12 The SOE designed for f/3 micro-optics with each ray path highlighted (a). The angular spectrum increased by 3.3x in one dimension (b). (© 2010 IEEE).

The proposed SOE design has the added benefit of repositioning the PV cell beneath the waveguide instead of mounting vertically to the waveguide edge. Placing the cell underneath provides ample space for the cell carrier, heatsink and interconnects. We envision an optic fabricated by glass or injection molding and affixed to the PV cell prior to connecting to the waveguide outputs. An alternative embodiment integrates the SOE as an element within lens array and placed on top of the waveguide. In this case, cladding regions must be selectively removed for the SOE to act on otherwise guided light.

4.5. High-Concentration System Designs

4.5.1. Improved Efficiency

The waveguide SOE can be used to shorten propagation distances and improve overall efficiency. Consider the optimized air-clad design described in Chapter 2 with 81.9% simulated efficiency at 300x concentration. The SOE can be incorporated into this system to push towards 1000x, or the waveguide can be shortened to reduce

propagation loss. Instead of a single, long, 300x concentrating waveguide, the SOE can be placed between two 91x systems which operate at 89.3% efficiency. If the SOE used 98% reflective silver mirrors, the overall configuration reaches 87.5% efficiency compared to 81.9% of the simple, rectangular layout.

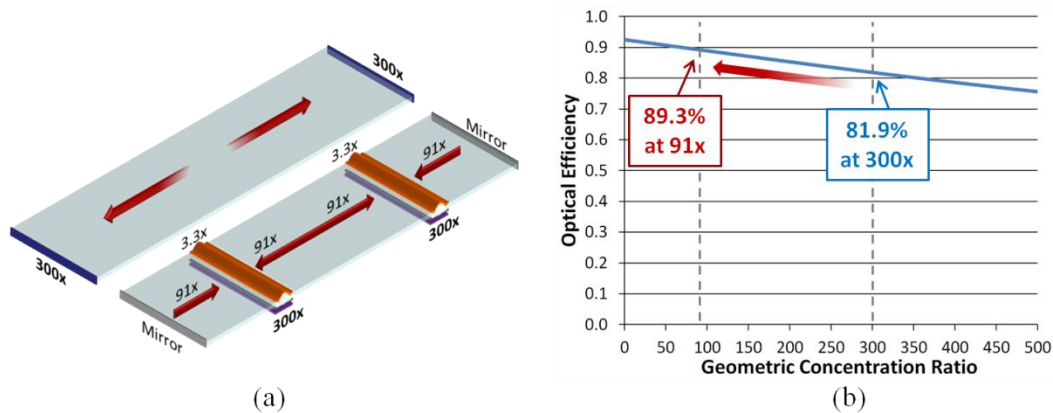


Figure 4.13 The SOE can improve efficiency by shortening the waveguide length while maintaining concentration (a). Optical efficiency improved from 81.9% to 87.5% at 300x.

4.5.2. Spectral Separation

High-efficiency solar cells use multiple, current-matched layers to respond to the entire solar spectrum. Additional material bandgaps improve efficiency, but lattice mismatches and defects complicate fabrication [10]. Instead, dichroic mirrors can be used to optically split the incident spectrum and direct energy onto separate PV cells optimized for each spectral band. Optical geometries based on cube beamsplitters have previously demonstrated spectral separation, but tend to orient PV cells orthogonal to one another which complicate packaging and alignment [11]. With micro-optic concentration, spectral separation into two bands is easily performed by placing dichroic mirrors over each waveguide output. Light interacting with the

mirror either emits out the edge or passes back through the system and exits through the opposing output. Coatings may be applied directly to the slab edges or integrated as part of the PV cell. Due to symmetry, spectral splitting also functions with waveguide SOEs.

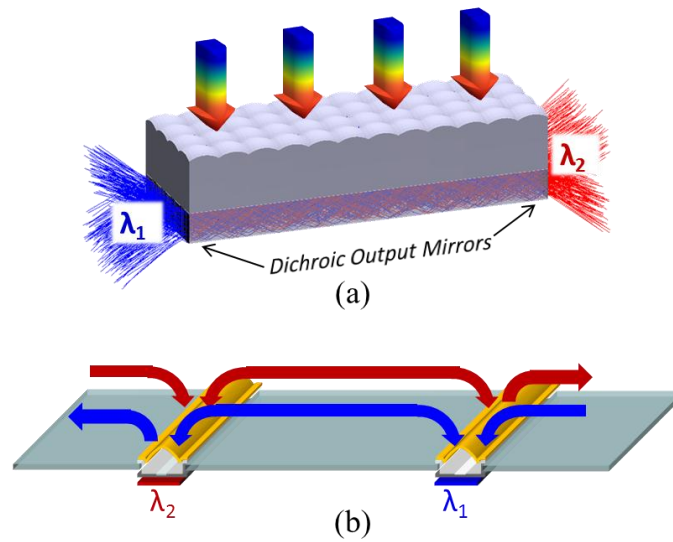


Figure 4.14 Spectral splitting with dichroic mirrors placed along the slab edges (a) or integrated into the SOEs (b).

4.5.3. Combining Orthogonal and SOE Concentration

Orthogonal waveguides and secondary optics both achieve concentration by increasing the angular spectrum at the output. However, each approach acted on the coupled rays in perpendicular directions, meaning both methods can be combined into the same system. The resulting configuration positions two orthogonal waveguides to form a ‘bowtie’, joined by a SOE in the center. We previously simulated a 900x orthogonal concentrator with 85% optical efficiency. Pairing this geometry with a 3.3x SOE yields 2970x geometric concentration with greater than 83% optical

efficiency. For the geometry to maintain high efficiency, the SOE sidewalls must become optical surfaces in order to confine skew rays exiting the orthogonal waveguide. In Figure 4.15, we see visually depict the bowtie configuration and the associated angular spectrum. From both concentration methods, the angular spectrum expands by 26.4x compared to rectangular micro-optic concentrators with $f/3$ lenses.

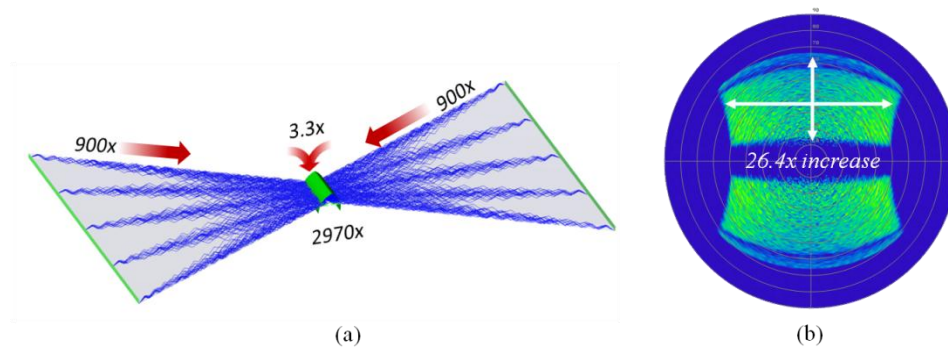


Figure 4.15 Both orthogonal concentration and waveguide SOEs can be combined into a single system (a). The overall angular spectrum increased 26.4x compared to rectangular waveguides (b).

As described, the bowtie concentrator no longer complies with roll-to-roll manufacturing because the system contains many individual components which must be assembled and aligned to one another. Interestingly, components such as v-trough sidewalls and back reflectors can be replaced with equivalent micro-optic structures integrated into the lens array surface and index-matched to the waveguide. Displacing edge-mounted components to the top surface returns to a single micro-optic superstrate which can again be manufactured and applied to large-area planar waveguides. However, designing such prismatic reflectors can be difficult as shadowing effects can limit accepted angles.

Very high concentration ratios ($>1000\times$) give rise to practical problems such as tracking alignment and thermal management. Instead of maximizing concentration ratio, the bowtie concentrator can be redesigned to operate at a lower flux level in exchange for increased acceptance angle or alignment tolerance. Choices between lens f-number, coupling area, waveguide length, trough angle and secondary optics provide immense design flexibility within planar concentrating optics.

4.6. Orthogonal Waveguide Prototype

4.6.1. Sectioned Waveguide

To demonstrate orthogonal waveguide concentration, we diced a 75mm x 50mm x 1mm thick glass slab to create an 11.3° trough angle and a 20mm x 1mm output aperture. To approximate radial coupler orientation with a linear prism array, three wedged sections were assembled into a single PDMS mold. A first-surface edge mirror attached directly to the wide edge of the waveguide. Instead of a custom parabolic edge reflector, we used a planar aluminum mirror index-matched to the wide face of the slab. We chose a narrow trough angle far from the thermodynamic limit to support the suboptimal reflector shape.

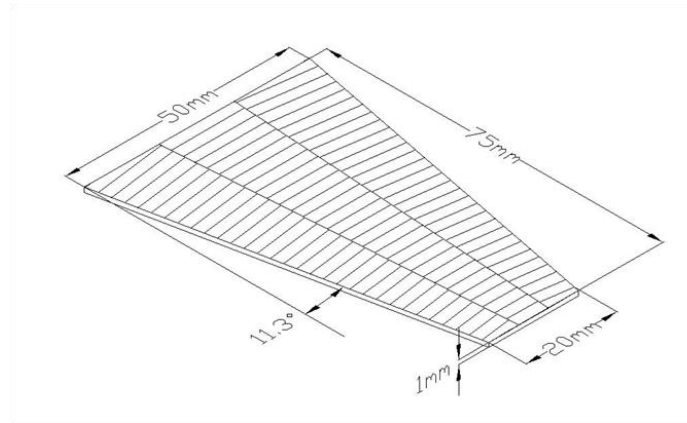


Figure 4.16 Layout of the orthogonal waveguide prototype with assembled linear prism arrays.

4.6.2. Experimental Results

The experimental geometry was first programmed into Zemax to trace the optical efficiency. Simulations included 1mm diameter, $f/3$ lenses focusing onto sectioned and oriented 120° prisms. Each coupling region was $80\mu\text{m}$ in diameter and intersected $50\mu\text{m}$ prism periods. We assumed the planar edge mirror was 85% reflective due to our previous coating measurements. The geometry provided 131x geometric concentration with 59.4% optical efficiency. The efficiency can be improved by reducing the prism pitch to $5\mu\text{m}$ and increasing reflectivity. Simulated performance is slightly lower than comparable rectangular waveguides due to an extra reflection off the back edge mirror.

Orthogonal waveguide concentration relies upon optical-quality sidewalls to further confine guided light. Dicing the waveguide left diffuse edges which caused light to scatter upon incidence. Precision edge polishing on 1mm thick substrates is both difficult and expensive because traditional lapping tends to round the edges. As a

polishing alternative, we refaceted the sidewalls by adding a thin layer of PDMS to index-match out surface irregularities. PDMS was prepared with 70% toluene to reduce viscosity and spun onto a glass wafer at 500rpm. The diced edge was then dipped into the PDMS layer and cured against a silanated glass flat. Figure 4.17 shows the resulting specular sidewalls. As consequence of refaceting, PDMS also covered a small portion of the top and bottom waveguide surfaces and strip incident light. We observed $\sim 100\mu\text{m}$ of PDMS on these critical surfaces. Adding material instead of polishing provides a fast, simple approach to test systems, but should not be considered a permanent solution.

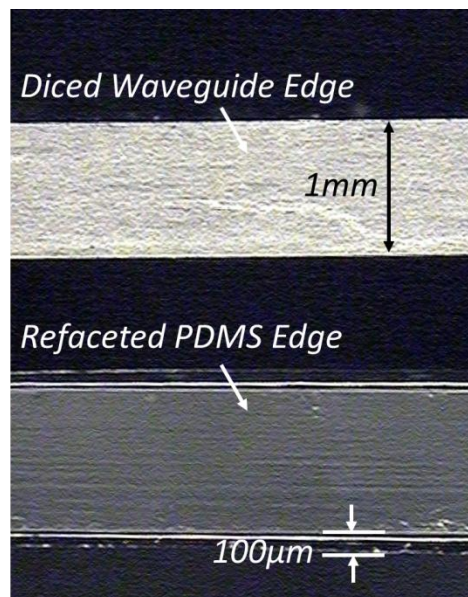


Figure 4.17 Dicing the waveguide left diffuse sidewalls. Refaceting edges with PDMS index-matched out surface irregularities to yield specular sidewalls.

Figure 4.18 shows the orthogonal waveguide concentrator fabricated using the same self-alignment procedure outlined in Chapter 3. We measured the optical efficiency using a Xe arc lamp conditioned to match the divergence of the sun. A

30mm x 3mm photodiode (Hamamatsu Photonics Inc., S3588) spanned the entire 20mm x 1mm output and captured all the light emitting from the edge. We experimentally measured 22.4% optical efficiency at 131x geometric concentration.

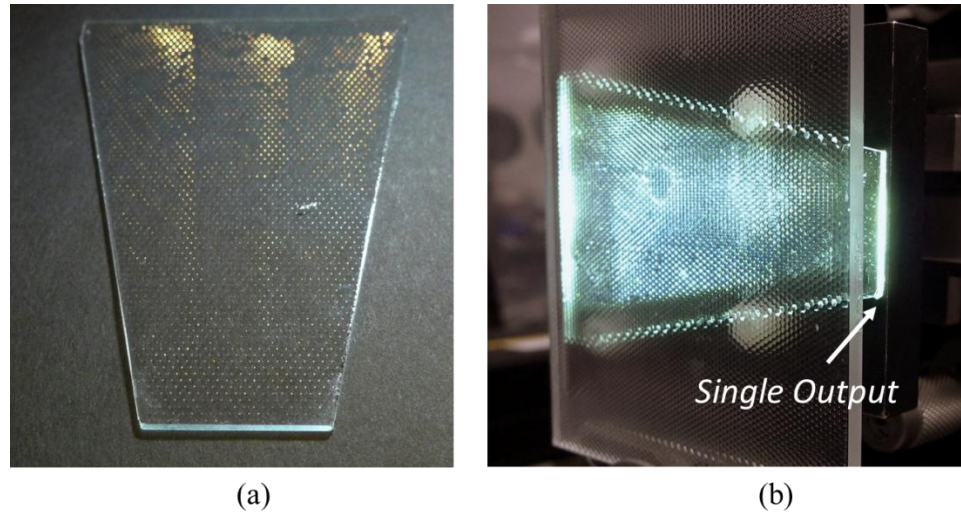


Figure 4.18 Fabricated orthogonal waveguide concentrator (a). Experimental system under test (b).

The measured efficiency is significantly lower than we expected. We attribute the lower performance to several new loss mechanisms unique to the orthogonal concentration setup. Though the sidewalls were specular after refaceting, point defects and chips in the glass lead to light leakage. Refaceting also left excess material along the waveguide edges. 100 μ m of PDMS on the top and bottom surfaces reduced the optical efficiency by more than 10%. Similar losses occurred when index-matching the planar edge reflector. Index gel tended to overflow onto the waveguide surfaces when positioning the mirror. Due to additional confinement along the slab

width, guided light had a high probability of interacting with any one of these edge loss mechanisms and leaking from the slab.

From our simulations, orthogonal concentration presents a powerful method for increasing concentration ratios without affecting optical path length. However, we must address several practical concerns in order to achieve this benefit. Altering the waveguide geometry places particular emphasis on surface quality and assembly which can complicate manufacturing.

4.7. Summary

Micro-optic concentrators experience loss due to propagation within a lossy waveguide. Altering the waveguide geometry increases the concentration ratio by confining light along the slab width. Selecting the proper waveguide aspect ratio enables these systems to approach the thermodynamic concentration limit in one dimension. A secondary optic combines the outputs of two waveguides to also increase concentration. Lens array f-number determines guided ray angles and influences the amount of additional concentration available within the angular spectrum. Both orthogonal waveguiding and secondary focusing can be combined together to increase the base concentration level by more than 25x. However, fabricating these modified structures deviates from the initial roll-to-roll processing concept and requires precision surfaces and assembly. Depending on application, orthogonal waveguiding and/or secondary optics provide additional degrees of design

freedom which can lead to increased efficiency, higher output flux or relaxed solar alignment.

Chapter 4, in part is a reprint of material appearing in 1) J. H. Karp, E. J. Tremblay and J. E. Ford, "Micro-optic solar concentration and next-generation prototypes," 35th IEEE Photovoltaic Specialists Conference (PVSC), pp.000493-000497, 20-25 June 2010, 2) J. H. Karp, E. J. Tremblay and J. E Ford, "Radial Coupling Method for Orthogonal Concentration within Planar Micro-Optic Solar Collectors," Optics for Solar Energy, OSA paper STuD2 (2010), and 3) J. H. Karp, E. J. Tremblay and J. E. Ford, "Orthogonal and secondary concentration in planar micro-optic solar collectors," Optics Express (*in preparation*). The dissertation author was the primary researcher and author of these publications.

4.8. References

- [1] R. Sherif, R. King, N. Karam, and D. Lillington, "The path to 1 GW of concentrator photovoltaics using multijunction solar cells," IEEE PVSC 31, 17-22 (2005).
- [2] J. C. Minano, "Application of the conservation of etendue theorem for 2-D subdomains of the phase space in nonimaging concentrators," Applied Optics **23**, 2021 (1984).
- [3] A.Rabl, *Active Solar Collectors and Their Applications* (Oxford University Press, 1985).
- [4] R. Winston and H. Hinterberger, "Principles of cylindrical concentrators for solar energy," Solar Energy **17**, 255-258 (1975).
- [5] J. C. Miñano, J. C. González, and P. Benítez, "A high-gain, compact, nonimaging concentrator: RXI," Applied Optics **34**, 7850 (1995).
- [6] N. Fraidenraich, "Analytic solutions for the optical properties of V-trough concentrators," Applied optics **31**, 131-9 (1992).

- [7] M. Collares-Pereira, A. Rabl, and R. Winston, "Lens-mirror combinations with maximal concentration," *Applied optics* **16**, 2677-83 (1977).
- [8] W. T. Welford and R. Winston, *High Collection Nonimaging Optics* (Academic Press, 1989).
- [9] L. Fu, R. Leutz, and H. P. Annen, "Secondary optics for Fresnel lens solar concentrators," *Proc. SPIE* 7785, 778509-6 (2010).
- [10] R. R. King, D. C. Law, K. M. Edmondson, C. M. Fetzer, G. S. Kinsey, H. Yoon, R. A. Sherif, and N. H. Karam, "40% efficient metamorphic GaInP/GaInAs/Ge multijunction solar cells," *Applied Physics Letters* **90**, 183516 (2007).
- [11] A. Barnett, D. Kirkpatrick, C. Honsberg, D. Moore, M. Wanlass, K. Emery, R. Schwartz, D. Carlson, S. Bowden, D. Aiken, A. Gray, S. Kurtz, L. Kazmerski, M. Steiner, J. Gray, T. Davenport, R. Buelow, L. Takacs, N. Shatz, J. Bortz, O. Jani, K. Goossen, F. Kiamilev, A. Doolittle, I. Ferguson, B. Unger, G. Schmidt, E. Christensen, and D. Salzman, "Very high efficiency solar cell modules," *Progress in Photovoltaics: Research and Applications* **17**, 75-83 (2009).

Chapter 5

Conclusions and Future Directions

This dissertation presents an investigation of a planar micro-optic concentrator for solar light collection. Inexpensive, large-aperture optical systems are essential to reducing the cost of electricity generated by CPV. To our knowledge, this is the first configuration which maintains a thin, uniform cross-section and enables large-scale manufacturing techniques such as roll-to-roll processing. The layout provides a new design space with several degrees of freedom including lens f-number, waveguide geometry and coupling prisms. The goal of this work was to design, fabricate and experimentally test planar micro-optic solar concentrators as a means address manufacturing, alignment and assembly concerns associated with CPV systems.

As an overview, I began by describing the micro-optic concentrator concept which couples light from thousands of millimeter-sized lenses to a common output aperture. 120° symmetric prisms reflected incident light at angles which guided by TIR. The unique coupler geometry avoided shadowing from neighboring facets, yielding a periodic structure which simplified alignment. Due to the uniform waveguide cross-section, guided light could interact with subsequent coupling regions and reflect out of the system as loss. Propagation efficiency within the waveguide became the primary loss mechanism which was managed through optical path length, lens f-number, waveguide materials and acceptance angles.

An analytic model balanced the tradeoff between propagation efficiency and concentration ratio. Using Zemax optical software, we raytraced and compared two system designs using air and fluoropolymer waveguide claddings. The different material sets altered the waveguide index contrast with air-claddings supporting plano-convex $f/2.45$ lenses and fluoropolymer claddings limited to $f/4.11$. Considering lens aberrations, dispersion and absorption, both systems approached 80% optical efficiency at 300x geometric concentration. The 9mm thick planar systems had 600mm diameter apertures which could be extended further to increase concentration ratio. The analytic model explored the initial design space for micro-optic concentration. Waveguide geometry and coupling area influence efficiency and acceptance angle for a variety of medium- and high-concentration designs.

Next, I presented fabrication and experimental results for two concentrator prototypes. We proposed a self-aligned fabrication approach in which coupling

prisms were molded into SU-8 photoresist. The lens array acted as the mask, cross-linking localized regions at the focal plane. We assembled a custom UV illumination source to mimic the divergence of the sun during exposure. The process was tolerant towards lens imperfections and ensured the size and spacing of waveguide couplers matched the characteristics of the lens array.

We presented two prototype concentrators using commercially available lens arrays and $50\mu\text{m}$ pitch, 120° prisms. The first-generation proof-of-concept used plano-convex $f/1.1$ lenses focusing to $200\mu\text{m}$ coupling regions. For this setup, we expected 44.8% optical efficiency and experimentally measured 32.4% at $37.5\times$. Lens aberrations and fill-factor led to suboptimal performance compared to systems with custom components. We fabricated a second experimental system using $f/3$ lenses focusing onto $80\mu\text{m}$ coupling regions which more closely matched optimal designs. Simulated and measured efficiencies increased to 76.2% and 52.3% respectively. Additional losses due to coating reflectivity and prism pitch accounted for the discrepancy between simulation and experimentation. These prototype systems demonstrated micro-optic concentration on a small scale and highlighted requirements of future experimental systems.

Next, I described two approaches to increase concentration ratios without adding propagation loss. The first approach modified the waveguide geometry to confine light along the slab width. Orthogonal concentration leveraged independent research using lenses focusing into simple v-trough concentrator. Based on étendue, decreasing the output area required an equal increase in angular spectrum. Properly

designing waveguide aspect ratios enabled systems to approach the thermodynamic limit in one dimension. We simulated an example waveguide with $f/3$ lenses and 8x orthogonal concentration to achieve 85% optical efficiency at 900x.

Another concentration method placed a secondary optical element between two opposing waveguides to combine the outputs onto a common PV cell. The nonimaging secondary used off-axis parabolic reflectors to increase the concentration ratio by 3.3x. We showed how secondary optics can be incorporated to increase efficiency and enable spectral separation. They can also be used in tandem with orthogonal concentration to reach very high concentration ratios while maintaining high efficiency.

We experimentally tested a simplified orthogonal concentrator which was diced from a rectangular waveguide. Using the same self-alignment process, we fabricated oriented coupling regions on the waveguide surface. A planar reflector directed all the light towards a single output. Despite simulations above 59% optical efficiency, we experimentally measured 22.4% at 131x. Waveguide sidewalls and index-matched reflectors accounted for most of the additional loss. Orthogonal and secondary concentration can potentially reach very high concentrations, but required precision optics and assembly which may complicate manufacturing.

In summary, micro-optic concentration presents a new design space for large-aperture collection optics. The planar cross-section enables systems to be manufactured using volume manufacturing techniques such as photolithography or

roll-to-roll processing. In this dissertation, I presented several simulated designs as well as experimental prototypes which highlighted the tradeoffs linked to each component. In conclusion, micro-optic concentration offers several new degrees of freedom which may be useful in addressing manufacturing, assembly and alignment concerns associated with concentrator photovoltaics.

5.1. Future Direction: Conformal Cladding

During fabrication and characterization of our prototype systems, we observed several unexpected loss mechanisms which reduced optical efficiency. I previously addressed reflectivity and prism pitch, yet altering the cladding design may further improve performance. Our current processing approach attempted to remove uncured regions of SU-8 trapped beneath a solid reflective coating. Development with heat and ultrasonics often caused regions of the reflector to lift and tear away from the underlying cross-linked couplers. Instead of attempting liftoff with SU-8 photoresist, we can apply a conformal cladding layer between the couplers and reflector. With a conformal cladding, the metallic reflector can be applied after chemical development and avoid using heat and agitation.

Upon first incidence, sunlight passes through the cladding and reflects off the underlying mirror to couple into the waveguide. With the cladding in place, guided light continues to TIR within planar waveguide regions. Conformal claddings also protect the slab surface from contaminants which can cause propagation loss. Materials such as low-index fluoropolymers have refractive indices approaching 1.3

and can be spun or dipped-coated onto the waveguide. Fabrication must overcome low surface energies associated with low-index polymers, though this configuration presents a promising direction for future systems.

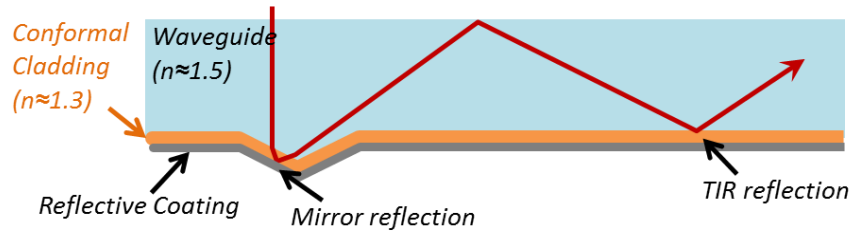


Figure 5.1 Conformal claddings enable metallization after development while supporting TIR within planar regions.

5.2. Future Direction: Lateral Micro-Tracking

Like all high-flux solar concentrators, micro-optic concentrators only accept a small range of incidence angles and must be combined with tracking mechanics. Segmented apertures and planar waveguides reduce system mass which enables tilt/roll tracking schemes instead of two-axis pedestals, yet both approaches occupy a significant portion of overall system cost. We can leverage the micro-optic concentrator geometry to extend solar acceptance angles and follow the sun without requiring bulk, two-axis motion.

Sunlight couples into the waveguide when the lens focus aligns to coupling regions. Under normal incidence, this focus lies along the lens axis. When the sun angle deviates from normal, the focus position begins to shift laterally. Off-axis sunlight can be captured by translating the waveguide with respect to the lens array.

Translation repositions coupling regions to different focus locations and maintains incidence on the prisms. Because each lens aperture is small in diameter, lateral motion only occurs within each lens pitch. We refer to this motion as lateral micro-tracking because it enables the concentrator to follow the sun's path using only millimeters of translation, regardless of the overall aperture dimensions.

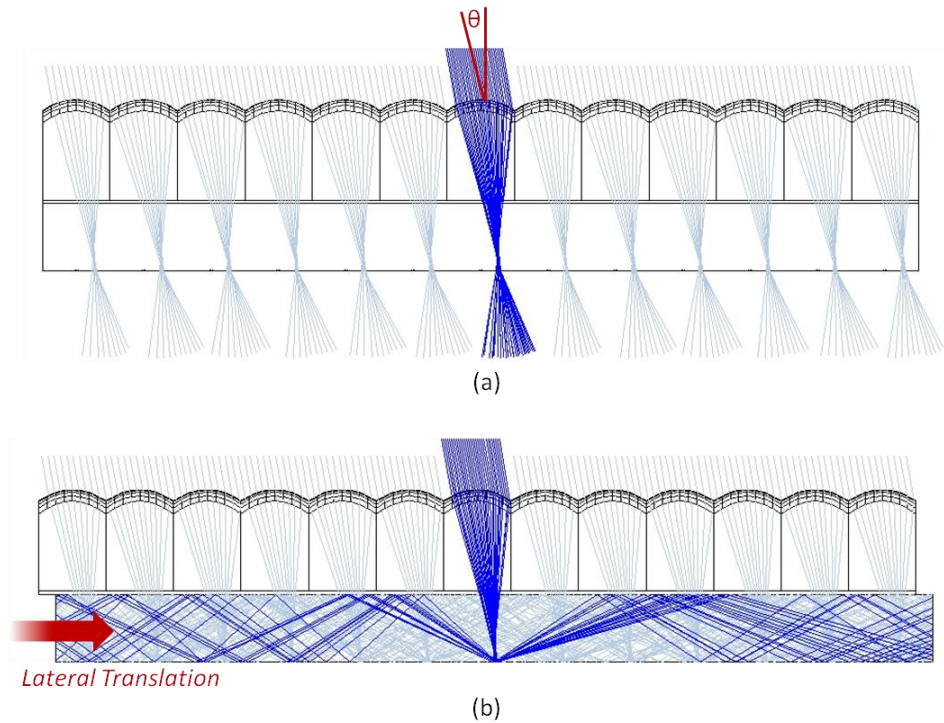


Figure 5.2 Off-axis lens focus misses waveguide coupling regions (a). Micro-tracking translates the waveguide, repositioning couplers to the shifted lens focus (b).

Micro-tracking off-loads some mechanical tracking duties onto the optics. In order to couple off-axis sunlight, the lens array must maintain a focus on the back waveguide surface without significant aberration. Simple plano-convex lenses develop coma and field curvature which increase the focused spot area and cause coupling and propagation loss. Micro-tracking requires new lens designs which

properly focus off-axis sunlight without vignetting, while using inexpensive components that can be fabricated in large arrays. When properly designed, micro-tracking provides a simple approach to relax solar alignment or even eliminate bulk tracking altogether.

Micro-tracking may be useful in applications beyond solar concentration. Free-space optical links often use concentrating optics to focus infrared data signals onto high-speed photodetectors. Planar micro-optic concentrators are wavelength independent and can be redesigned to function as large aperture receivers. With micro-tracking, these receivers can maintain alignment or select between multiple data sources. Though the challenges between solar concentration and free-space communication are quite similar, the latter is primarily focused on modulation frequency and not optical efficiency. Due to multiple paths to the output, concentration using waveguides must pay special attention to dispersion which degrades signal fidelity. Using the same overall concepts outlined in this dissertation, micro-optic concentrators can be redesigned for free-space communication applications with new emphasis on physical geometry and optical path length. Micro-tracking, in addition to orthogonal waveguides and secondary edge optics, highlight the flexibility of micro-optic concentration as a means to simplify system fabrication, assembly, alignment and mechanics.

Appendix A

Example Zemax Nonsequential Lens Prescription

System/Prescription Data

OBJECT DATA DETAIL:

There are 15 objects:

Object 1	:	Lens Array			
Object Type	:	Lenslet Array 1 (NSC_LET1)			
Face 0	:	Side Faces			
Face Is	:	Object Default			
Coating	:	(none)			
Scattering	:	None			
Face 1	:	Front Face			
Face Is	:	Object Default			
Coating	:	(none)			
Scattering	:	None			
Face 2	:	Back Face			
Face Is	:	Object Default			
Coating	:	(none)			
Scattering	:	None			
Face 3	:	Inside Faces			
Face Is	:	Object Default			
Coating	:	(none)			
Scattering	:	None			
Reference Object	:	0			
Inside Of	:	0			
XYZ Position	:	0	0	0	
Tilt About XYZ	:	0	180	0	

Pos. Mtrx. R11 R12 R13 X : -1.00000000E+000 0.00000000E+000 -7.65713740E-016 0.00000000E+000
 Pos. Mtrx. R21 R22 R23 Y : 0.00000000E+000 1.00000000E+000 0.00000000E+000 0.00000000E+000
 Pos. Mtrx. R31 R32 R33 Z : 7.65713740E-016 0.00000000E+000 -1.00000000E+000 0.00000000E+000
 Material : ACRYLIC
 X Half-Width : 0.5
 Y Half-Width : 0.5
 Thickness : 3.3
 Radius : -1.48
 Conic : 0
 Is Toric? : 0
 Toric R : 0
 Lines/ μ m : 0
 Diff Order : 0
 Coeff r^2 : 0
 Coeff r^4 : 0
 Coeff r^6 : 0
 Coeff r^8 : 0
 Coeff r^10 : 0
 Coeff r^12 : 0
 Coeff r^14 : 0
 Coeff r^16 : 0
 Decenter X : 0
 Decenter Y : 0
 Number In X : 1
 Number In Y : 100
 Diffract Face : 1

 Object 2 : Cladding
 Object Type : Rectangular Volume (NSC_RBLK)
 Face 0 : Side Faces
 Face Is : Object Default
 Coating : (none)
 Scattering : None
 Face 1 : Front Face
 Face Is : Object Default
 Coating : (none)
 Scattering : None
 Face 2 : Back Face
 Face Is : Object Default
 Coating : (none)
 Scattering : None
 Reference Object : 0
 Inside Of : 0
 XYZ Position : 0 0 0
 Tilt About XYZ : 0 0 0
 Pos. Mtrx. R11 R12 R13 X : 1.00000000E+000 0.00000000E+000 0.00000000E+000 0.00000000E+000
 Pos. Mtrx. R21 R22 R23 Y : 0.00000000E+000 1.00000000E+000 0.00000000E+000 0.00000000E+000
 Pos. Mtrx. R31 R32 R33 Z : 0.00000000E+000 0.00000000E+000 1.00000000E+000 0.00000000E+000
 Material :
 X1 Half Width : 0.5
 Y1 Half Width : 50
 Z Length : 0.061
 X2 Half Width : 0.5
 Y2 Half Width : 50
 Front X Angle : 0
 Front Y Angle : 0
 Rear X Angle : 0
 Rear Y Angle : 0

 Object 3 : Slab
 Object Type : Rectangular Volume (NSC_RBLK)
 Face 0 : Side Faces
 Face Is : Object Default
 Coating : (none)
 Scattering : None
 Face 1 : Front Face

```

Face Is      : Object Default
Coating      : (none)
Scattering   : None
Face 2      : Back Face
Face Is      : Object Default
Coating      : (none)
Scattering   : None
Reference Object : 2
Inside Of    : 0
XYZ Position :      0      0      0.061
Tilt About XYZ :      0      0      0
Pos. Mtrx. R11 R12 R13 X : 1.00000000E+000 0.00000000E+000 0.00000000E+000 0.00000000E+000
Pos. Mtrx. R21 R22 R23 Y : 0.00000000E+000 1.00000000E+000 0.00000000E+000 0.00000000E+000
Pos. Mtrx. R31 R32 R33 Z : 0.00000000E+000 0.00000000E+000 1.00000000E+000 6.10000000E-002
Material      : BK7
X1 Half Width :      0.5
Y1 Half Width :      50
Z Length      :      1
X2 Half Width :      0.5
Y2 Half Width :      50
Front X Angle :      0
Front Y Angle :      0
Rear X Angle  :      0
Rear Y Angle  :      0

Object 4      : spot
Object Type   : Null Object (NSC_NULL)
Reference Object : 0
Inside Of    : 0
XYZ Position :      0.07      0      0
Tilt About XYZ :      0      0      0
Pos. Mtrx. R11 R12 R13 X : 1.00000000E+000 0.00000000E+000 0.00000000E+000 7.00000000E-002
Pos. Mtrx. R21 R22 R23 Y : 0.00000000E+000 1.00000000E+000 0.00000000E+000 0.00000000E+000
Pos. Mtrx. R31 R32 R33 Z : 0.00000000E+000 0.00000000E+000 1.00000000E+000 0.00000000E+000
Material      :

Object 5      : single
Object Type   : Cylinder Volume (NSC_CBLK)
Face 0      : Side Faces
Face Is      : Object Default
Coating      : (none)
Scattering   : None
Face 1      : Front Face
Face Is      : Object Default
Coating      : (none)
Scattering   : None
Face 2      : Back Face
Face Is      : Object Default
Coating      : (none)
Scattering   : None
Reference Object : 3
Inside Of    : 3
XYZ Position :      0      0      1
Tilt About XYZ :      0      0      0
Pos. Mtrx. R11 R12 R13 X : 1.00000000E+000 0.00000000E+000 0.00000000E+000 0.00000000E+000
Pos. Mtrx. R21 R22 R23 Y : 0.00000000E+000 1.00000000E+000 0.00000000E+000 0.00000000E+000
Pos. Mtrx. R31 R32 R33 Z : 0.00000000E+000 0.00000000E+000 1.00000000E+000 1.06100000E+000
Material      : F2
Front R      :      0.035
Z Length     :      0.025
Back R       :      0.035

Object 6      : couplers
Object Type   : Array (NSC_ARRA)
Face 0      : Defined by Object 5 Face 0
Face 1      : Defined by Object 5 Face 1

```


Face 2 : Defined by Object 5 Face 2
 Reference Object : 5
 Inside Of : 3
 XYZ Position : 0 -49.5 0
 Tilt About XYZ : 0 0 90
 Pos. Mtrx. R11 R12 R13 X : -3.82856870E-016 -1.00000000E+000 0.00000000E+000 0.00000000E+000
 Pos. Mtrx. R21 R22 R23 Y : 1.00000000E+000 -3.82856870E-016 0.00000000E+000 -4.95000000E+001
 Pos. Mtrx. R31 R32 R33 Z : 0.00000000E+000 0.00000000E+000 1.00000000E+000 1.06100000E+000
 Material :
 Parent Object # : 5
 Number X' : 100
 Number Y' : 1
 Number Z' : 1
 Delta1 X' : 1
 Delta1 Y' : 1
 Delta1 Z' : 1
 X' - x : 1
 X' - y : 0
 X' - z : 0
 Y' - x : 0
 Y' - y : 0
 Y' - z : 0
 Z' - x : 0
 Z' - y : 0
 Z' - z : 0
 Tilt X : 0
 Tilt Y : 0
 Tilt Z : 0
 Draw Limit : 100
 Draw Boundary : 0
 Delta2 X' : 0
 Delta2 Y' : 0
 Delta2 Z' : 0
 Delta3 X' : 0
 Delta3 Y' : 0
 Delta3 Z' : 0
 Delta4 X' : 0
 Delta4 Y' : 0
 Delta4 Z' : 0
 Maximum X' : 99
 Maximum Y' : 0
 Maximum Z' : 0

 Object 7 : pitch
 Object Type : Null Object (NSC_NULL)
 Reference Object : 0
 Inside Of : 0
 XYZ Position : 0.05 0 0
 Tilt About XYZ : 0 0 0
 Pos. Mtrx. R11 R12 R13 X : 1.00000000E+000 0.00000000E+000 0.00000000E+000 5.00000000E-002
 Pos. Mtrx. R21 R22 R23 Y : 0.00000000E+000 1.00000000E+000 0.00000000E+000 0.00000000E+000
 Pos. Mtrx. R31 R32 R33 Z : 0.00000000E+000 0.00000000E+000 1.00000000E+000 0.00000000E+000
 Material :

 Object 8 : single prism
 Object Type : Rectangular Volume (NSC_RBLK)
 Face 0 : Side Faces
 Face Is : Reflective
 Coating : AL85
 Scattering : None
 Face 1 : Front Face
 Face Is : Object Default
 Coating : (none)
 Scattering : None
 Face 2 : Back Face
 Face Is : Object Default

Coating : (none)
 Scattering : None
 Reference Object : 3
 Inside Of : 0
 XYZ Position : 0 0 1.005
 Tilt About XYZ : 0 0 0
 Pos. Mtrx. R11 R12 R13 X : 1.00000000E+000 0.00000000E+000 0.00000000E+000 0.00000000E+000
 Pos. Mtrx. R21 R22 R23 Y : 0.00000000E+000 1.00000000E+000 0.00000000E+000 0.00000000E+000
 Pos. Mtrx. R31 R32 R33 Z : 0.00000000E+000 0.00000000E+000 1.00000000E+000 1.06600000E+000
 Material :
 X1 Half Width : 0.5
 Y1 Half Width : 1e-005
 Z Length : 0.01443
 X2 Half Width : 0.5
 Y2 Half Width : 0.025
 Front X Angle : 0
 Front Y Angle : 0
 Rear X Angle : 0
 Rear Y Angle : 0

Object 9 : prisms
 Object Type : Array (NSC_ARRA)
 Face 0 : Defined by Object 8 Face 0
 Face 1 : Defined by Object 8 Face 1
 Face 2 : Defined by Object 8 Face 2
 Reference Object : 8
 Inside Of : 6
 XYZ Position : 0 -50 0.014
 Tilt About XYZ : 0 180 0
 Pos. Mtrx. R11 R12 R13 X : -1.00000000E+000 0.00000000E+000 -7.65713740E-016 0.00000000E+000
 Pos. Mtrx. R21 R22 R23 Y : 0.00000000E+000 1.00000000E+000 0.00000000E+000 -5.00000000E+001
 Pos. Mtrx. R31 R32 R33 Z : 7.65713740E-016 0.00000000E+000 -1.00000000E+000 1.08000000E+000
 Material :
 Parent Object # : 8
 Number X' : 1
 Number Y' : 2000
 Number Z' : 1
 Delta1 X' : 0
 Delta1 Y' : 0.05
 Delta1 Z' : 0
 X' - x : 0
 X' - y : 0
 X' - z : 0
 Y' - x : 0
 Y' - y : 0
 Y' - z : 0
 Z' - x : 0
 Z' - y : 0
 Z' - z : 0
 Tilt X : 0
 Tilt Y : 0
 Tilt Z : 0
 Draw Limit : 1500
 Draw Boundary : 0
 Delta2 X' : 0
 Delta2 Y' : 0
 Delta2 Z' : 0
 Delta3 X' : 0
 Delta3 Y' : 0
 Delta3 Z' : 0
 Delta4 X' : 0
 Delta4 Y' : 0
 Delta4 Z' : 0
 Maximum X' : 0
 Maximum Y' : 99.95
 Maximum Z' : 0

```

Object 10      :
Object Type    : Null Object (NSC_NULL)
Reference Object : 0
Inside Of      : 0
XYZ Position   :          0          0          0
Tilt About XYZ :          0          0          0
Pos. Mtrx. R11 R12 R13 X : 1.00000000E+000 0.00000000E+000 0.00000000E+000 0.00000000E+000
Pos. Mtrx. R21 R22 R23 Y : 0.00000000E+000 1.00000000E+000 0.00000000E+000 0.00000000E+000
Pos. Mtrx. R31 R32 R33 Z : 0.00000000E+000 0.00000000E+000 1.00000000E+000 0.00000000E+000
Material       :

Object 11      : Center
Object Type    : Source Two Angle (NSC_SR2A)
Reference Object : 0
Inside Of      : 0
XYZ Position   :          0          0         -4.3
Tilt About XYZ :          0          0          0
Pos. Mtrx. R11 R12 R13 X : 1.00000000E+000 0.00000000E+000 0.00000000E+000 0.00000000E+000
Pos. Mtrx. R21 R22 R23 Y : 0.00000000E+000 1.00000000E+000 0.00000000E+000 0.00000000E+000
Pos. Mtrx. R31 R32 R33 Z : 0.00000000E+000 0.00000000E+000 1.00000000E+000 -4.30000000E+000
Source uses system wavelengths
# Layout Rays   :          0
# Analysis Rays :          0
Power(Watts)    :          1
Wavenumber      :          0
Color #         :          1
X Half Width    :         0.49
Y Half Width    :         0.49
X Half Angle (deg) :         0.26
Y Half Angle (deg) :         0.26
Spatial Shape   :          0
Angular Shape   :          0
Uniform Angle   :          0

Object 12      : ALL
Object Type    : Source Two Angle (NSC_SR2A)
Reference Object : 0
Inside Of      : 0
XYZ Position   :          0          0         -4.3
Tilt About XYZ :          0          0          0
Pos. Mtrx. R11 R12 R13 X : 1.00000000E+000 0.00000000E+000 0.00000000E+000 0.00000000E+000
Pos. Mtrx. R21 R22 R23 Y : 0.00000000E+000 1.00000000E+000 0.00000000E+000 0.00000000E+000
Pos. Mtrx. R31 R32 R33 Z : 0.00000000E+000 0.00000000E+000 1.00000000E+000 -4.30000000E+000
Source uses system wavelengths
# Layout Rays   :         100
# Analysis Rays :        7500
Power(Watts)    :         100
Wavenumber      :          0
Color #         :          3
X Half Width    :         0.475
Y Half Width    :         50
X Half Angle (deg) :         0.26
Y Half Angle (deg) :         0.26
Spatial Shape   :          0
Angular Shape   :          0
Uniform Angle   :          0

Object 13      : PV Top
Object Type    : Detector Rect (NSC_DETE)
Face 0        : All Faces
Face Is       : Object Default
Coating       : (none)
Scattering     : None
Reference Object : 3
Inside Of      : 3

```

```

XYZ Position      :      0      50      0.5
Tilt About XYZ    :      90      0      0
Pos. Mtrx. R11 R12 R13 X : 1.00000000E+000 0.00000000E+000 0.00000000E+000 0.00000000E+000
Pos. Mtrx. R21 R22 R23 Y : 0.00000000E+000 -3.82856870E-016 -1.00000000E+000 5.00000000E+001
Pos. Mtrx. R31 R32 R33 Z : 0.00000000E+000 1.00000000E+000 -3.82856870E-016 5.61000000E-001
Material          : ABSORB
X Half Width      :      0.5
Y Half Width      :      0.5
# X Pixels        :      25
# Y Pixels        :      25
Data Type         :      0
Color             :      0
Smoothing         :      0
Scale             :      0
Plot Scale        :      0
Front Only        :      0
PSF Wave#         :      0
X Angle Min       :     -90
X Angle Max       :      90
Y Angle Min       :     -90
Y Angle Max       :      90
Polarization      :      0
Mirroring         :      0

Object 14         : PV Bot
Object Type       : Detector Rect (NSC_DETE)
Face 0           : All Faces
Face Is          : Object Default
Coating          : (none)
Scattering        : None
Reference Object  : 3
Inside Of        : 3
XYZ Position      :      0     -50      0.5
Tilt About XYZ    :      90      0      0
Pos. Mtrx. R11 R12 R13 X : 1.00000000E+000 0.00000000E+000 0.00000000E+000 0.00000000E+000
Pos. Mtrx. R21 R22 R23 Y : 0.00000000E+000 -3.82856870E-016 -1.00000000E+000 -5.00000000E+001
Pos. Mtrx. R31 R32 R33 Z : 0.00000000E+000 1.00000000E+000 -3.82856870E-016 5.61000000E-001
Material          : ABSORB
X Half Width      :      0.5
Y Half Width      :      0.5
# X Pixels        :      25
# Y Pixels        :      25
Data Type         :      0
Color             :      0
Smoothing         :      0
Scale             :      0
Plot Scale        :      0
Front Only        :      0
PSF Wave#         :      0
X Angle Min       :     -90
X Angle Max       :      90
Y Angle Min       :     -90
Y Angle Max       :      90
Polarization      :      0
Mirroring         :      0

Object 15         :
Object Type       : Detector Polar (NSC_DETP)
Face 0           : All Faces
Face Is          : Object Default
Coating          : (none)
Scattering        : None
Reference Object  : 13
Inside Of        : 3
XYZ Position      :      0      0      0
Tilt About XYZ    :     180      0      0

```

Pos. Mtrx. R11 R12 R13 X : 1.00000000E+000 -0.00000000E+000 0.00000000E+000 0.00000000E+000
 Pos. Mtrx. R21 R22 R23 Y : 0.00000000E+000 1.14857061E-015 1.00000000E+000 5.00000000E+001
 Pos. Mtrx. R31 R32 R33 Z : 0.00000000E+000 -1.00000000E+000 1.14857061E-015 5.61000000E-001
 Material : ABSORB
 Maximum Angle : 90
 Radial Size : 1
 # P Pixels : 181
 # A Pixels : 180
 Mirroring : 0

COATING DEFINITIONS:

Coating Name: AL85 (IDEAL)

SOLVE AND VARIABLE DATA:

Surf	1	NSC Object	1	Parameter	2:	Pickup From	1	Scale	1.0000E+000	Offset	0.0000E+000	Column	Parameter 1
Surf	1	NSC Object	2	Parameter	4:	Pickup From	2	Scale	1.0000E+000	Offset	0.0000E+000	Column	Parameter 1
Surf	1	NSC Object	2	Parameter	5:	Pickup From	2	Scale	1.0000E+000	Offset	0.0000E+000	Column	Parameter 2
Surf	1	NSC Object	3	Parameter	1:	Pickup From	2	Scale	1.0000E+000	Offset	0.0000E+000	Column	Current
Surf	1	NSC Object	3	Parameter	2:	Pickup From	2	Scale	1.0000E+000	Offset	0.0000E+000	Column	Current
Surf	1	NSC Object	3	Parameter	4:	Pickup From	2	Scale	1.0000E+000	Offset	0.0000E+000	Column	Parameter 1
Surf	1	NSC Object	3	Parameter	5:	Pickup From	3	Scale	1.0000E+000	Offset	0.0000E+000	Column	Parameter 2
Surf	1	NSC Object	5	Parameter	1:	Pickup From	4	Scale	5.0000E-001	Offset	0.0000E+000	Column	X
Surf	1	NSC Object	5	Parameter	3:	Pickup From	4	Scale	5.0000E-001	Offset	0.0000E+000	Column	X
Surf	1	NSC Object	6	Parameter	2:	Pickup From	1	Scale	1.0000E+000	Offset	0.0000E+000	Column	Parameter 23
Surf	1	NSC Object	8	Parameter	3:	Pickup From	7	Scale	2.8860E-001	Offset	0.0000E+000	Column	X
Surf	1	NSC Object	8	Parameter	5:	Pickup From	7	Scale	5.0000E-001	Offset	0.0000E+000	Column	X
Surf	1	NSC Object	9	Parameter	6:	Pickup From	7	Scale	1.0000E+000	Offset	0.0000E+000	Column	X
Surf	1	NSC Object	11	Position Y	:	Pickup From	1	Scale	1.0000E+000	Offset	0.0000E+000	Column	Current
Surf	1	NSC Object	11	Parameter	2:	Pickup From	11	Scale	1.0000E+002	Offset	0.0000E+000	Column	Parameter 1
Surf	1	NSC Object	11	Parameter	7:	Pickup From	11	Scale	1.0000E+000	Offset	0.0000E+000	Column	Parameter 6
Surf	1	NSC Object	12	Position Y	:	Pickup From	1	Scale	1.0000E+000	Offset	0.0000E+000	Column	Current
Surf	1	NSC Object	12	Position Z	:	Pickup From	11	Scale	1.0000E+000	Offset	0.0000E+000	Column	Current
Surf	1	NSC Object	12	Parameter	6:	Pickup From	2	Scale	9.5000E-001	Offset	0.0000E+000	Column	Parameter 1
Surf	1	NSC Object	13	Position Y	:	Pickup From	3	Scale	1.0000E+000	Offset	0.0000E+000	Column	Parameter 2
Surf	1	NSC Object	13	Parameter	1:	Pickup From	3	Scale	1.0000E+000	Offset	0.0000E+000	Column	Parameter 1
Surf	1	NSC Object	13	Parameter	2:	Pickup From	3	Scale	5.0000E-001	Offset	0.0000E+000	Column	Parameter 3
Surf	1	NSC Object	13	Parameter	3:	Pickup From	13	Scale	5.0000E+001	Offset	0.0000E+000	Column	Parameter 1
Surf	1	NSC Object	13	Parameter	4:	Pickup From	13	Scale	5.0000E+001	Offset	0.0000E+000	Column	Parameter 2
Surf	1	NSC Object	14	Position Y	:	Pickup From	3	Scale	-1.0000E+000	Offset	0.0000E+000	Column	Parameter 2
Surf	1	NSC Object	14	Parameter	1:	Pickup From	3	Scale	1.0000E+000	Offset	0.0000E+000	Column	Parameter 1
Surf	1	NSC Object	14	Parameter	2:	Pickup From	3	Scale	5.0000E-001	Offset	0.0000E+000	Column	Parameter 3
Surf	1	NSC Object	14	Parameter	3:	Pickup From	13	Scale	5.0000E+001	Offset	0.0000E+000	Column	Parameter 1
Surf	1	NSC Object	14	Parameter	4:	Pickup From	13	Scale	5.0000E+001	Offset	0.0000E+000	Column	Parameter 2

Appendix B

Self-Aligned Fabrication Process

Prism Coupler Fabrication

1. Glass Cleaning
 - 1min sonication in Acetone
 - 1min sonication in Methanol
 - Rinse with IPA
 - Wash in DI water, Dry with nitrogen
 - Dehydrate glass - Bake on hotplate 200°C for 5min
 - Remove from heat and let cool to ~30°C
2. Spin-Coating - 20 μ m layer using MicroChem SU-8 10
 - Pour half dollar-sized amount of SU-8 onto glass (covers chuck ring)
 - 15s at 500rpm, acceleration = 100rpm/s
 - 30s at 2500rpm, acceleration = 300rpm/s
3. Soft Bake (on hotplate)
 - Bake 2min at 65°C
 - Ramp heat to 95°C (~4min)
 - Bake 5min at 95°C

- Turn off hotplate and let cool to $\sim 30^{\circ}\text{C}$
4. Prism Molding (Vacuum Oven)
 - Preheat vacuum oven to 60°C
 - Place PDMS mold onto spun photoresist layer (do not press)
 - Place 1kg aluminum block on top of PDMS mold
 - Insert into oven, raise thermostat to 95°C ($\sim 30\text{min}$ transition)
 - Pull vacuum (20-25 inHg)
 - Bake for a total of 45min
 - Vent chamber and let cool to $\sim 30^{\circ}\text{C}$ with mold still in contact
 5. UV Exposure
 - Turn on Hg arc lamp and exhaust fan. Warm up for $\sim 15\text{min}$
 - Place glass, SU-8 and mold onto exposure stage
 - Place lens array over glass and gently secure with clamps
 - Set Newport 818-ST to power integration (mJ/cm^2)
 - Exposure Parameters
 - a. $8.4\text{mrad} (\pm 0.25^{\circ}) - 90\text{mJ}/\text{cm}^2 - 14-18\text{min}$
 - b. $12.5\text{mrad} (\pm 0.34^{\circ}) - 175\text{mJ}/\text{cm}^2 - 12-14\text{min}$
 - c. $18.3\text{mrad} (\pm 0.52^{\circ}) - 300\text{mJ}/\text{cm}^2 - 13-15\text{min}$
 6. Post Bake (on hotplate)
 - Bake with PDMS mold in place to prevent resist reflow
 - Bake 2min at 65°C
 - Ramp plate to 95°C ($\sim 4\text{min}$)
 - Bake 3min at 95°C
 - Turn off hotplate and let cool to $\sim 30^{\circ}\text{C}$
 - Remove PDMS mold
 7. Metallization – AJA DC Sputter Deposition Tool
 - Place glass on wafer carrier. Cover edges with foil strips
 - Pull high vacuum - $< 5 \times 10^{-8}$ Torr
 - Sputter parameters – Vacuum to $5\text{e-}6$ mTorr, 2.7mTorr sputter pressure
 - a. 5 sccm Argon
 - b. 3mTorr sputter pressure
 - c. 9min deposition at 300W – 90nm Aluminum coating
 8. Development and Liftoff
 - Heat sonication bath to $> 65^{\circ}\text{C}$
 - Bake coated glass for 2min at 80°C (mirrored coating wrinkles)
 - Immediately place in glass into PGMEA developer and begin sonication
 - Sonicate for $\sim 30\text{s}$ until metal is removed (Do not over sonicate)

- Continue development in PGMEA for 1:30
- Wash with IPA, dry with nitrogen

PDMS Mold Fabrication

1. Prism Film Mounting
 - Cut slightly oversized section of original prism film
 - Cut CrystalBond WaferMount sheet to match film area
 - Place film and WaferMount on 4" glass wafer
 - Bake for 5min at 125°C (ensure CrystalBond is thoroughly heated)
2. Silanation (anti-stick surface treatment)
 - Place glass wafer and prism film in silane-specific vacuum chamber
 - Place ~5 drops of silane into crucible
(Tridecafluoro-1,1,2,2-Tetrahydrooctyl)-1-Trichlorosilane
 - Pull vacuum (>30inHg) and let stand for 10min
3. Prepare PDMS (Sylgard 184 silicone elastomer)
 - Mix 30g of PDMS base with 3g of hardening agent
 - Pull vacuum (>30inHg) until bubbles settle out (~20min)
4. Mold Fabrication
 - Place mounted film inside lid of plastic wafer dish
 - Level lid on a cool hotplate
 - Slowly pour PDMS to cover film and wafer
 - Pull vacuum (>30inHg) to remove final bubbles
 - Bake for 4hrs at 70°C
5. Final Cut and Coating
 - Cut around glass wafer with razor and remove from plastic dish
 - Trim edges until PDMS mold peels away from film and wafer
 - Cut out final shape from PDMS
 - Repeat Step 2 to Silane coat PDMS mold
6. To Clean PDMS Mold after use
 - Rinse 2min in PGMEA developer
 - Rinse 2min in IPA
 - Bake for 5min at 95°C to remove absorbed solvent

Appendix C

Integrated Diffractive Shearing Interferometry for Adaptive Wavefront Sensing

This appendix includes published research which was part of my advancement to candidacy. The work centers around a different planar micro-optic device using a diffraction grating mounted to an image sensor for wavefront phase detection. The following is a reprint which appears in:

- J. Karp, T. Chan, and J. Ford, “Integrated diffractive shearing interferometry for adaptive wavefront sensing,” *Appl. Opt.* 47, 6666-6674 (2008).

The dissertation author was the primary researcher and author.

Integrated diffractive shearing interferometry for adaptive wavefront sensing

Jason H. Karp,* Trevor K. Chan, and Joseph E. Ford

Department of Electrical and Computer Engineering, University of California,
San Diego, 9500 Gilman Drive, La Jolla, California 92093-0407, USA

*Corresponding author: jkarp@ucsd.edu

Received 3 July 2008; revised 1 October 2008; accepted 4 November 2008;
posted 6 November 2008 (Doc. ID 98299); published 8 December 2008

We present theory, design, and preliminary experimental studies for a compact wavefront sensor based on lateral shearing interferometry using a binary phase grating, image sensor, and Fourier-based processing. The integrated system places a diffractive element directly onto an image sensor to generate interference fringes within overlapping diffraction orders. The shearing ratio and the interferogram signal-to-noise ratio directly affect the reconstruction accuracy of wavefronts with differing spatial variations. Optimal shearing parameters associated with the autocorrelation of the input encourage placing a spatial light modulator as the diffractive element allowing adaptive wavefront sensing. Experimental results from a fixed-grating system are presented as well as requirements for next-generation adaptive systems. © 2008 Optical Society of America

OCIS codes: 070.6120, 110.3175, 130.3120.

1. Introduction

Wavefront sensing describes phase-sensitive detection from optical path differences (OPDs) within a field. Optical wavefront sensors are used in metrology applications ranging from corrective vision surgery to adaptive free-space communication. All wavefront sensors map phase information into intensity variations for detection. Several types of system exist based on their mapping techniques. Phase shifting interferometry forms a linear intensity pattern on the object surface and scans through a set phase shifts to visualize the OPD [1]. Shack–Hartmann (SH) sensors place a lens array above an image sensor, resulting in focal-spot position shifts relating to local wavefront tilt [2]. Lateral shearing interferometry (LSI) overlaps a wavefront with shifted replicas of itself, creating an interferogram with differential phase contours.

SH sensors have gained significant attention in the past decade owing to their compact and integrated form factor that lends itself well to practical

devices. Commercial Hartmann masks consist of a two-dimensional array of lenses to sample the incoming wavefront and focus onto a high-resolution image sensor. Aberrations such as coma, spherical and astigmatism, as well as tilt and defocus can be calculated from the spot field and are especially useful in adaptive-optic feedback loops. However, one must assume the maximum tilt and spatial frequency of the aberration when selecting the lenslet and detector parameters. Spatial variations smaller than the lens diameter are not sampled. Large local tilts form focal spots behind adjacent lenses, leading to identification errors [2]. SH devices can be sensitive to over $\lambda/20$ but place an upper bound on the dynamic range of the wavefront due to the trade-off defined by the sensor and lens selection.

Optical interferometry offers exceptional sensitivity relating to the short wavelength of visible or infrared light. Twyman–Green and Fizeau interferometers are commonly used in astronomy and aberrometry along with deformable mirrors to compensate for atmospheric distortions. Traditional interferometers such as these require strict alignment and vibration isolation to produce stable

0003-6935/08/356666-09\$15.00/0
© 2008 Optical Society of America

fringes, since a reference arm is needed to interfere with the aberrated wavefront arm [3]. Ronchi first proposed the use of linear patterns imaged onto mirrors to observe phase distortions [4], and this technique is the basis for using LSI as a wavefront sensor. LSI generates an interferogram by overlapping copies of an identical wavefront with induced lateral shift and/or tilt. Michelson, Mach-Zehnder, and Sagnac interferometers can all be designed for lateral shearing; however, our focus is on diffractive shearing [5,6]. The self-referenced design inherent to LSI removes vibration and isolation concerns, since no planar reference arm is used. This is also a drawback. The interferogram embeds phase information between two unknown signals, thereby requiring postprocessing and reconstruction algorithms. Despite the added computation, adjustable shear magnitude is a degree of freedom inherent to LSI and is not found in other sensing techniques. This parameter can provide varied levels of sensitivity based on the type and severity of the input aberration, allowing LSI to potentially surpass limitations restricting other wavefront sensing modalities.

2. Integrated Diffractive Shearing

Integrated wavefront sensors are finding uses in a broad range of new applications because of their ability to stand alone as a complete system. An integrated system refers to a compact optical setup, including all devices and sensors, aligned and mounted in an all-inclusive package. SH devices are excellent examples of integrated wavefront sensors; but sensitivity trade-offs lead to reduced resolution at certain wavefront aberrations. Our goal in this work is to explore the design and limitations of a LSI diffractive wavefront sensor with adjustable sensitivity to accommodate a wide range of profiles.

LSI first creates replicas of an unknown wavefront and overlaps them with some shift and/or tilt to form an interference pattern within the overlapping area. The contours associated with the fringe pattern differ significantly as the lateral shear distance changes, because no known reference phase front is present. Parallel plate surface reflections and grating diffraction orders are two methods for generating the overlapping beam replicas needed for LSI [5]. Gratings can have very high diffraction efficiencies, thereby using the illumination effectively compared with surface reflections, and gratings remain the focus of this work.

Interference fringes occur only in the area of overlap, directly relating to the OPD between the points of intersection. Measuring a two-dimensional field requires two nonparallel shears, often performed in orthogonal directions. Figure 1 depicts several approaches to shearing along multiple dimensions. A one-dimensional grating can be physically rotated between two positions to acquire time-sequential measurements of the wavefront. Also a pair of orthogonal gratings can produce separated sets of interferograms that can be analyzed by using multiple

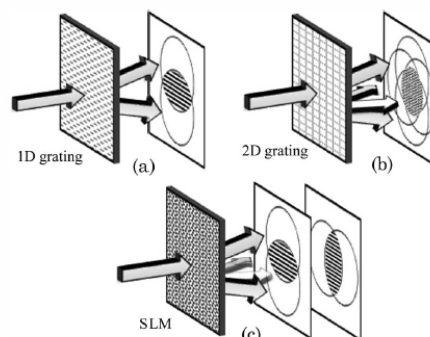


Fig. 1. Diffractive elements perform LSI by overlapping diffraction orders. (a) Information about the wavefront is obtained along the shearing direction. (b) Two-dimensional gratings simultaneously record the entire field while (c) SLMs sequentially create multiple interferograms.

detectors [7]. Multiorder gratings divide wavefronts into several replicas that simultaneously overlap [8]. The resulting interference provides additional sets of fringes between nonparallel diffraction orders but reduces interferogram contrast and imposes further sampling constraints. Most interesting is an electrically addressable element such as a spatial light modulator (SLM) to display gratings of different periods and orientations. This permits shearing variability within a two-dimensional field. Feedback increases system sensitivity and dynamic range by changing the shear on the basis of characteristics of the wavefront.

The simplest demonstration of an integrated, diffractive interferometer places a fixed grating directly on the surface of an image sensor. This setup provides only one-dimensional shearing; however, it is used to test processing algorithms and identify performance requirements for variable LSI designs. Section 3 details the theory behind diffractive shearing including spectral processing and wavefront reconstruction steps. Preliminary experimental results for a fixed grating device are shown in Section 4. Section 5 highlights the benefits of variable shearing and emphasizes the potential gains realized by substituting a SLM for the fixed grating. Section 6 is dedicated to the physical specifications and requirements of the SLM for an adaptive wavefront sensor. Concluding remarks are made in Section 7.

3. Description of LSI Method

The amplitude and phase of a general field are defined by $|f(x,y)| \exp[j\phi(x,y)]$, and a laterally shifted version can be written as $|f(x-s,y)| \exp[j\phi(x-s,y)]$, where s is the magnitude of a one-dimensional shift. The resulting intensity occurring from interference appears as

$$g(x,y) = |f(x,y)| \exp[j\phi(x,y)] + |f(x-s,y)| \exp[j\phi(x-s,y)]^2 \quad (1)$$

and can be expressed in the form

$$g(x,y) = a(x,y) + b(x,y) \cos[\phi(x,y) - \phi(x-s,y)] \quad (2)$$

with

$$a(x,y) = |f(x,y)|^2 + |f(x-s,y)|^2, \quad (3)$$

$$b(x,y) = 2|f(x,y)||f(x-s,y)|. \quad (4)$$

The cosine term in Eq. (2) depends on the relative phase difference between the fields and is the desired quantity for wavefront sensing. This signal is embedded along with other irradiance variations and is typically measured with contour mapping in cases with known reference arms.

Passing the original field through a diffraction grating causes the light to split into multiple orders, each being a copy of the original, tilted at an angle θ_m defined by the grating equation at normal incidence

$$\sin \theta_m = m \frac{\lambda}{d}, \quad (5)$$

where m refers to the diffraction order at wavelength λ and grating period d . Diffractive replication is useful, since it not only creates lateral separation s when allowed to propagate, but also incorporates a modulation frequency f_o within the cosine term. This is due to the linear OPD between the tilted diffraction orders (Fig. 2). The interference intensity between diffraction orders α and β is written as

$$g(x,y) = a(x,y) + b(x,y) \cos[\phi(x,y) - \phi(x-s,y) + 2\pi f_o x], \quad (6)$$

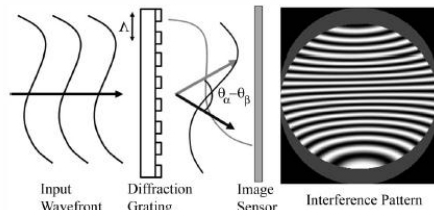


Fig. 2. Diffraction angles create a linear fringe pattern within the interferogram. Wavefront aberrations distort the carrier pattern, which is spectrally processed.

$$f_o = \frac{\sin(\theta_\alpha - \theta_\beta)}{\lambda}. \quad (7)$$

The spatial variation introduced by f_o is typically fast compared with the terms in Eqs. (3) and (4) and acts as a carrier frequency for the phase difference signal. Well-separated peaks appear in the spectral domain, allowing the differential phase component to be isolated from other intensity variations [9]. To highlight the phase detection steps, Eq. (6) is rewritten in the form

$$g(x,y) = a(x,y) + c(x,y) \exp(i2\pi f_o x) + c^*(x,y) \exp(-i2\pi f_o x), \quad (8)$$

where

$$c(x,y) = \frac{1}{2} b(x,y) \exp[i\phi(x,y) - i\phi(x-s,y)] \quad (9)$$

and $*$ denotes the complex conjugate. Fourier transformation of Eq. (8) yields Eq. (10), with capital letters referring to the Fourier spectra and ω_α the spatial frequency in the α direction:

$$G(\omega_x, \omega_y) = A(\omega_x, \omega_y) + C(\omega_x - f_o, \omega_y) + C^*(\omega_x + f_o, \omega_y). \quad (10)$$

Modulation from the tilted wavefronts is seen as shifts in the spectrum, allowing the phase measurement to be isolated with a single sideband spectral filter (Fig. 3). The phase difference signal results in spectral broadening of the modulation peak and affects the width of the required filter.

The carrier may be demodulated by shifting the filtered sideband toward the origin. This is viable only for theoretical, single-frequency carriers and may lead to residual Fourier components in experimental scenarios. In practice, the gradient phase measurement is mixed with a reference interferogram acquired by shearing and overlapping a collimated field [10]. Let $c_m(x,y)$ represent the complex signal of the differential phase as seen in Eq. (9) and

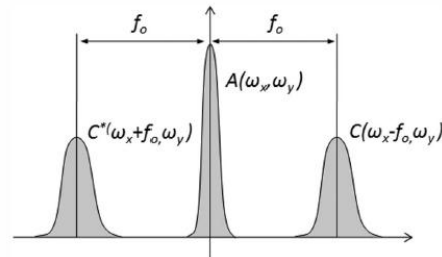


Fig. 3. Carrier modulation allows the phase difference signal to be isolated from other illumination components. The spectral width of the sidebands contains the phase information.

$c_r(x, y)$ correspond to the complex measurement formed from shearing a plane wave as a reference pattern. The phase gradient can be retrieved through the relation

$$\phi(x, y) - \phi(x - s, y) = \arctan \left[\frac{\text{Re}\{c_r(x, y)\} \text{Im}\{c_m(x, y)\} - \text{Im}\{c_r(x, y)\} \text{Re}\{c_m(x, y)\}}{\text{Im}\{c_r(x, y)\} \text{Im}\{c_m(x, y)\} + \text{Re}\{c_r(x, y)\} \text{Re}\{c_m(x, y)\}} \right], \quad (11)$$

where Re and Im represent the real and imaginary components, respectively. The additional reference measurement is performed only once for a given carrier. Mixing is superior to spectral translation because it removes all frequencies associated with the carrier, including additional frequencies stemming from illumination aberrations. The signal resulting from Eq. (11) uncovers the differential phase measurement of the field, wrapped from $-\pi$ to π . Care must be taken during phase unwrapping schemes to avoid streaks emanating from discrete points of residue [11].

The phase difference is the difference between the original field and a sheared copy, thereby representing slope information in the direction of the shear. To analyze an entire two-dimensional wavefront, shearing and analysis must be performed along two nonparallel directions. Multidirectional phase derivatives generated from multilateral shearing produce additional signals that aid in reconstruction accuracy, despite adding complexity to the detection process [8]. Note that the piston term associated with optical aberrations cannot be detected by using LSI. Periodic aberrations with identical frequencies to the carrier are not seen, since no subtraction signal results.

At this point, slope information about the wavefront has been extracted from the modulated interferogram. To estimate the three-dimensional profile of the wavefront itself, the measured signal must undergo spatial integration. Several mathematical algorithms based on least-squares fitting and modal estimation have been proposed for differential wavefront reconstruction [12–15]. Our implemented technique is a generalization based on modal estimation methods proposed by Elster and Weingartner [16,17], which rely on an inverse Fourier filter known as the shearing transfer function. Let the discrete phase difference along each orthogonal direction in an $N \times N$ field be written as

$$\Delta\phi_x(m, n) = \phi(m, n) - \phi(m - s, n), \quad (12)$$

$$m, n = 0, 1, 2, \dots, N - 1,$$

$$\Delta\phi_y(m, n) = \phi(m, n) - \phi(m, n - s), \quad (13)$$

$$m, n = 0, 1, 2, \dots, N - 1,$$

where s is the discrete lateral shear distance in samples. The shift theorem of Fourier transforms states that a translation in space introduces a linear phase shift in frequency [18]:

$$\text{FT}\{\Delta\phi_x(m, n)\} = \text{FT}\{\phi(x, y)\} \left[1 - \exp\left(-\frac{i2\pi\omega_x s}{N}\right) \right], \quad (14)$$

$$\text{FT}\{\Delta\phi_y(m, n)\} = \text{FT}\{\phi(x, y)\} \left[1 - \exp\left(-\frac{i2\pi\omega_y s}{N}\right) \right]. \quad (15)$$

The bracketed exponentials in Eqs. (14) and (15) are known as shearing transfer functions. Dividing the right-hand side by this term isolates the spectral frequencies of the wavefront profile along each shearing direction. The final spatial form of the data is recovered with a simple inverse transform.

The shearing transfer function has an inherent drawback regarding frequency poles occurring at multiples of N/s , causing the exponential to become zero. These Fourier components will be lost, but may be replaced by averaging values from adjacent points, i.e., letting $\text{FT}_x(m, n) = [\text{FT}_x(m + 1, n) + \text{FT}_x(m - 1, n)]/2$. Estimating the missing information may result in reconstruction error; however, it is tolerable provided that the shear s does not create an excessive number of leakage points [19].

The concept of integration over the slope measurement leads to one final point of ambiguity regarding the size of the overlapping region relative to the size of the input wavefront. The common area between the wavefront and its sheared copy is of dimension $(N - s) \times N$. The wavefront under test is $N \times N$. This dimensional mismatch hinders the direct application of the shearing transfer function and requires data preprocessing through a periodicity constraint de-

finer by the periodicity inherent to the exponential basis functions of the inverse filter. The idea is known as the natural extension of the difference function, which was obtained in [16,17].

Periodicity within the differential wavefront occurs when the summation of each row or column has a zero sum. Considering the special case where s is an integer multiple of N , the gradient phase may be extended by using

$$\Delta\phi_x(m, n) = - \sum_{p=0}^{(N/s)-1} \Delta\phi_x(m + ps, n), \quad (16)$$

$$m = 0, 1, 2, \dots, s-1, \quad n = 0, 1, 2, \dots, N-1;$$

$$\Delta\phi_y(m, n) = - \sum_{q=0}^{(N/s)-1} \Delta\phi_y(m, n + qs), \quad (17)$$

$$n = 0, 1, 2, \dots, s-1, \quad m = 0, 1, 2, \dots, N-1.$$

For the general case when s is not an integer multiple of N , similar treatment is still possible by first extending the measurement data beyond the desired $N \times N$ size until the constraint is met. Some data interpolation and smoothing is necessary to suitably meet the above requirement; however, only the solution within the $N \times N$ interval is retained. The added capability to utilize any shear distance provides powerful insight regarding input aberration types and noise relationships, which are explored in Section 5. To summarize the process of wavefront reconstruction from an arbitrary gradient phase measurement, the following steps are necessary:

- Impose periodicity via natural extension so that each row and column of the gradient has zero sum and $N \times N$ dimensions.
- Fourier transform each array of phase differences.
- Perform integration through division with the shearing transfer function.
- View the reconstructed wavefront by using inverse Fourier transformation.

4. Fixed Diffractive Shearing Experiment

The integrated LSI consists of a one-dimensional binary phase grating mounted directly onto the surface of a CMOS image sensor. The grating has 42 lines/mm and is designed for 1064 nm illumination. Shearing is performed by allowing the ± 1 st diffraction orders to propagate within the 2 mm thickness of the grating substrate. Binary phase patterns are ideal for LSI because of their strong first-order diffraction and zero-order suppression.

The diffraction orders overlap at the sensor plane to create 11.2 μm carrier fringes. The carrier must be sampled at a rate higher than the Nyquist frequency to avoid aliasing of modulated gradient data. Con-

sely, dense sampling of the fringe places spectral sidebands close to the origin, requiring a narrow spectral filter that may not encompass all gradient phase spectral components. The carrier should be sampled so as to provide good separation from the origin and appropriate bandwidth on both sides of the spectral peak and avoid aliasing of the modulated data.

A 2 megapixel monochrome CMOS sensor with a 3.2 μm pixel pitch is chosen to detect the interference pattern formed on its surface. The phase object under test is a plano-convex lens with a 100 mm focal length. Though 3.5 pixel sampling per fringe period is within the defined sampling criteria, practical problems prevent the sensor from accurately identifying the carrier and distinguishing small deviations in periodicity. Coherent speckle and moiré are dominant noise sources that corrupt spectral information when few samples span the carrier. Additionally, high-order diffraction gives rise to aliased interference fringes that overlap the carrier frequency, further hindering detection. The rectangular image in Fig. 4(a) shows the interferogram captured by the system in Fig. 4(b), which overfills the sensor array. Poor carrier modulation and moiré are clearly seen in Fig. 4(c), which ultimately damage the sensitive phase information.

The system is modified to include a 3.6 \times magnifying 4F relay to decrease the diffraction angle and thereby increase the fringe period. The grating is no longer attached to the CMOS sensor, but instead resides within the front focus of the relay. The relay system reduces the dynamic range by shrinking the usable sensor bandwidth. The modifications can be avoided by selecting a grating with a slightly larger pitch or by selecting a higher-resolution sensor to accommodate both sampling and environmental concerns. The modified system is used solely for verification of the processing methods described in Section 3.

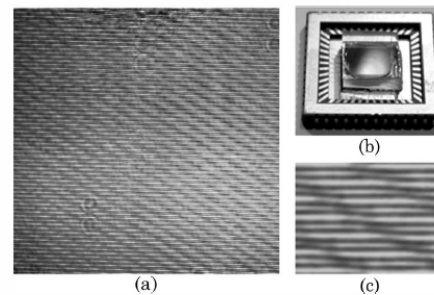


Fig. 4. (a) Low sampling and moiré disrupt the carrier modulation seen using (b) an integrated device consisting of a fixed phase grating and image sensor. (c) Poor detection of the horizontal carrier fringes is seen in the magnified view.

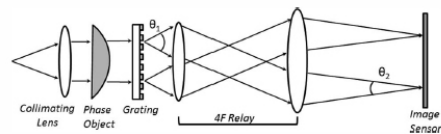


Fig. 5. Integrated LSI is modified by using a 4F relay with magnification to reduce the diffraction angle from θ_1 to θ_2 and increase the carrier period.

The optical setup in Fig. 5 is used to measure the radius of curvature of the 100 mm focal length, plano-convex lens. The imager sensor is rotated 60° with respect to the grating orientation to minimize moiré between the interference pattern and the pixel array. The spherical wavefront emanating from the lens is captured, reconstructed, and compared with a surface profile measurement performed using an interference microscope (Fig. 6). The measured radius of curvature differs by 9.2% and may be attributed to measuring the phase front just after the lens, and not directly at the lens plane. Much of the measurement difficulty stems from the small signal generated from shearing a slowly varying wavefront. Increasing the lateral shift significantly disrupts the carrier periodicity, resulting in larger spectral components that stand out against the background noise. The impact of the shearing ratio is discussed in the following section.

5. Shearing Ratio

The lateral shear distance is one adjustable quantity that separates LSI from fixed wavefront sensing techniques such as SH. The shearing ratio is defined as the fractional shift within the normalized field size. Shearing ratios of 0.01 overlap 99% of the wa-

vefront, while 1.0 creates no common interference area and provides no gradient information.

The shearing ratio governs a trade-off between overlapping field size and magnitude of the differential signal. Large areas of overlap maximize the number of data points to create an accurate estimation of the wavefront profile by minimizing data extension. However, since spatial phase variation is typically slow compared with the sample pitch, the resulting difference measurement for small shears is diminutive and difficult to detect, especially in the presence of noise. Large shearing ratios interfere substantially separated field points to yield an increased OPD at the cost of a reduced common area. This scenario requires additional data extension and increases the likelihood of reconstruction error. The significance of altering the shear ratio can be seen visually in Fig. 7, with small shears producing near periodic fringes, while increasing the shear further disrupts carrier regularity. The distorted fringes in Fig. 7(c) contain more Fourier content, which stands out in noisy environments.

Simulations are performed by using rectangular data sets versus circular ones for geometric simplicity. Sets of Zernike polynomials generate the input phase profile. These are sheared to form synthesized interferograms to process under the algorithm described in Section 3. Two specific wavefronts are simulated, encompassing the cases of slow phase changes, Fig. 8(a), and increased spatial variation, seen in Fig. 8(b). The frequency of spatial variations is associated with certain aberration types. Spherical and coma lead to slow changes, while high-order aberrations cause faster spatial variations.

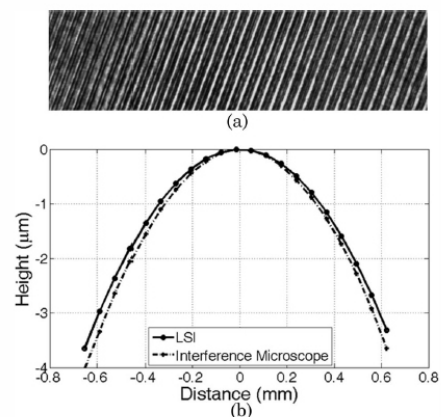


Fig. 6. (a) A section of the interferogram captured from the modified LSI is used to reconstruct the spherical profile. (b) The lens profile is compared with a phase-shifting microscope.

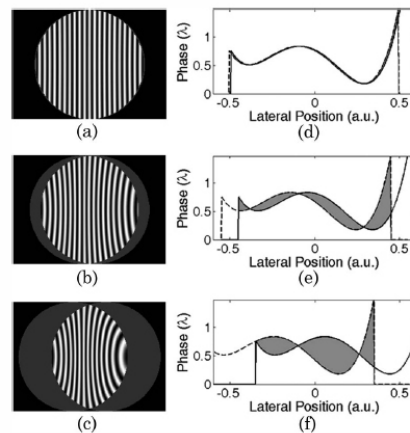


Fig. 7. OPDs between the sheared points of overlap disrupt fringe carrier periodicity. Adjusting the shearing ratio from (a) 0.01 to (b) 0.1 and (c) 0.3 increases the difference signal highlighted in (d), (e), and (f), respectively.

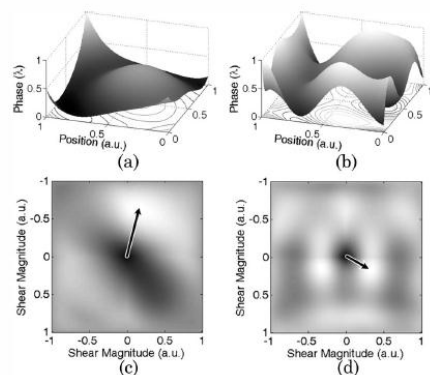


Fig. 8. Autocorrelation maps identify the shift needed for maximum OPD. (a) Wavefronts exhibiting slow spatial variation produce (c) large difference signals with large shears while (b) increased spatial variation requires (d) smaller shifts.

The spatial autocorrelation of the phase profile is a measure of similarity between the field and shifted versions of itself. Autocorrelation is similar to convolution, except it results in the difference between probability distributions of the signals instead of the sum. The output measurement is always twice as large in dimension as the input and is maximal at the origin. Maps of the autocorrelation are seen in Figs. 8(c) and 8(d). The distance between the maximum (origin) and minimum pinpoints the shift that yields the greatest OPD within the wavefront. The magnitude and direction of this shift is highlighted by arrows within the figures. A single shift along the identified direction maximizes the differential signal; however, a pair of shears is needed to span the two-dimensional field. The highlighted vector is broken down into orthogonal shear components along the rows and columns. The synthesized wavefront with slow spatial change has greatest signal from shears of 0.62 and 0.17 along the rows and columns, respectively. Alternatively, shifts of 0.13 and 0.32 along the rows and columns result in the largest phase difference when analyzing the wavefront with increased spatial variation. The autocorrelation map identifies the optimum shearing ratio based only on the wavefront profile, ignoring impacts from data extension and interferogram noise.

To investigate the relationship between shearing ratios and interferogram noise, white Gaussian noise is added to each synthesized interferogram prior to processing. The signal-to-noise ratio (SNR) is computed in decibels as the logarithm of the ratio between normalized fringe intensity and random background noise. The added noise affects the contrast of the interferogram and coincides with spectral frequencies of the differential phase data. The root-mean-square (RMS) error in wavelengths between

the final wavefront reconstruction and the known input is used as the figure of merit.

The profile of the reference wavefront seen in Fig. 9(a) is sheared by using equal, orthogonal ratios spanning from 0.01 to 0.7. Gaussian noise is added to each interferogram to simulate SNRs ranging from 40 to 20 dB. The effect on reconstruction is seen in Figs. 9(b)–9(d). Decreased SNR causes measurement errors in the gradient, which leads to streaks along each direction of integration. Ripples manifest from combining reconstructions along each direction, adversely affecting the overall smooth profile. SNRs below 10 dB completely lose details of the wavefront, capturing only a rough estimate of the general profile shape. Simulated SNRs above 30 dB exhibit very accurate reconstructions with less than $\lambda/100$ error. The RMS is plotted as a function of shearing ratio for increasing SNR values in Fig. 10(a). The curves identify specific shearing values that yield reconstruction error minimums. At high SNRs, small shearing ratios yield the lowest reconstruction error. Small disruptions in fringe periodicity stand out in the high contrast of the interferogram. As noise levels rise, error minimums initially appear at 0.12 and more significantly at 0.53 shearing ratios. These values are slightly less than the shear optima identified by autocorrelation. Differential signal strength versus overlap area will have diminishing returns on error improvement due to increased data extension. The plots in Fig. 10 are for identical shear values along both orthogonal directions. Allowing independent shear magnitudes along the rows and columns to better model the shift direction identified by autocorrelation lowers the RMS error by 8.2% at 20 dB.

The second wavefront with increased spatial variation in Fig. 8(b) is simulated under the same shearing and noise conditions. Observing the RMS error versus shearing ratio in Fig. 10(b) yields best

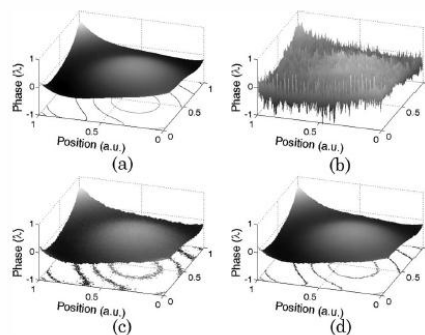


Fig. 9. (a) Simulated reference wavefront sheared and with Gaussian noise added to the interferogram prior to processing. Reconstructions from (a) 10 dB, (b) 20 dB, and (c) 30 dB SNRs. A low SNR loses all profile detail, while a high SNR creates reconstructions with $>\lambda/100$ accuracy.

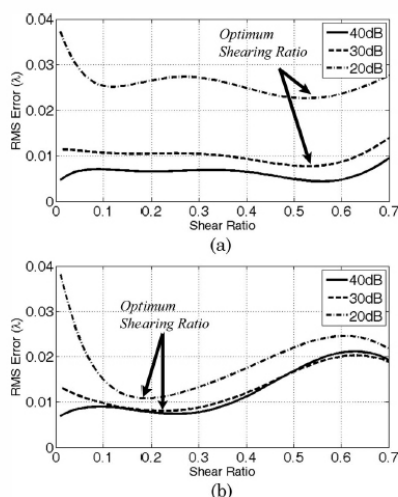


Fig. 10. Varying the shear ratio at different SNRs leads to reconstruction error minimums that depend on the wavefront profile. (a) Slowly varying wavefronts benefit from large shears, while (b) smaller shears perform best for increased spatial variation.

reconstructions at shifts between 0.18 and 0.22. These values are once again in close agreement with those determined from autocorrelation. Including independent shearing along each direction further reduces the RMS error by 2.3%. The optimal shear in each scenario is significantly different, suggesting that reconstruction accuracy exhibits strong dependence on the type and frequency of the aberrations present. A system that can actively change the shearing ratio in response to different input wavefronts can achieve greater accuracy and dynamic range over a wide variety of potential input profiles.

6. Variable LSI Sensor

To create variable lateral shearing, the propagation distance between a fixed grating and sensor can simply be adjusted, allowing the tilted orders to separate. Other implementations vary the rotation angle between a series of crossed gratings [20,21] or rely on rotation within Talbot self-imaging to alter the region of overlap [22]. Mechanical motion and tight tolerances associated with these techniques are not ideal for integrated devices.

Alternatively, liquid-crystal spatial light modulators (SLMs) can act as gratings by displaying binary phase patterns. The grating pitch alters the diffraction angle and affects the shearing ratio when propagated a fixed distance to the image sensor. SLMs have been incorporated into phase shifting interferometry systems [23,24] but are yet to find use as diffractive shearers. The main reason is the discrete pixel pitch, which determines the change in grating

frequency and ultimately the realizable shift in shearing ratio.

The diffraction angle varies with the sine of the grating frequency as indicated by Eq. (5) in Section 3. Small shearing ratios arise from larger grating periods to reduce wavefront tilt, while greater shifts rely on smaller periods. The discrete pitch of the SLM also governs the step size between shearing ratios. A very small pitch is needed for small shearing increments, as well as to generate larger diffraction angles needed in high-shearing scenarios. A general system consisting of a 5 mm field propagating 10 mm to the sensor, calls for a $5\mu\text{m}$ SLM pitch simply to switch between ratios of 0.3 and 0.4. To achieve higher shearing ratios and increased resolution pushes the pitch closer to $1\mu\text{m}$. Additionally, the pitch of the image sensor is of concern to properly sample interferograms with increased carrier frequencies created from larger diffraction angles.

Devices with very small pitches are not currently available as commercial products. High-resolution SLMs with $8\mu\text{m}$ pixels are used in diffractive beam splitting; however, they utilize reflective, liquid-crystal-on-silicon technology [25]. Transmission-based SLMs are better suited for integrated LSI devices, but have pixels larger than $25\mu\text{m}$. Increasing the propagation distance between the diffractive element and sensor relaxes the pitch specification by decreasing the need for high diffraction angles to create large shearing ratios. This approach affects the incremental step size between shearing ratios, resulting in coarse shifts that may not yield the type of variability desired for detecting high-order aberrations.

Fabrication and packaging improvements need to be made in order to create addressable phase modulators with pitches below $5\mu\text{m}$ at high fill factors to promote diffraction efficiency. Combining such a device with a high-resolution image sensor creates an integrated wavefront sensor with the unique ability to adapt its shearing parameters based on the incoming phase. Future techniques may involve shearing within localized regions of a field to provide unprecedented levels of dynamic range. The process for identifying the optimum shearing ratio of an unknown wavefront may involve preliminary shear measurements and is currently a topic of further investigation.

7. Conclusion

We have designed and simulated an integrated, lateral shearing interferometer comprising a binary phase grating and CMOS image sensor. Tilt between overlapping diffraction orders creates a carrier fringe within the interferogram that provides gradient slope information. Fourier-based processing is used to detect and reconstruct the phase profile of the input field.

The magnitude of the lateral shear determines the points of overlap between the wavefront copies and directly affects the optical path difference within

the interferogram. Variable shearing enables the LSI technique to adjust to different types of wavefront aberration and minimizes reconstruction error. The SNR and its connection to shearing ratio has been explored with a clear relationship to the autocorrelation of the input. The optimum shear differs depending on the spatial variation of the wavefront and noise levels present during detection.

A system incorporating a SLM as a variable diffractive element can adapt the shearing ratio for maximum sensitivity and dynamic range by changing the diffraction angle. Consequently, no transmission modulator technology currently offers the $5\mu\text{m}$ resolution needed for the desired shear increment. The added flexibility would allow this LSI system to detect high-order aberrations and avoid resolution-dynamic-range trade-offs inherent to other integrated wavefront sensors.

The authors acknowledge Ronald Stack (Distant Focus Corporation) and Tessera Digital Optics Technologies for providing equipment and technical assistance. This research was supported by the Defense Advanced Research Projects Agency (DARPA) via the MONTAGE program, grant HR0011-04-I-0045.

References

1. K. Kinnstaetter, A. W. Lohmann, J. Schwider, and N. Streibl, "Accuracy of phase shifting interferometry," *Appl. Opt.* **27**, 5082–5089 (1988).
2. J. Primot, "Theoretical description of Shack–Hartmann wavefront sensor," *Opt. Commun.* **222**, 81–92 (2003).
3. P. S. Fairman, B. K. Ward, B. F. Oreb, D. I. Farrant, Y. Gilliland, C. H. Freund, A. J. Leistner, J. A. Seckold, and C. J. Walsh, "300-mm-aperture phase-shifting Fizeau interferometer," *Opt. Eng.* **38**, 1371–1380 (1999).
4. V. Ronchi, "Forty years of history of a grating interferometer," *Appl. Opt.* **3**, 437–451 (1964).
5. P. Hariharan, *Optical Interferometry*, 2nd ed. (Academic, 2003).
6. G. Paez, M. Strojnik, and G. Torales, "Vectorial shearing interferometer," *Appl. Opt.* **39**, 5172–5178 (2000).
7. J. C. Wyant, "Double frequency grating lateral shear interferometer," *Appl. Opt.* **12**, 2057–2060 (1973).
8. S. Velghe, J. Primot, N. Guérineau, M. Cohen, and B. Wattelier, "Wave-front reconstruction from multidirectional phase derivatives generated by multilateral shearing interferometers," *Opt. Lett.* **30**, 245–247 (2005).
9. M. Takeda, H. Ina, and S. Kobayashi, "Fourier-transform method of fringe-pattern analysis for computer-based topography and interferometry," *J. Opt. Soc. Am.* **72**, 156–160 (1982).
10. S. De Nicola and P. Ferraro, "Fourier transform method of fringe analysis for moiré interferometry," *J. Opt. A* **2**, 228–233 (2000).
11. D. Bone, "Fourier fringe analysis: the two-dimensional phase unwrapping problem," *Appl. Opt.* **30**, 3627–3632 (1991).
12. D. Fried, "Least-square fitting a wave-front distortion estimate to an array of phase-difference measurements," *J. Opt. Soc. Am.* **67**, 370–375 (1977).
13. R. Hudgin, "Wave-front reconstruction for compensated imaging," *J. Opt. Soc. Am.* **67**, 375–378 (1977).
14. K. Freichlad and C. Koliopoulos, "Modal estimation of a wave front from difference measurements using the discrete Fourier transform," *J. Opt. Soc. Am.* **3**, 1852–1861 (1986).
15. L. Poyneer, D. T. Gavel, and J. M. Brase, "Fast wave-front reconstruction in large adaptive optics systems with use of the Fourier transform," *J. Opt. Soc. Am. A* **19**, 2100–2111 (2002).
16. C. Elster and I. Weingartner, "Solution to the shearing problem," *Appl. Opt.* **38**, 5024–5031 (1999).
17. C. Elster and I. Weingartner, "Exact wave-front reconstruction from two lateral shearing interferograms," *J. Opt. Soc. Am. A* **16**, 2281–2285 (1999).
18. J. Goodman, *Introduction to Fourier Optics*, 3rd ed. (Roberts & Company, 2005).
19. P. Liang, J. Ding, Z. Jin, C. Guo, and H. Wang, "Two-dimensional wave-front reconstruction from lateral shearing interferograms," *Opt. Express* **14**, 625–634 (2006).
20. M. P. Rimmer and J. C. Wyant, "Evaluation of large aberrations using a lateral-shear interferometer having variable shear," *Appl. Opt.* **14**, 142–150 (1975).
21. A. Lohmann and O. Bryngdahl, "A lateral wavefront shearing interferometer with variable shear," *Appl. Opt.* **6**, 1934–1937 (1967).
22. S. Yokozeki and T. Suzuki, "Shearing interferometer using the grating as the beam splitter," *Appl. Opt.* **10**, 1575–1580 (1971).
23. Y. Bitou, "Digital phase-shifting interferometer with an electrically addressed liquid-crystal spatial light modulator," *Opt. Lett.* **28**, 1576–1578 (2003).
24. S. Zhao and P. S. Chung, "Digital speckle shearing interferometer using a liquid-crystal spatial light modulator," *Opt. Eng.* **45**, 105606 (2006).
25. A. Hermerschmidt, S. Krüger, and G. Wernicke, "Binary diffractive beam splitters with arbitrary diffraction angles," *Opt. Lett.* **32**, 448–450 (2007).

Appendix D

Multiband Solar Concentrator Using Transmissive Dichroic Beamsplitting

This appendix includes published research which was part of my advancement to candidacy. The work describes a low-concentration solar collector array which performs spectral separation using a dichroic beamsplitter. The following is a reprint which appears in:

- J. H. Karp and J. E. Ford, “Multiband solar concentrator using transmissive dichroic beamsplitting,” Proc. SPIE 7043, 70430F (2008).

The dissertation author was the primary researcher and author.

Multiband Solar Concentrator using Transmissive Dichroic Beamsplitting

Jason H. Karp and Joseph E. Ford

University of California San Diego, 9500 Gilman Dr, La Jolla, CA, USA 92093-0407

ABSTRACT

Significant efficiency increases in photovoltaic power conversion are due to improved absorption over the broad spectrum of the sun. Semiconductors have an efficiency peak at a specific wavelength associated with the material band gap. The current trend towards high-efficiency photovoltaics involves multi-junction cells where several semiconductors are grown on top of one another creating a layered device with a broad spectral response. Fabrication is a difficult and expensive process that results in small area solar cells. An alternative approach uses dielectric mirrors to optically separate the incident light by reflecting certain spectral bands while transmitting others.

Spectral splitting is simulated within a non-imaging 10x concentrator. The optical system is designed for concatenation into large arrays and incorporates two separated ray paths exiting at a common plane. Optimized photovoltaic cells can be interleaved on a single circuit board, improving packaging and thermal management compared to orthogonal arrangements. The entire concentrator can be molded from glass or acrylic and requires a dichroic coating as the only reflector. Average collection efficiencies above 84% are realized within $40^\circ \times 16^\circ$ angular acceptance.

Keywords: solar concentrator, multi-junction photovoltaics, solar beamsplitting

1. INTRODUCTION

The need for clean, renewable energy has placed enormous attention on solar power to provide the world's energy, despite currently supplying only 0.1% of generated electricity¹. Two approaches of power generation aim to utilize either the sun's thermal energy or photon energies to excite the photoelectric effect in semiconductor materials. Photovoltaics (PV) can provide point-of-use power eliminating large scale distribution problems and expenses.

Photovoltaic cells are commonly connected into large area, rigid solar panels used to cover upward-facing rooftops. These systems require large volumes of high-purity mono- or polycrystalline silicon and provide power conversion efficiencies well below 20%. The high material cost and low output levels elevate the cost per Watt to over \$5 which is currently four to five times higher than grid-based power generation¹.

Tandem and multi-junction PV cells are constructed by layering semiconductors with different absorption characteristics to convert a larger portion of the incident solar spectrum. These devices can achieve efficiencies above 40%, however are small in physical area and cost orders of magnitude more than simple silicon cells². Multi-junction solar cells hope become cost effective by using concentrating optics to capture large areas of illumination and increase the flux onto small areas.

The geometric concentration ratio is defined as the incident illumination area divided by the area of the absorber. Solar concentrators are classified into three regimes: high concentration ($>100\times$), medium concentration ($>10\times$) and low concentration ($<10\times$)³. The highest efficiency solar cells reach their peak performance under high concentration, but require strict alignment to the sun accuracy and intense cooling arrangements. Low concentration optical geometries have significant benefits since cell performance improves under increased flux⁴, less semiconductor material lowers cost and solar tracking is not necessary.

A significant portion of cost for multi-junction cells comes from the difficult fabrication involving the layered growth of several materials with different lattice constants. Strain and interface defects reduce

the yield and overall performance of the cell⁵. Solar splitting can also be achieved using dichroic mirrors which appear transparent for certain wavelengths and reflective at others. Designing dichroics into the already required concentrator incorporates various single-junction PV cells of differing materials instead of complicated, multi-junction cells. The proposed optic has the unique ability of using two dichroic reflections to provide 10x concentration onto interleaved PV cells placed on a common circuit board. The structure is cascaded into an array aiding in packaging and thermal management.

2. SPECTRAL SPLITTING

The sun is a 5760K black body radiator depositing an average of 1372 W/m² on the earth's surface⁶. The atmosphere causes specific ultraviolet and infrared spectral nulls due to absorption and scattering from water vapor, ozone, CO₂, clouds and dust. 97.5% of the resulting spectrum exists between 380nm and 2130nm⁶. The PV material should maximize its response to this very broadband illumination. Unfortunately, the photovoltaic effect requires specific photon energies above the material band gap to generate a photocurrent. Photons greater than the band gap contain too much energy and lead to excess heat from phonons while low energy photons cannot generate electron-hole pairs. This makes PV materials truly efficient at only one specific wavelength.

The solar spectrum has an irradiance peak at 885nm, corresponding to an ideal 1.4eV material band gap⁴. Silicon is the most widely-used PV material, though has a band gap of 1.12eV shifting its absorption further towards lower energy infrared photons. III-V semiconductor compounds such as gallium arsenide (GaAs) with 1.42eV band gaps are better suited for single-junction solar cells, but provide only modest efficiency gains over silicon and add significant material costs⁴.

Since the incident illumination spans 0.5-3eV, several semiconductor materials can be used in tandem to effectively convert a large portion of the incident illumination. This is the motivation for multi-junction solar cells which layer different band gap semiconductors to form a composite, high-efficiency PV cell. Double-junction, or tandem devices have demonstrated efficiencies over 35%⁷ while triple-junction cells hold the current record of 40.7%⁸. Multi-junction cells are very expensive compared to crystalline silicon due to the complicated growth necessary for lattice matching, buffer layers and terminal connection. The devices are typically small in area and are used in space applications where collection area is limited and conversion efficiency is paramount.

Spectral splitting is an alternative approach using dichroics to separate sunlight bands instead of tunneling seen in multi-junction cells. Filters formed using thin-film dielectrics can be designed to transmit a specific spectral band while reflecting another. Hot mirrors are commercial examples passing visible light while reflecting infrared. Optically splitting incident sunlight allows the use of different, single-junction devices, eliminating fabrication concerns associated with lattice matching and tunnel junctions.

The optical geometry and design of a two band, solar splitting concentrator comprises the main area of focus. Creating more than two distinct ray paths within a common optic leads to unnecessary concentrator length and complexity, requiring multiple dichroic mirrors. Optimized single-junction or multi-junction PV cells can be placed at the exit aperture of the device to maximize solar absorption.

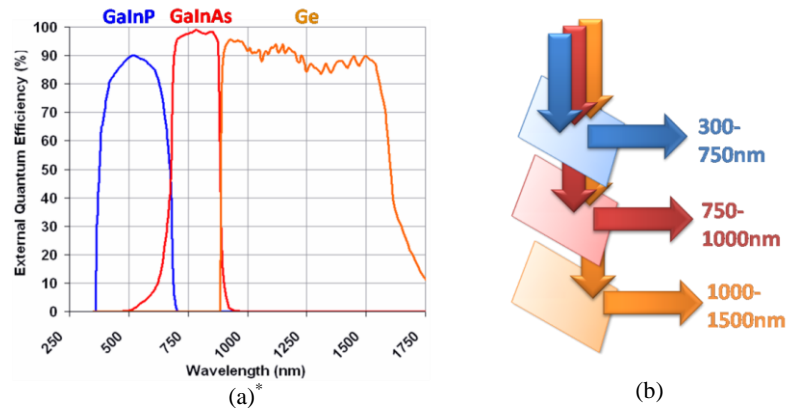


Figure 1: Multi-junction PV cells grow several different semiconductors on a common substrate material to respond to the solar spectrum (a)*. Dichroic mirrors can be used to spectrally split and direct sunlight onto monolithic PV cells (b).

*Spectrolab C1MJ_CDO-100. <http://www.spectrolab.com/prd/terres/cell-main.htm>

The simplest form of spectral splitting uses a lens to collect incoming sunlight and a dichroic beamsplitter prior to the focused spot. The dichroic divides the light into orthogonal spots, each incident on their respective PV cell⁹. Practical packaging problems exist due to the vertical orientation of the second cell. Thermal management concerns arise from the undesirable cell arrangement since concentrated photovoltaics require a heat sink to maintain efficient, long-term operation. Lastly, the overall geometry has a poor fill-factor since the orthogonal cell occupies potential upward-facing area with its positioning and heat sink.

Our proposed solution considers spectral splitting from an array of repeated lens/dichroic systems, using two mirror reflections to orient multiband light onto a single plane. Light is reflected orthogonally as with the cube beamsplitter, however the divided light is incident on a second dichroic existing within the adjacent focusing system. Upon second illumination, the light is reflected again, now propagating parallel, but laterally shifted, to the light passed by the dichroic. This enables both PV cells to be interleaved on a common circuit board, simplifying packaging and thermal management by using a single heat sink for all cells. Maximizing the area behind each lens suggests off-axis input illumination which can be accomplished by tilting the system with respect to normal illumination from the sun. Designing decentered lenses or placing a prism structure above the input can also generate an off-axis focus. These considerations will be discussed further in the following optical design section.

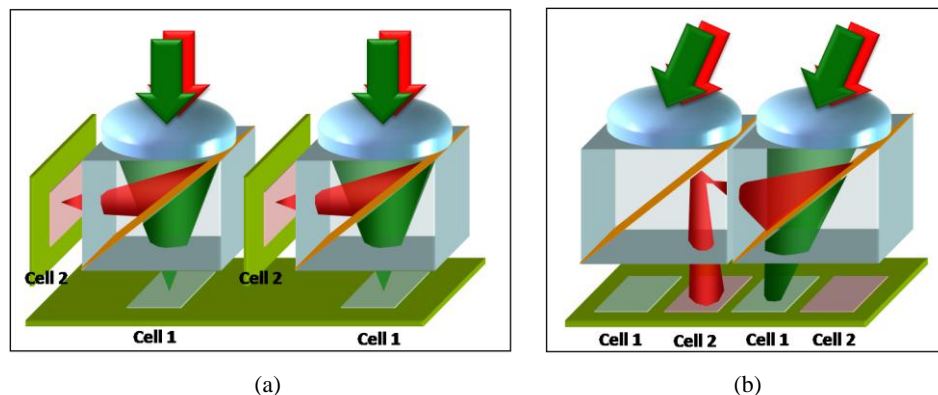


Figure 2: Single-reflection spectral splitting places the second PV cell orthogonal to the first making packaging and thermal management difficult (a). The adjacent dichroic reorients the separated band to the same plane as the transmitted band when using off-axis illumination (b).

3. OPTICAL DESIGN

The dichroic mirror is integrated into a 10x non-imaging concentrator. Our target specifications call for >80% optical efficiency from 40° acceptance East to West and 16° from North to South. The wide entrance angles allow the system to perform efficiently without active alignment during the peak hours of sunlight. The design points are well-suited to use a compound parabolic concentrator (CPC). A CPC is a modification to the cone concentrator and consists of parabolic sidewalls tilted to the extreme entrance angle, reflecting incident rays towards the exit aperture with a single bounce. The optical path length within the CPC differs based on ray positioning within the entrance pupil, leading to non-imaging concentration.

The CPC tends to be excessive in length, especially as the concentration ratio surpasses 5x. The fundamental method for overcoming physical size is to incorporate refractive elements to converge the angle of extreme rays. This involves placing a lens at the entrance as well as filling the CPC with a dielectric material. The curvature of the lens can be chosen such that the parabolic shape of the CPC regresses to a straight line creating planar sidewalls³. These improvements simplify the fabrication and allow the walls to reflect by total internal reflection (TIR).

Effective use of the area behind the lens/CPC is essential when attempting to place two PV cells next to one another. Normal illumination forms a focus directly behind the lens, leaving little continuous area for the second PV cell to reside. Off-axis illumination laterally shifts the focus creating space for both cells behind the lens. Tilting the incident sunlight is executed by tilting the entire lens system with respect to the sun or placing a prism array at the entrance pupil. Both scenarios have drawbacks of dispersion and off-axis lens aberrations. Creating decentered lens elements also causes shadowing effects as the sun arcs across the sky. Since the system is not forming an image of the sun, chromatic and off-axis aberrations have minimal impact on low concentration systems.

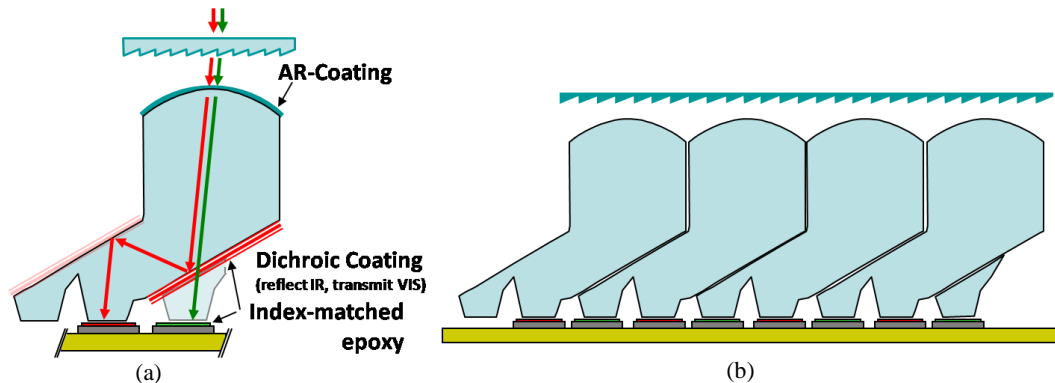


Figure 3: The double-reflection multiband concentrator exists as a single, molded optical element containing all required optical surfaces (a). Each lens/dichroic system connects with adjacent elements to form an entire array with all PV cells interleaved on a common circuit board (b).

Spectral splitting uses two dichroic reflections for one path and none for the other creating a significant difference between the optical path lengths. The refractive lens is designed to focus at a location in between these differing tracks. Transmitted rays reach the exit aperture prior to coming to a focus while the reflection path occurs just after focus. Optical power is placed on the dichroic mirror to help maintain a confined ray bundle throughout the reflection path.

The dichroic mirror is placed within the CPC to spectrally split the incident illumination. The reflector shape is formed from a set of Zernike polynomials. These circularly symmetric functions create unique curvatures allowing a single reflector design to perform well under the two illumination scenarios. Off-axis illumination places the bulk of the incoming rays on the bottom two-thirds of the reflector leaving freedom in the top portion. The specific design of the reflector is key in maintaining high optical

efficiency over large acceptance angles. The dichroic mirror is formed using a circular aperture, yet only a central region is actually used within the CPC sidewalls.

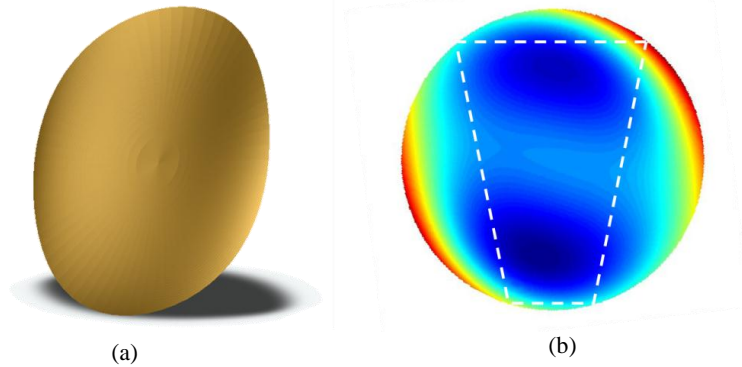


Figure 4: Circularly symmetric Zernike polynomials shape the dichroic reflector (a). Only the highlighted central region of the shape is seen by incoming rays (b).

PV cells made from semiconductor materials have refractive indexes above 3.5. The high index difference requires multi-layer antireflection coatings that only perform well over a specified angle range. Additional tapered sidewalls are designed around each exit aperture to TIR diverging rays and maintain 10x concentration. The angular extent of the exiting rays is limited to $<\pm 45^\circ$ to maximize optical coupling into the PV cell. All rays incident on the sidewalls undergo total internal reflections preventing expensive and imperfect metallic reflectors.

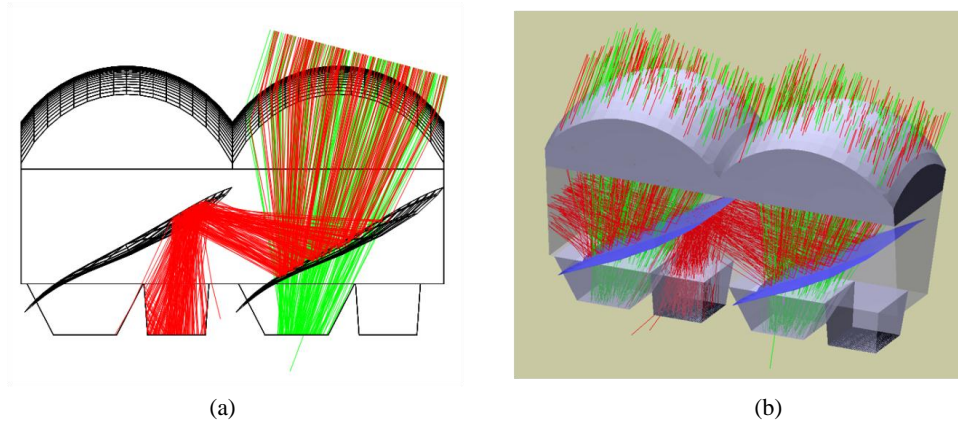


Figure 5: 2D optical ray trace (a) of the multiband dichroic concentrator (does not include all input angles). 3D optical ray trace showing placement of reflective sidewalls (b).

4. PERFORMANCE

The sun subtends a 0.5° full angle and changes its elevation in the sky throughout the year. A stationary collector must accept 71° full angle to collect direct sunlight for 7 hours per day⁶. This statistic can be misleading in that the most intense sunlight occurs from 10:00am to 2:00pm while the morning and evening sun provide less solar insolation because of increased atmospheric absorption. The multiband concentrator is designed to collect these peak sunlight hours without requiring two-axis solar tracking.

Sunlight is efficiently collected over $40^\circ \times 16^\circ$ illumination cone. The incident rays are divided into two propagation directions referred to as the transmission and reflection paths. The transmission path sees concentration from the lens and CPC sidewalls and passes through the dichroic reflector to the exit aperture. The reflection path undergoes two reflections from the primary and neighboring dichroics

with additional TIR at the tapered sidewalls around the PV cell. Optical power is placed on the reflector to constrain ray divergence within the reflection path.

The overall system was designed and simulated using Zemax Non-Sequentials. The presented results are for a 10x concentrator with a 5x5mm entrance pupil and 6.5mm physical depth; however, all dimensions can be scaled to any arbitrary size. The aspect ratio of the PV cell placed at the exit aperture of the transmission path is 1.12:1 and 1.5:1 for the reflection geometry. Incident illumination enters at 14.8° off axis. Shallower entrance angles are realized by extending the optical track; however, increased thicknesses adversely affects efficiency due to material absorption.

Collection efficiency maps for both paths are shown in Figure 6 with the on-axis origin referring to the source tilted at the designed off-axis angle. The transmission path provides 87% average collection efficiency through the $40^\circ \times 16^\circ$ angular acceptance while the reflection path yields 84% average from the same input range. The transmission path has better overall performance characteristics allowing concentration at angles beyond $44^\circ \times 24^\circ$ with $>40\%$ optical efficiency. The reflection path experiences sharper roll-offs at extended angles due to the more complicated optical track. Light which is not collected typically leaks from the sidewalls when the critical angle for TIR is not satisfied.

These results do not consider surface reflections or losses incurred from material absorption. One simulated example is constructed from UV-transparent acrylic ($n=1.491$) and yields average optical efficiencies of 82% and 76% for the transmission and reflection paths respectively over the specified acceptance angles. This includes a first-surface anti-reflection coating and material absorption characteristics for 365-1014nm wavelengths. The reflection path shows increased loss due to the absorption from the extended path length. Higher refractive index materials such as F2 glass ($n=1.62$) increase the range of TIR angles and can lead to increased angular acceptance with minor adjustments to the lens and dichroic mirror curvatures. However, high-index materials tend to have poor optical transmission at shorter wavelengths and increased cost compared to moldable acrylic.

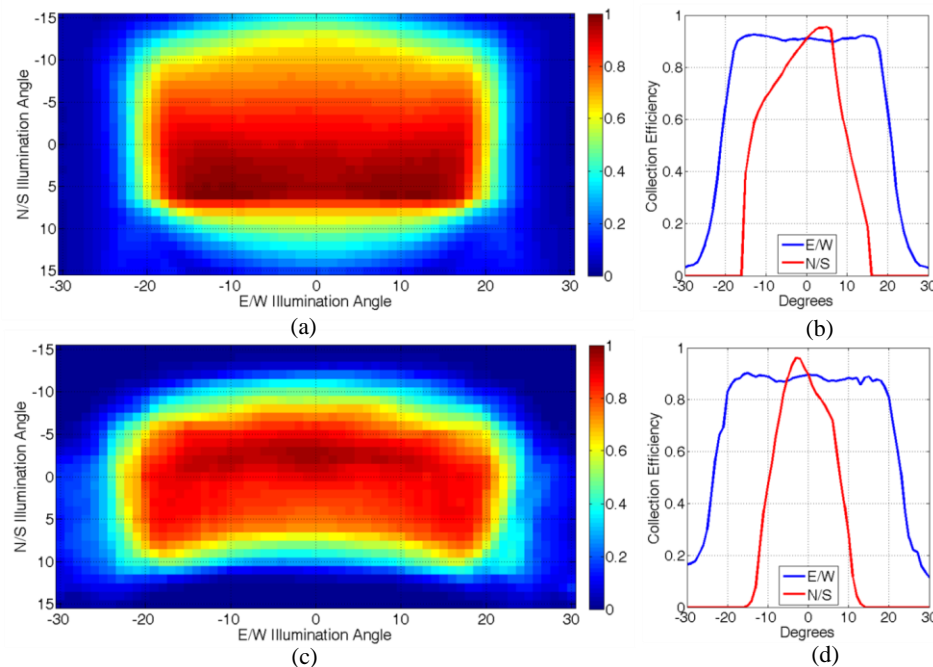


Figure 6: Collection efficiency maps for the transmission (a) and reflection paths (c). $>80\%$ collection efficiency occurs within the $40^\circ \times 16^\circ$ acceptance range. Cross sections through the origin are plotted for each path in (b) and (d).

The concentrator is oriented so the daily arc of the sun occurs orthogonal to the interleaved PV cells. The non-imaging sidewalls enable the wide-angle light to remain within the concentrator body. Seasonal elevation changes are much more difficult to collect since only the trapezoidal reflectors around the exit pupil confine the light in the North-South direction. Seasonal adjustments or single-axis tracking will help provide efficient solar collection year round.

Non-uniform illumination hinders PV cell performance and is of particular concern in concentrated photovoltaics. Localized, high-intensity hot spots can lead to cell shunting and cracking which lead to cell failure⁵. The proposed concentrator system incorporates non-imaging reflections and defocus, eliminating regions of gradient flux.

5. ASSEMBLY

The complete system is designed for concatenation into large arrays. Each subassembly may be injection molded from UV-transparent acrylic for low-cost volume manufacture. One-dimensional arrays formed in long rows are fitted together along the dichroic mirror to create a large two-dimensional concentrator. Two PV cells are interleaved on a common circuit board and attached directly to the output apertures of the concentrator array. Refractive index-matching epoxy is applied along the dichroic and exit apertures to create a single, bonded optic to the interleaved PV cells.

Two different PV cells coexist on a single output plane to collect each of the wavelength bands. Cells with an optimum band gap constructed from a single material can be placed at the exit aperture to avoid complicated and expensive fabrication associated with multi-junction solar cells. The superior performance of the transmission path should incorporate $\sim 1.6\text{eV}$ material to collect higher energy photons from visible wavelengths while using a lower band gap semiconductor at the exit of the reflection path for near infrared. The two cells alternate on a common circuit board which may contain hundreds of individual modules when large concentrator arrays are constructed. Cells of a common material may be connected in series, as in flat-plate solar modules, to increase the output voltage.

Because Zernike Polynomials are all circularly symmetric, the complicated shape of the dichroic reflector may be fabricated as a master using diamond turning. The refractive lens incorporates aspheric terms and may also be diamond machined. All other concentrator surfaces are planar and uncoated. A full manufacturing tolerance analysis is yet to be completed as this has been primarily an optical design study. Angular intersections, especially those close to the exit apertures, may need to be evaluated in order to create a moldable structure.

Multilayer dielectric thin-films are deposited on the Zernike reflector. A custom dichroic design is required to address the wavelength transition characteristics and wide-angle response. Filters containing upwards of 100 dielectric depositions can be designed to meet these specifications¹⁰, however simpler coatings may be preferable for cost considerations. The upward-facing refractive lens also requires a dielectric coating to minimize first-surface reflection and should consider acceptance angles and illumination wavelengths.

Off-axis illumination is important to enable both PV cells to reside behind a common lens. A micro-prism above the refractive lens can tilt the incoming sunlight, however requires its own anti-reflection coatings on both the entrance and exit facets. Orienting the entire concentrator at the desired angle provides the simplest solution, however the upward-facing area is reduced by the cosine of the tilt. If this approach is pursued, the tilt angle should be minimized to provide greater collection area.

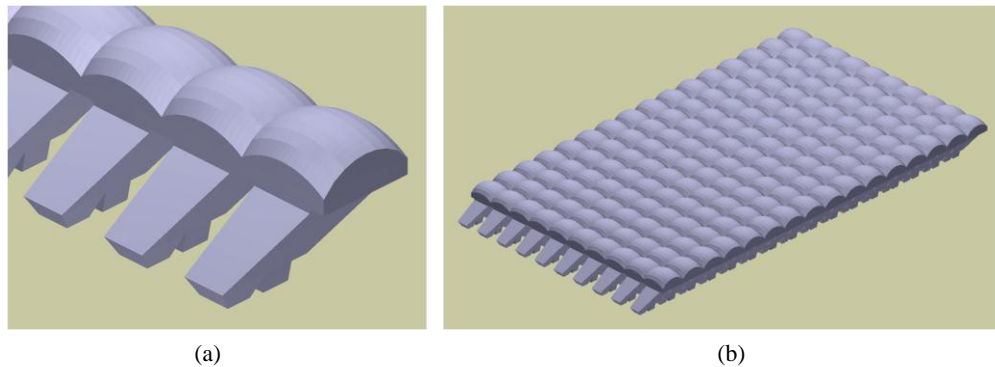


Figure 7: 3D rendering of a single multiband concentrator molded as a 1-D subassembly (a). The specific curvature of the dichroic reflector is omitted and represented as planar. The subassembly may be connected into large 2D arrays to share the adjacent dichroic (b).

6. Conclusion

Approaches to improve solar energy collection and efficiency require extended spectral absorption. Multi-junction PV cells have demonstrated high efficiencies using III-V semiconductors with different band gaps layered on top of one another. These devices are hundreds of times more expensive than crystalline silicon modules due to costly fabrication using deposition processes. Spectral splitting from thin-film dielectric mirrors offers an optical approach to multiband solar power.

The double-reflection geometry of the multiband solar concentrator improves packaging and thermal dissipation by placing both spectral bands on a common plane. Two optimized PV cells are interleaved onto the same circuit board with the concentrator bonded to the surface. The optical subassembly is designed for concatenation into a large array by sharing the neighboring dichroic mirror.

A refractive first surface is combined with non-imaging sidewalls to accept light from a $40^\circ \times 16^\circ$ illumination cone. Zernike polynomials shape the dichroic reflector to place optical power at specific locations for primary and secondary illumination. The system provides 87% and 84% average collection efficiency for the transmission and reflection paths respectively.

The dichroic concentrator can be fabricated through injection molding of inexpensive plastics or polymers. Each subassembly has a thin-film dielectric mirror and is mated to adjacent concentrators with index-matched epoxy to form the concentrator array. The optical properties of acrylic were used to optimize dimensions for the specified acceptance angles. Higher index materials provide increased design freedom regarding the illumination cone and TIR angles at the sidewall interfaces. Dichroic concentrators incorporating the double-reflection design may enable multiband solar power using monolithic PV cells instead of costly multi-junction modules.

References:

- [1] Anscombe, N., Oliver, G., "Technology Focus: Photovoltaics", *Nature Photonics*, 2, 275-292 (2008).
- [2] King, R.R. "Multijunction Cells: Record Breakers," *Nature Photonics*, 2, 284-286, (2008).
- [3] Welford, W.T. and Winston, R., [High Collection Nonimaging Optics], Academic Press, San Diego, 53-97 (1989).
- [4] Nelson, J., [The Physics of Solar Cells], Imperial College Press, London, 289-325 (2003).
- [5] Luque, A.L. and Andreev, V.M., [Concentrator Photovoltaics], Springer-Verlag, Berlin Heidelberg, 67-219 (2007).

- [6] Rabl, A., [Active Solar Collectors and Their Applications], Oxford University Press, New York, 28-80 (1985).
- [7] Fraas, L.M., Avery, J.E., Martin, J., Sundaram, V.S., Girard, G., Dinh, V.T., Davenport, T.M., Yerkes, J.W., O'Neill, M.J., "Over 35-percent Efficient GaAs/GaSb Tandem Solar Cells," IEEE Trans on Elec Dev, 37(2), 443-448 (1990).
- [8] King, R. R., Law, D.C., Edmondson, K.M., Fetzer, C.M., Kinsey, G.S., Yoon, H., Sherif, R.A., and Karam, N.H., "40% Efficient Metamorphic GaInP/GaInAs/Ge Multijunction Solar Cells," Appl Phy Let 90, 183516 (2007).
- [9] Barnett, A., Honsberg, C.B., Goossen, K., F. Kiamilev, F., Kirkpatrick, D., Kurtz, S.R., Wanlass, M.W., Emery, K., Kazmerski, L., Moore, D., Schwartz, R., Aiken, D.J. "Milestones Toward 50% Efficient Solar Cells," Paper 1AO.6.7, 22nd European Photovoltaic Solar Energy Conference, Milan, Italy, September 2007
- [10] Thelen, A., "Design of a Hot Mirror: Contest Results", Appl Opt, 35(25), 4966-4977 (1996).